10-19-2015

Electron Collisions in a Magneto-Optical Trap

Jeff Dech
University of Windsor

Electron Collisions in a Magneto-Optical Trap

By

Jeffery Michael Dech

A Thesis
Submitted to the Faculty of Graduate Studies
through the Department of Physics
in Partial Fulfillment of the Requirements for
the Degree of Master of Science
at the University of Windsor

Windsor, Ontario, Canada

2015

Declaration of Originality

I hereby certify that I am the sole author of this thesis and that no part of this thesis has been published or submitted for publication.

I certify that, to the best of my knowledge, my thesis does not infringe upon anyone's copyright nor violate any proprietary rights and that any ideas, techniques, quotations, or any other material from the work of other people included in my thesis, published or otherwise, are fully acknowledged in accordance with the standard referencing practices. Furthermore, to the extent that I have included copyrighted material that surpasses the bounds of fair dealing within the meaning of the Canada Copyright Act, I certify that I have obtained a written permission from the copyright owner(s) to include such material(s) in my thesis and have included copies of such copyright clearances to my appendix.

I declare that this is a true copy of my thesis, including any final revisions, as approved by my thesis committee and the Graduate Studies office, and that this thesis has not been submitted for a higher degree to any other University or Institution.

Abstract

Measurements of the multiple ionization cross section ratios of Cesium were performed with ion time-of-flight (TOF) spectroscopy with a magneto-optical trap (MOT) apparatus, updating the previous measurement which dates back almost a century. Results are presented for collisions at energies of 50 eV to 120 eV. With a MOT, experiments can be performed with trapped, cold atomic targets which allow for unparalleled accuracy and experiments with significant excited state target fractions above those achievable in most atomic beam experiments. A basic overview of optical cooling trapping, electron collision and atomic phenomena are presented. Experimental studies of electrons with Argon and Cesium targets were performed, measuring the multiple ionization ratios with ion TOF spectroscopy. The experimental apparatus and analysis methods are described in detail. Results are compared with previous measurements of multiple ionization ratios for both targets. Agreement within experimental error is found with the results of Tate and Smith across the energy range.

To my parents for their love,
and teaching me the value of questions

Acknowledgments

First and foremost, I wish to thank Dr. J. W. McConkey for the extraordinary privileged of his supervision during this work. His sage wisdom, patience and guidance have been incredible and words cannot describe my gratitude. I am proud to call him my mentor and my friend. I would also like to thank Dr. W. Kedzierski for his input and advice throughout this research. His ingenuity, knowledge and insight should not go unrecognized.

I also wish to thank all of the undergraduate students who have worked in the lab including Joshua Trocchi, Colin Tiessen, Justine Cunningham, Austin Lindquist and Aaron Bondy. Their help with the experimental preparation and measurements was truly appreciated and I could not have done this without them.

The technical staff of the Physics Department, Erik Clausen, Louis Beaudry and Sinisa Jezdic, must also be thanked for their contributions in the development of the experimental apparatus used in this work. The importance of their technical services to experimental research at this university cannot be overemphasized.

Finally, I would like to thank the Natural Sciences and Engineering Research Council (NSERC) and the Canadian Foundation for Innovation (CFI) for their financial support of this research.

Contents

List of Tables

List of Figures

Chapter 1

Properties and Atomic Structure of Cesium

The study of the atomic properties of Cesium (Cs) has many diverse applications. The current definition of the second is in terms of one of its optical transitions[1] and atomic clocks based on this element are used for precision chronometrology[2]. It may also be possible to construct an alkali laser from Cs[3], making understanding of its electronic properties critical. The electronic collision properties of Cs are also of considerable interest due to the fact that its nucleus is of sufficient mass that electronic scattering processes include relativistic effects which can be negligible for lighter nuclei[4]. It is also an alkali atom with a single valence electron, reducing the complexity of the atomic structure[4, 5]. These properties make it an excellent experimental benchmark[3, 6] for theoretical models of relativistic electron scattering from atoms.

Optical cooling and trapping have lead to a new era cold atom physics providing a new platform for precision measurement of samples with negligible velocities[7]. These ultracold temperatures also allow for experiments which would not be possible at room temperature due to thermal effects[8]. Laser cooling has allowed for the realization of Bose-Einstein condenstates (BECs)[7], provided a platform for investigations into quantum information and computing[9] and a host of other applications[7, 8]. Electron collisions with trapped targets have allowed for new levels precision in scattering cross section measurements in addition to the ability to perform experiments with excited state targets[10–13]. Studies of electron-atom collisions with trapped targets have been performed for Rubidium [10] and metastable Helium[11]. The Cs magneto-optical trap (MOT) used in the present study was originally constructed by John MacAskill[14]. Previously the group has measured the total scattering[12, 15] and total ionization[13] cross sections for Cs. For the first time, results were presented for excited state collisions with Cs in the $6^2P_{3/2}$ excited state[13]. This work is a continuation of that campaign measuring electron scattering cross sections with ion time-of-flight spectroscopy.

A time-of-flight (TOF) spectrometer had previously been installed by Stephen Brotton in order to measure multiple ionization cross sections of Cs. Previous measurements of the total ionization cross section used an optical technique which determined collisional trap losses from measurements of the trapped target fluorescence[12]. As this measurement determined the total losses of the trap, it was indiscriminate of ion charge and only measured total ionization losses. Ion TOF spectroscopy

on the other hand, inherently resolves differently charged ions, making it ideal for measurements of the multiple ionization cross sections. Such data is of considerable interest as the relative cross sections for multiply ionized Cs were last measured by Tate and Smith[16] in 1934.

1.1 Gas Phase Properties

The MOT is loaded by cooling Cs captured from a background vapour which fills the vacuum chamber enclosing the trap. The background vapour can be considered a thermally distributed, ideal gas where the constituents only interact[17] through elastic collisions resulting from their kinetic motion. The velocity distribution of the constituents is determined by Maxwell-Boltzmann statistics. The ideal gas model has important implications for cold atom experiments as optical cooling and trapping is a velocity dependent effect (Chapter 2). Thermal collisions can also be a source of trap losses that are dependent on thermodynamic properties of the background vapour.

1.1.1 Maxwell-Boltzmann Distribution of Speeds

In a gaseous medium, the atoms take on a distribution of speeds that describe the collective statistical behaviour of the atoms. The motion can be described by classical thermodynamics which idealizes the gas and assumes the atoms only interact through elastic collisions. The velocities of such an ensemble follow[17] the Maxwell-Boltzmann distribution

$$f(v) \; dv = \left(\frac{M}{2\pi k_B T}\right)^{3/2} 4\pi v^2 e^{-\frac{Mv^2}{2k_B T}} \; dv \tag{1.1}$$

The distribution (Figure 1.1) is in terms of Boltzmann's constant k_B, the atomic mass M and the temperature of the gas T. When integrated over all velocities, the distribution normalizes to unity with $\int dv \; f(v) = 1$. As the ideal gas particles have equal mass m, their kinetic energy $E = mv^2/2$ follows a similar distribution

$$f(E) \; dE = \sqrt{\frac{2E}{\pi (k_B T)^3}} e^{-E/k_B T} \; dE \tag{1.2}$$

which follows from the velocity distribution (1.1) transformed into the energy domain.

It is often convenient to characterize the velocity distribution by its most probable, mean, and root mean square speeds. The maximum of the velocity distribution (1.1) represents the most probable speed of any particle in the gas. The maximum occurs at $df(v)/dt = 0$ corresponding to a velocity

$$v_p = \sqrt{\frac{2k_B T}{M}} \tag{1.3}$$

The mean velocity can be found by taking the expectation value of the distribution

$$\langle v \rangle = \int_0^\infty dv \; v f(v) = \sqrt{\frac{8k_B T}{\pi M}} \equiv \frac{2}{\sqrt{\pi}} v_p \tag{1.4}$$
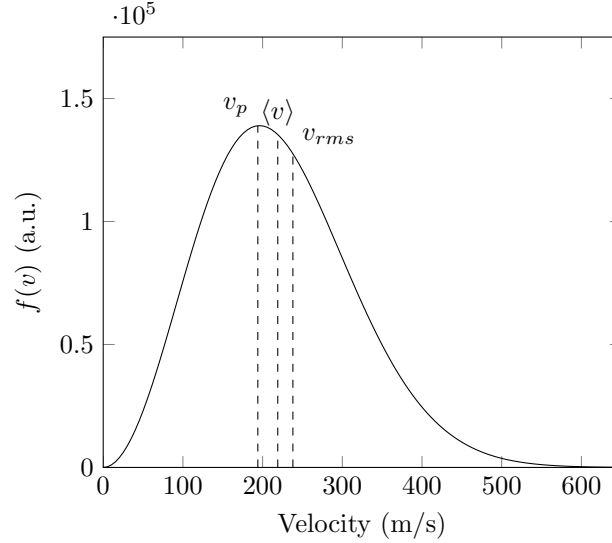
Figure 1.1: Maxwell-Boltzmann distribution of speeds for ^{133}Cs at standard temperature $T = 300\,\mathrm{K}$. Shown, left to right with dashed lines, are the most probable speed v_p, the mean speed $\langle v \rangle$ and the room mean square speed v_{rms}.

Finally, the root mean square speed is determined by

$$v_{rms} = \sqrt{\langle v^2 \rangle} = \sqrt{\int_0^\infty dv\ v^2 f(v)} = \sqrt{\frac{3k_B T}{M}} \equiv \sqrt{\frac{3}{2}} v_p \tag{1.5}$$

For atomic Cs vapour, at $T = 300\,\mathrm{K}$, these speeds have approximate values

$$v_p = 194\,\mathrm{m/s} \qquad \langle v \rangle = 219\,\mathrm{m/s} \qquad v_{rms} = 237\,\mathrm{m/s} \tag{1.6}$$

1.1.2   Thermal Gas Collisions

The collision properties of the room temperature Cs vapour in the chamber can be found from kinetic gas theory[17]. The average atomic density n is determined by the ideal gas law

$$n \equiv \frac{N}{V} = \frac{P}{k_b T} \tag{1.7}$$

which relates the number of atoms N within a volume V to the pressure P and temperature T of the sample. At ultra-high vacuum pressures of $P \approx 4 \times 10^{-8}$ torr $= 5.32 \times 10^{-6}\,\mathrm{Pa}$ and temperatures $T \approx 300\,\mathrm{K}$, the density is about $4.69 \times 10^{10}/\mathrm{m}^3$. The average distance an atom travels without colliding with another, the mean free path[17] is

$$\lambda_{mp} = \frac{1}{\sqrt{2}\pi n d^2} \tag{1.8}$$

determined by the element's effective interaction distance d and the density n. For atomic Cs in vapour[18], $d \approx 2.73\,\mathrm{nm}$ and at the UHV pressures inside the chamber, $\lambda \approx 23.5\,\mathrm{m}$. If the velocities of the particles follow a Boltzmann distribution (1.1), then the average rate of collisions between
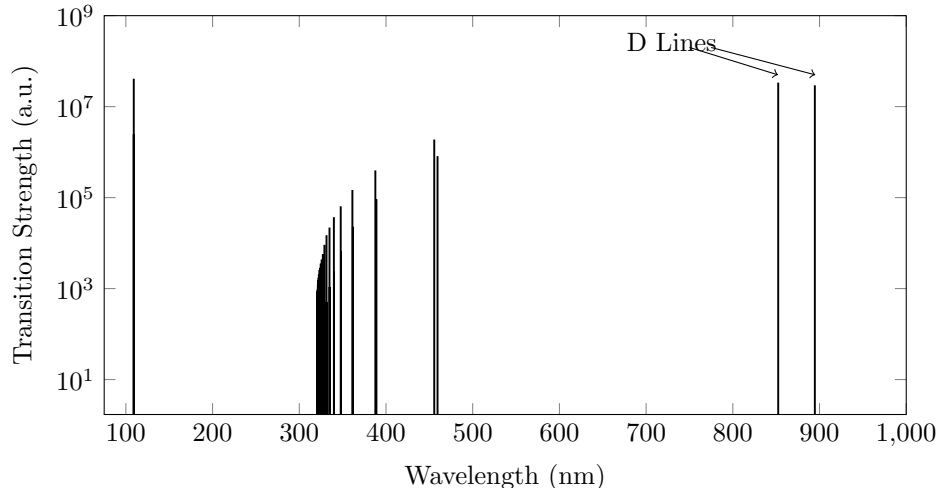
Figure 1.2: Spectral lines of ^{133}Cs. Data is taken from[19]. The D-Lines at 852 and 895 nm are shown with arrows.

particles is

$$f_c = \frac{\lambda_{mp}}{\langle v \rangle} \tag{1.9}$$

which is determined by the mean free path and the mean velocity $\langle v \rangle$ defined in (1.4) and for Cs correspond to about 9.31 Hz.

1.2 Atomic Structure

Cesium has a rich atomic structure which can be seen from its absorption and emission spectra (Figure 1.2). Its stable isotope ^{133}Cs has 55 protons and 78 neutrons. As an alkali metal, ground state Cs has a single valence electron with the remaining 54 electrons being contained within closed shell orbitals[4]. Its full configuration can be written

$$1s^2 2s^2 2p^6 3s^2 3p^6 3d^{10} 4s^2 4p^6 4d^{10} 5s^2 5p^6 6s^1 \tag{1.10}$$

or in the short hand notation $[Xe]6s^1$ based on the closed shell configuration of Xenon.

The photoabsorption spectra of neutral Cesium is shown in Figure 1.2. Two predominant features of the neutral spectrum are observed at 852 nm and 895 nm, known as the Cs D-lines[20] and correspond to the $^2S_{1/2} \rightarrow^2 P_{1/2}$ and $^2S_{1/2} \rightarrow^2 P_{3/2}$ transitions respectively. This doublet is the result of spin-orbit coupling[21] of the spin and angular momentum of the electron. Cesium can also exhibit hyperfine structure in the presence of a magnetic field. This hyperfine splitting is discussed further in Section 1.3.1 due to its importance[7] in atomic trapping. The 852 nm $^2S_{1/2} \rightarrow^2 P_{3/2}$ transition is used in atomic cooling and is the basis of the cooling scheme used in this work. The transition is in the near infrared and is accessible with inexpensive diode lasers. There are also no strong transitions nearby so narrow bandwidth lasers at this transition should not appreciably excite other atomic states.

1.3 Atomic Interactions

1.3.1 Hyperfine Structure and the Zeeman Effect

The fine-structure doublet observed in the spectral lines of Cs can be attributed to LS-coupling between the orbital angular moment and spin of the electron[21]. In the presence of a magnetic field, further hyperfine splitting can be observed due to the magnetic field interaction. A detailed review of hyperfine structure in both the non-relativistic and relativistic regimes is given by Arimondo[22]. Here, the results for non-relativistic hyperfine structure in the weak field regime are discussed.

The interaction between the atomic nucleus and the electron is given by the Hamiltonian

$$\mathcal{H}_{hfs} = \sum_k \mathbf{T}^{(k)} \cdot \mathbf{M}^{(k)} \tag{1.11}$$

which is the sum of rank k tensor operators $\mathbf{T}^{(k)}$ and $\mathbf{M}^{(k)}$ which represent the electronic and magnetic components respectively. The electric interactions are represented by the even k components while magnetic interactions correspond to odd k components.

The lowest order term $k = 0$ corresponds to the electrical interaction between the electron and the spherical component of the nuclear charge distribution. This term interacts the same with all electron states in a given configuration and so is neglected in $\mathcal{H}_{hfs}$.

The first order term $k = 1$ represents the magnetic dipole coupling of the nuclear magnetic moment with the electron's magnetic field. The nuclear magnetic moment is

$$\mathbf{M}^{(1)} \equiv \boldsymbol{\mu}_I = -g_I \mu_B \mathbf{I} \tag{1.12}$$

which is expressed in terms of the nuclear g factor and the Bohr magneton μ_B. In the non-relativistic regime, the electronic component is

$$\mathbf{T}^{(1)} = \frac{\mu_o \mu_B}{2\pi} \left\{ \frac{\mathbf{L}}{r^3} - \frac{1}{r^3} \left[\mathbf{S} - 3\frac{\mathbf{S} \cdot \mathbf{r}}{r^2} \mathbf{r} \right] + \frac{2}{3} \frac{\delta(r)}{r^2} \mathbf{S} \right\} \tag{1.13}$$

where μ_o is the vacuum permeability, $\mathbf{L}$ and $\mathbf{S}$ are the orbital angular momentum and spin operators and $\mathbf{r}$ is the electron position operator. The first term in (1.13) corresponds to the magnetic field produced at the nuclear position due to the orbital motion of the electron. The second term is related to the magnetic field created by the electron spin. The final term is the "contact interaction" which, due to the presence of the delta function $\delta(r)$, corresponds to electronic magnetization present at the nuclear position. This also implies that it can only be non-zero for s electrons.

The magnetic quadrupole term $k = 2$ has a nuclear component

$$\mathbf{M}^{(2)} = \frac{e}{2} \frac{\sqrt{6}Q}{I(2I-1)} (\mathbf{I} \cdot \mathbf{I})^{(2)} \tag{1.14}$$

where Q is the magnitude of the nuclear quadrupole moment and $(\mathbf{I} \cdot \mathbf{I})^{(2)}$ is the irreducible tensor operator created by the nuclear angular momentum. The electronic component of the interaction can be expressed as

$$\mathbf{T}^{(2)} = -\frac{e}{4\pi\epsilon_o} \frac{1}{r^3} \mathbf{C}^{(2)} \tag{1.15}$$

in terms of the auxiliary tensor operator $\mathbf{C}^{(2)}$ whose q components can be written in the spherical harmonic basis as

$$C_q^{(k)} = \sqrt{\frac{4\pi}{2k+1}} Y_q^{(k)} \tag{1.16}$$

The hyperfine structure can be considered in terms of the set of quantum numbers $\{J, I, F, m_F\}$ where J refers to the total electron momentum

$$\mathbf{J} = \mathbf{L} + \mathbf{S} \tag{1.17}$$

which varies over

$$|L - S| \leq J \leq |L + S| \tag{1.18}$$

and I is the nuclear angular momentum quantum number. The total momentum is

$$\mathbf{F} = \mathbf{J} + \mathbf{I} = \mathbf{L} + \mathbf{S} + \mathbf{I} \tag{1.19}$$

and the quantum number F is in the range

$$|I - J| \leq F \leq |I + J| \tag{1.20}$$

As nuclear transitions require very large energies, I is always a good quantum number. In the case where J is also a good quantum number, the matrix elements of $\mathcal{H}_{hfs}$ over states of different J can be neglected and the hyperfine energy is

$$E_F = \frac{1}{2} hAK + hB \frac{\frac{3}{2} K(K+1) - 2I(I+1)J(J+1)}{2I(2I-1)2J(2J-1)} \tag{1.21}$$

where $K = F(F+1) - I(I+1) - J(J+1)$.

If the atom is placed in a static magnetic field, the interaction can be described by the Hamiltonian

$$\mathcal{H}_B = -\boldsymbol{\mu}_{tot} \cdot \mathbf{B} \tag{1.22}$$

The total magnetic moment

$$\mu_{tot} = \boldsymbol{\mu}_L + \boldsymbol{\mu}_S + \boldsymbol{\mu}_I \tag{1.23}$$

is projected along the magnetic field direction. If the $\hat{\mathbf{z}}$ axis is chosen as the arbitrary field direction

$$\mathcal{H}_B = (g_L L_z + g_S S_z + g_I I_z)\mu_B B \tag{1.24}$$

where g_L, g_S and g_I are the electronic orbital, electronic spin and nuclear g factors respectively.

If the strength of the magnetic field is small relative to the fine-structure splitting, then the total electron momentum $\mathbf{J}$ is well defined. The interaction reduces to

$$\mathcal{H}_B = (g_J J_z + g_I I_z)\mu_B B \tag{1.25}$$

Here the result is expressed in terms of the Landé g-factor

$$g_J = g_L \frac{J(J+1) + L(L+1) - S(S+1)}{2J(J+1)} + g_S \frac{J(J+1) - L(L+1) + S(S+1)}{2J(J+1)} \tag{1.26}$$

If the field is sufficiently strong, it may decouple the interaction between I and J so that F is no longer a good quantum number. This is known as the *Paschen-Back* regime and the resulting hyperfine structure will not be discussed here.

If instead the field induced splitting is smaller than the hyperfine splitting, the hyperfine structure is considered in terms of the *anomalous Zeeman effect*. Here, F remains a good quantum number as the nuclear and electronic angular momenta are still coupled. The splitting is then

$$\mathcal{H}_B = g_F F_z \mu_B B \tag{1.27}$$

where the Landé g-factor g_F is

$$g_F = g_J \frac{J(J+1) - I(I+1) + F(F+1)}{2F(F+1)} + g_I \frac{J(J+1) + I(I+1) - F(F+1)}{2F(F+1)} \tag{1.28}$$

and the energy splitting between hyperfine states is equal to

$$\Delta E = g_F m_F \mu_B B \tag{1.29}$$

1.3.2 Optical Transitions and Selection Rules

Transitions between atomic states can be induced by a radiation field of an appropriate frequency ω_ℓ. At optical frequencies, the interaction can be approximated as an electric dipole transition[7]. The transition strengths are found by applying the Wigner-Eckart theorem to determine the dipole matrix elements. The accessibility of a transition can be shown to be determined by a set of selection rules which depend on the atomic structure and the polarization of the optical field, determining the optically allowed and forbidden transitions. Below, the electric dipole interaction is derived for the alkalis following the derivation of Cohen-Tannoudji[7].

If the alkali atom is approximated as a neutral, one electron atom, the physics of optical transitions between electronic states can be greatly simplified with the use of the *electric dipole approximation*. The optical field can be approximated as a traveling wave

$$\mathcal{E}(\mathbf{r}, t) = E_o \hat{\epsilon} \cos(kz - \omega_\ell t) \tag{1.30}$$

with amplitude E_o and unit polarization $\hat{\varepsilon}$. The Hamiltonian of the interaction, in terms of the field's vector potential $\mathbf{A}(\mathbf{r}, t) = c\mathcal{E}(\mathbf{r}, t)$ is

$$\mathcal{H} = -\sum_j \frac{q_j}{m_j} \mathbf{p}_j \cdot \mathbf{A}(\mathbf{r}_j, t) + \sum_j \frac{q_j^2}{2m_j} \mathbf{A}^2(\mathbf{r}_j, t) \tag{1.31}$$

where the effects on the nucleus and the electron are summed over $j = 1, 2$. In the case of single photon transitions, the quadratic term $\mathbf{A}^2$ can be neglected. Since the charges are of equal magnitude

and opposite sign, this reduces to

$$\mathcal{H} = -q \left(\frac{\mathbf{p}_1}{m_1} \cdot \mathbf{A}(\mathbf{r}_1, t) - \frac{\mathbf{p}_2}{m_2} \cdot \mathbf{A}(\mathbf{r}_2, t) \right) \tag{1.32}$$

At optical and infra-red wavelengths, the wavelength of the field λ_ℓ is orders of magnitude larger than that of atomic radius a. At long range, the variations over distance a can be neglected and the effect approximated as an electric dipole interaction. The vector potential can be evaluated at the centre of mass with position $\mathbf{r}$ and momentum $\mathbf{p}$. The Hamiltonian in then approximately

$$\mathcal{H} \approx -\frac{q}{\mu} \mathbf{A}(\mathbf{r}, t) \cdot \mathbf{p} \approx -e\mathcal{E}(\mathbf{r}, t) \cdot \mathbf{r} \tag{1.33}$$

where μ is the reduced mass

$$\mu = \frac{m_1 m_2}{m_1 + m_2} \tag{1.34}$$

Atoms can transition to or from an excited state through the absorption or emission of radiation at a specific frequency, respectively. The strength of the optical coupling can be determined in the F momentum basis (1.19) and is described by the matrix elements of

$$\langle F m_F | e\mathbf{r} | F' m_F' \rangle \tag{1.35}$$

coupling the initial state $|F m_F\rangle$ to the final state $|F' m_F'\rangle$. Applying the Wigner-Eckart theorem (Appendix B), these matrix elements can be expressed as the product of a Clebsch-Gordan coefficient and a rank-one reduced matrix element.

The matrix element can be expressed in terms of a reduced matrix element of the orbital angular momentum basis L. The following derivation is taken from Steck[20]. In a spherical basis indexed over q, the optical field can be of linear polarization with $q = 0$ or circular with $q = 1$ for right-handed and $q = -1$ for left-handed fields. The q-th spherical tensor component is then

$$\langle F \ m_F | e r_q | F' \ m_F' \rangle = \langle F \| e\mathbf{r} \| F' \rangle \langle F \ m_F | F' \ 1 \ m_F' \ q \rangle$$

$$= \langle F \| e\mathbf{r} \| F' \rangle (-1)^{F'-1+m_F} \sqrt{2F+1} \begin{pmatrix} F' & 1 & F \\ m_F' & q & -m_F \end{pmatrix} \tag{1.36}$$

Where the final line has been expressed in terms of the Wigner 3-j symbol (B.3). The reduced matrix element can be written in terms of J as

$$\langle F \| e\mathbf{r} \| F' \rangle \equiv \langle J \ I \ F \| e\mathbf{r} \| J' \ I' \ F' \rangle$$

$$= \langle J \| e\mathbf{r} \| J' \rangle (-1)^{F'+J+1+I} \sqrt{(2F'+1)(2J+1)} \begin{Bmatrix} J & J' & 1 \\ F' & F & I \end{Bmatrix} \tag{1.37}$$

written in terms of the Wigner 6-j symbol (B.5). This element can be further simplified into a reduced matrix element that depends on L yielding

$$\langle J \| e\mathbf{r} \| J' \rangle \equiv \langle L \ S \ J \| e\mathbf{r} \| L' \ S' \ J' \rangle$$

$$= \langle L \| e\mathbf{r} \| L' \rangle (-1)^{J'+L+1+S} \sqrt{(2J'+1)(2L+1)} \begin{Bmatrix} L & L' & 1 \\ J' & J & S \end{Bmatrix} \tag{1.38}$$
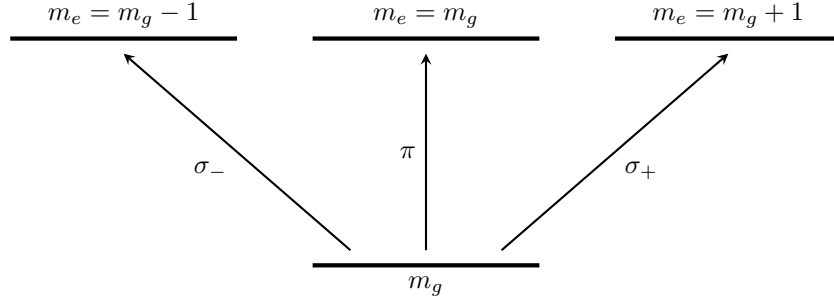
Figure 1.3: Selection rules for excitations by polarized light between ground and excited states with quantum numbers m_g and m_e respectively. The m quantum number changes by -1 for σ_- light, 0 for π light and +1 for σ_+.

The final result for the dipole matrix element can be expressed in terms of the reduced operator acting on the orbital angular momentum state and Wigner j-symbols

$$
\begin{aligned}
\mu_{FF'} = (-1)^{1+L'+S+J+J'+I-M_F'} & \langle L\|e\mathbf{r}\|L'\rangle \\
\times \sqrt{(2J+1)(2J'+1)(2F+1)(2F'+1)} & \\
\times \begin{Bmatrix} L' & J' & S \\ J & L & 1 \end{Bmatrix} \begin{Bmatrix} J' & F' & I \\ F & J & 1 \end{Bmatrix} \begin{pmatrix} F & 1 & F' \\ M_F & q & -M_F' \end{pmatrix} &
\end{aligned}
\tag{1.39}
$$

Due to the properties of the j-symbols, certain matrix elements will equal zero, corresponding to optically forbidden transitions. As all the matrix are in terms of the rank-one reduced matrix element $\langle L\|e\mathbf{r}\|L'\rangle$, only $L = L' \pm 1$ transitions are permitted. This can be seen from the Wigner $3-j$ selection rules (B.4) where $F' - 1 \leq F \leq F' + 1$ with $F' = F$ transitions being forbidden.

If the optical field is polarized, this imposes further selection rules on the transitions in addition to $L' = L \pm 1$. Three important polarization cases can be considered[7], linear (π) polarization , right handed (σ_+) and left handed (σ_-) circular polarizations. For π-polarized light, $\vec{\varepsilon}_\pi \propto \vec{\varepsilon}_z$ which acts as a rank-one tensor $T_0^{(1)}$ and only $m = m'$ transitions are allowed (Figure 1.3). In the case of σ_+, the polarization is aligned $\vec{\varepsilon}_{\sigma_+} \propto \vec{\varepsilon}_x + i\vec{\varepsilon}_y$ which acts as $T_1^{(1)}$ and $m' = m + 1$. Similarly, $\vec{\varepsilon}_{\sigma_-} \propto \vec{\varepsilon}_x - i\vec{\varepsilon}_y$ corresponds to $T_{-1}^{(1)}$ and $m' = m - 1$ transitions.

Chapter 2

Laser Cooling and Trapping

The dynamics of laser cooling are well approximated by the interaction of a two-level atom with an optical field. These dynamics evolve according to a set of coupled differential equations known as the optical Bloch equations (OBEs). The differential equations also permit a force description of the effect where the optical field can be seen to exert a radiation pressure force on the atomic system which can result in cooling. This cooling process can be described as mainly occurring through the Doppler cooling mechanism which describes the cooling in terms of the Doppler shifts of the optical field with respect to the atomic frame of reference. The temperatures associated with laser cooling processes can also be considered. The cooling of real atomic systems is discussed describing the differences between real atoms and the two-level picture. Finally, it can be shown that atoms can be both cooled and spatially confined by performing laser cooling in the presence of a magnetic field. This is the basis for the operation of a MOT. This chapter discusses some of the results which are relevant to MOTs, following the derivations of Cohen-Tannoudji[7] and Metcalf[8].

2.1 Laser Interactions with Two Level Atoms

The cooling of atoms with optical fields is typically considered in terms of a model two-level atomic system with a single ground to excited state transition at frequency ω_a. In practice, if the field is sufficiently monochromatic and near the frequency of the atomic transition ω_a, then the interaction between the ground and excited state is well approximated by a two-level description which greatly simplifies the mathematics of the problem.

Two-level cooling considers the interaction of an atom in a superposition of ground $|g\rangle$ and excited $|e\rangle$ states

$$|\psi\rangle = c_g|g\rangle + c_e|e\rangle \tag{2.1}$$

in the presence of an optical field, typically a narrow-band laser whose output is approximated as a single frequency ω_ℓ. Treating the field as a plane wave polarized along the $\hat{\varepsilon}$ direction, its electric field operator is

$$\mathcal{E}(\mathbf{r}, t) = E_o \cos(kz - \omega_\ell t)\hat{\varepsilon} \tag{2.2}$$

Provided that the laser wavelength is much larger than the atomic radius and the detuning

$$\delta = \omega_\ell - \omega_a \tag{2.3}$$

is sufficiently small, the interaction between the atom and field is represented by the Hamiltonian

$$\mathcal{H} = -e\boldsymbol{\mathcal{E}}(\mathbf{r},t) \cdot \mathbf{r} \tag{2.4}$$

The form of the interaction is that of an electric dipole aligned along the polarization axis.

If the laser frequency ω_ℓ is tuned close to the atomic transition ω_a, the optical field can drive the atom between the ground and excited state through cycles of absorption and spontaneous emission known as Rabi oscillations. The oscillations are characterized by the detuning δ from resonance and the Rabi frequency

$$\Omega = -\frac{eE_o}{\hbar}\langle e|\mathbf{r}|g\rangle \tag{2.5}$$

which is determined by the strength of the electric field of the laser E_o and the dipole matrix element $\langle e|\mathbf{r}|g\rangle$ of the position operator. The system evolves according to a set of second-order differential equations

$$\frac{d^2 c_g}{dt^2} - i\delta\frac{dc_g}{dt} + \frac{\Omega^2}{4}c_g = 0 \tag{2.6a}$$

$$\frac{d^2 c_e}{dt^2} + i\delta\frac{dc_e}{dt} + \frac{\Omega^2}{4}c_e = 0 \tag{2.6b}$$

The ground and excited state probabilities $|c_{g,e}|^2 = c_{g,e}^* c_{g,e}$ oscillate in time (Figure 2.1) with frequencies and amplitudes determined by the field detuning δ. Physically, this corresponds to an oscillating cycle of absorption and stimulated emission by the atom. The atom absorbs a photon from the optical field, transitioning to the excited state. The atom is then stimulated by the field to emit a photon with the same polarization as field, transitioning back to the ground state. The interaction also results in *light shifts* to the ground and excited state energies

$$\Delta E_{e,g} = \frac{\hbar}{2}(-\delta \pm \Omega) \tag{2.7}$$

An atom in the excited state can also randomly decay through *spontaneous emission* to the ground state emitting a photon with a random direction and polarization. Decay by spontaneous emission is described by the exponential relationship

$$\frac{dc_{e0}}{dt} = -\frac{\gamma}{2}c_{e0}(t) \tag{2.8}$$

in terms of the natural line width

$$\gamma = \frac{\omega_a^3 \mu^2}{3\pi\epsilon_0 \hbar c^3} \tag{2.9}$$

which is proportional to μ the dipole matrix element of the transition and ω_a the frequency of the atomic transition. It is important to note that the spontaneous decay process can occur irrespective of any possible Rabi oscillations. Therefore, in the presence of the optical field, an atom in the excited state can transition to the ground state in one of two ways. It can either complete the Rabi cycle and emit a photon through stimulated emission or it can decay randomly through spontaneous
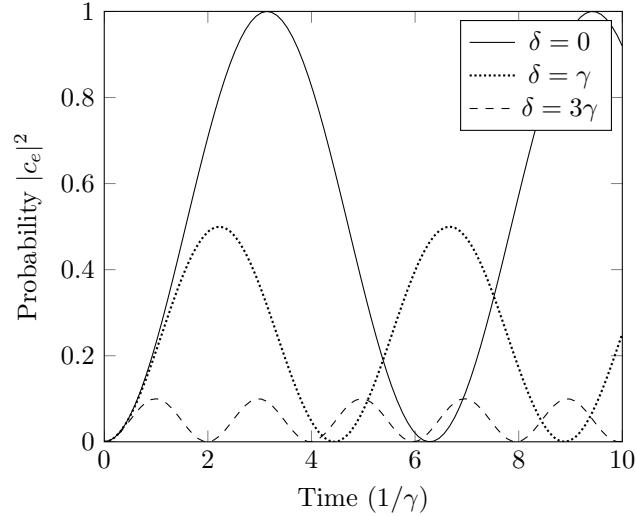
Figure 2.1: Time evolution of the excited state probability $|c_e|^2$. The excited state probability is proportional to the detuning and Rabi frequency both in amplitude and oscillation frequency. In all cases $\Omega = \gamma$. The solid curve represents the on resonance behaviour with $\delta = 0$. The dotted curve corresponds to $\delta = \gamma$ and the dashed curve $\delta = 3\gamma$.

emission. This breaks the original symmetry of the Rabi problem and a different mathematical treatment is needed to consider the dynamics of the two processes simultaneously.

When considering both processes, the state of a single atom contains insufficient information to determine the evolution of the system given that it can interact through two independent processes. Using the density matrix formalism, one can linearly add the effects of Rabi oscillations and spontaneous emission to arrive at the time evolution of the system. An ensemble of two-level atoms has a density matrix representation

$$\rho = \begin{pmatrix} \rho_{ee} & \rho_{eg} \\ \rho_{ge} & \rho_{gg} \end{pmatrix} = \begin{pmatrix} c_e c_e^* & c_e c_g^* \\ c_g c_e^* & c_g c_g^* \end{pmatrix} \tag{2.10}$$

and the dynamics are described by the sum of the interactions (2.6) and (2.8). The resulting set of coupled first-order differential equations

$$\frac{d\rho_{ee}}{dt} = -\gamma \rho_{ee} + \frac{i}{2}(\Omega \tilde{\rho}_{ge} - \Omega^* \tilde{\rho}_{eg}) \tag{2.11a}$$

$$\frac{d\rho_{gg}}{dt} = +\gamma \rho_{ee} + \frac{i}{2}(\Omega^* \tilde{\rho}_{eg} - \Omega \tilde{\rho}_{ge}) \tag{2.11b}$$

$$\frac{d\tilde{\rho}_{eg}}{dt} = -\left(\frac{\gamma}{2} - i\delta\right)\tilde{\rho}_{eg} + \frac{i}{2}\Omega(\rho_{gg} - \rho_{ee}) \tag{2.11c}$$

$$\frac{d\tilde{\rho}_{ge}}{dt} = -\left(\frac{\gamma}{2} + i\delta\right)\tilde{\rho}_{ge} + \frac{i}{2}\Omega^*(\rho_{ee} - \rho_{gg}) \tag{2.11d}$$

are known as the optical Bloch equations (OBE). The system can be described in terms of the population difference $w = \rho_{gg} - \rho_{ee}$ and the optical coherence ρ_{eg}. At steady state $dw/dt =$

$d\rho_{eg}/dt = 0$ and the OBEs (2.11) have solutions

$$w = \frac{1}{1+s} \tag{2.12a}$$

$$\rho_{eg} = \frac{i\Omega}{2(\gamma/2 - i\delta)(1+s)} \tag{2.12b}$$

where the saturation

$$s \equiv \frac{I/I_s}{1 + (2\delta/\gamma)^2} \tag{2.13}$$

can be written in terms of the laser saturation intensity

$$I_s \equiv \frac{\pi hc}{3\lambda^3\tau} \tag{2.14}$$

The steady state solution has an important implication in the context of laser cooling. The population difference w and therefore the excited state population

$$\rho_{ee} = \frac{1-w}{2} = \frac{s}{2(1+s)} = \frac{I/I_s}{1 + I/I_s + (2\delta/\gamma)} \tag{2.15}$$

for a given atomic species is determined by the intensity and frequency detuning of the optical field. At low intensities $s \ll 1$, the solution (2.12) has $w \approx 1$ and the atoms are mostly in the ground state. At large saturation values $s \gg 1$, the population difference becomes negligible and $\rho_{ee} \approx 1/2$.

It is also possible to describe the interaction in terms of the force applied to the atoms by the optical field. The force in one dimension can be found from Ehrenfest's Theorem

$$F = -\left\langle \frac{\partial \mathcal{H}}{\partial z} \right\rangle \tag{2.16}$$

In an optical field with small detuning δ, the force has the form

$$F = \hbar q_r (\Omega \rho_{eg}^* + \Omega^* \rho_{eg}) + i\hbar q_i (\Omega \rho_{eg}^* - \Omega^* \rho_{eg}) \tag{2.17}$$

where q_r and q_i are the real and imaginary components of the logarithmic derivative $\partial_z\Omega/\Omega$. The first term in (2.17) corresponds to a dipole force which is proportional to the energy of light shift (2.7) and scales with the intensity. The second term derives from the process of spontaneous emission and is termed the *radiation pressure force*. This viscous forces slows and cools the atoms but it saturates at large intensities so cannot be increased without limit. This second force is of particular interest for a MOT where low intensity fields are used with negligible dipole forces and the radiation pressure term of (2.17) dominates.

An important case of this pressure force is for an atom moving in a standing wave pattern with electric field

$$E(z) = E_o \cos(kz)\left(e^{i\omega t} + e^{-i\omega t}\right) = 2E_o \cos(kz)\cos(\omega t) \tag{2.18}$$

At low intensities, the spatially averaged force of the field is

$$F_{av} = -\hbar k^2 v \frac{8(I/I_s)(\delta/\gamma)}{(1 + (2\delta/\gamma)^2)^2} \equiv -\beta v \tag{2.19}$$

The optical field exerts a damping force on the atom slowing its atomic motion. Classically, one would expect that the force would bring the atom to rest with $v = 0$ but this is not the case. In Section 2.3 the temperature limits of laser cooling are discussed in more detail.

2.2 Doppler Cooling

The Doppler cooling mechanism provides an appealing description of the mechanics of the damping force (2.19). Consider an atom moving in one dimension in the standing wave pattern created by two counter-propagating beams. In the reference frame of the moving atom, both beams will be Doppler shifted by a frequency

$$\omega_D = -\mathbf{k} \cdot \mathbf{v} \tag{2.20}$$

The co-propagating beam ($\mathbf{k}$) will be red shifted farther from resonance while the counter-propagating beam ($-\mathbf{k}$) will be blue shifted closer to resonance. The force exerted on the atom increases as the frequency approaches ω_a and so the blue shifted counter-propagating beam exerts a stronger force than the red shifted co-propagating beam. The net result is a force that, due to symmetry, always opposes the motion of the atom. If the atom is stationary, there will be no Doppler shift and the forces of the two beams are equal and opposite. As a result the resting atom experiences no net force.

If the field is of sufficiently low intensity that the effects of spontaneous emission can be ignored, then we do not need to consider the case of excitation from one laser and stimulated emission from the second. This eliminates the consideration of the arising velocity dependent forces. In this low intensity limit, the force from each beam is

$$\mathbf{F}_\pm = \pm \frac{\hbar k \gamma}{2} \frac{s_o}{1 + s_o + [2(\delta \mp |\omega_D|)/\gamma]^2} \tag{2.21}$$

Summing these two forces together, the resultant force is approximately

$$F \approx \frac{8\hbar^2 k^2 \ (I/I_s) \ \delta \ v}{\gamma \ (1 + s_o + (2\delta/\gamma)^2)^2} \approx -\beta v \tag{2.22}$$

where terms of $\mathcal{O}(kv/\gamma)^4$ and greater have been neglected. In the two level model, maximum damping occurs for $2\delta/\gamma = -1$ when the field is red detuned by half the natural linewidth of the transition

$$\delta = -\frac{\gamma}{2} \tag{2.23}$$

As can be seen in Figure 2.2, for sufficiently small velocities the net force is proportional to v and acts as a frictional force against the atomic motion. At larger velocities however, the force can be seen to decrease implying that atoms traveling above some velocity limit will not be captured and cooled. The cooling force (2.22) has maxima near $v = \pm\delta/k$ which defined the *capture velocity*

$$v_{capt} \approx \frac{\gamma}{k} \tag{2.24}$$

an upper limit on the speed at which atoms can be moving and still cooled to near zero velocity. The dependence on the decay parameter γ implies that v_{capt} is dependent on which atomic species
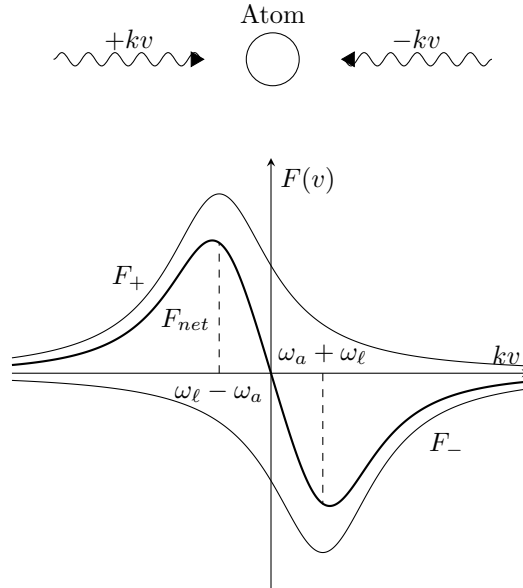
Figure 2.2: The radiation pressure force produced in one dimensional standing wave for a moving atom. The dashed curves represent the individual forces for the right moving (top) and left moving (bottom) beams. The solid curve represents the net force. For small velocities the force is approximately linear. In this region, the net force acts to dampen the atomic motion, cooling the atom.

is being cooled. In the case of Cesium, the capture velocity is $4.42 \, \mathrm{m/s}$.

Cooling in one dimension can easily be extended to three dimensions with the use of six beams rather than two. Three mutually orthogonal sets of counter-propagating lasers with equal frequency are arranged to intersect at a point. At this intersection, an atomic sample can be cooled forming an *optical molasses*. As noted earlier, the Doppler force (2.22) is a purely velocity dependent force and does not act on atoms at rest. The atoms may be cooled but there is no force spatially confining them to the cooling region. Atoms could drift or be kicked out of the optical field, escaping into the background. In Section 2.5, it will be shown how magnetic forces can be combined with the Doppler cooling mechanism in a *magneto-optical trap* (MOT) which is capable of both cooling an atomic sample and confining it within a certain spatial region.

2.3   Temperatures Associated with Laser Cooling

In classical thermodynamics, temperature is defined for a closed system in thermal contact with its surroundings which has reached a equilibrium through heat exchange. In laser cooling, the classical ideas of thermal contact and heat exchange are not easily transfered to the quantum description of the cooling process. Furthermore, the system is classified by large fluctuations in the state of the system as a result of the interactions so there is not even an appropriate equilibrium point to consider the temperature of. It is still possible however to define a quantity deemed the temperature from the average kinetic energy of the sample, a quantity which is much better defined in optical cooling.

If the atomic sample has a well defined velocity distribution with average kinetic energy $\langle E_k \rangle$

then it is convenient to define the temperature of the sample as

$$k_B T = 2\langle E_k \rangle$$

where k_B is Boltzmann's constant. The requirement of well defined velocity is necessary to apply this definition. If it were not required, then there could be infinitely many distributions with equal kinetic energy and this expression becomes ill-defined. As laser cooled samples have well defined velocity distributions, this relationship is valid in the present context.

Consider the temperature of atoms traveling at the capture velocity $v_{capt} = \gamma/k$ with average kinetic energy $\langle E_k \rangle = M v_c^2/2$. The corresponding temperature to this energy is

$$k_B T_c = \frac{M\gamma^2}{k^2} \tag{2.25}$$

and represents the warmest temperature from which a sample can be cooled. The temperature is typically on the order of mK and in the case of Cesium, $T_c = 312.14 \, \text{mK}$.

It is also possible to consider the low temperature limits of Doppler cooling. The form of the cooling force (2.22) is a pure damping force and classically the atoms could be expected to achieve a zero velocity. In reality however, at low temperatures the Doppler cooling process results in a competition between the fluctuations of photons absorbed from the field and fluctuations of emitted photons carrying momentum away. The point at which these two processes reach an equilibrium is determined by the natural width of the atomic transition used for cooling. This equilibrium point is known as the Doppler temperature

$$k_B T_D = \frac{\hbar\gamma}{2} \tag{2.26}$$

and is often on the order of hundreds of μK. Relating this to the average kinetic energy, atoms at the Doppler temperature moving in one-dimension have a velocity

$$v_D = \sqrt{\frac{k_B T_D}{M}} \tag{2.27}$$

Cesium can be Doppler cooled to $T_D = 124.39 \, \text{μK}$ and a corresponding speed $v_D = 8.82 \, \text{cm/s}$.

While sub-Doppler cooling methods can reach temperatures below the Doppler limit, there is still a fundamental limit to the temperatures achievable with optical cooling processes. As the interactions rely on the absorption or emission of a photon, which has an associated momentum $\hbar k$, the atom must recoil after the interaction with a velocity $v_r = \hbar k/M$. This recoil limit corresponds to a temperature

$$k_B T_r = \frac{\hbar^2 k^2}{M} \tag{2.28}$$

The recoil limit is on the order of hundreds of nK to a few μK and is considered the lower limit for optical cooling. The recoil limit for Cesium is $T_r = 198 \, \text{nK}$ with $v_r = 0.352 \, \text{cm/s}$.

2.4   Cooling Mutli-level Atoms

Up to this point, optical forces have been considered for an ensemble of ideal, two-level atoms. In practice real atoms have multiple fine and hyperfine levels and it is possible for atoms to transition
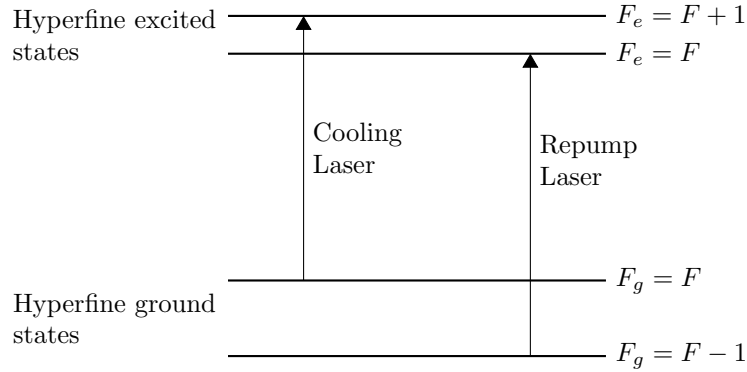
Figure 2.3: Typical cooling experiments pump the $F_g = F \rightarrow F_e = F + 1$ transition. Atoms which decay to the $F_g = F - 1$ ground state escape the optical loop. A repumping laser at the $F_g = F - 1 \rightarrow F_e = F$ transition frequency can be introduced to re-introduce the atoms into the excite state manifold.

between multiple states. In the absence of any interactions, the hyperfine states are nearly degenerate but this degeneracy can be lifted with the application of a magnetic field (Section 1.3.1). Cooling under such conditions is the basis for the operation of a MOT (Section 2.5). The process of cooling alkali samples is well described by the two-level system approach and the strength of the interaction is proportional to the dipole strength of the cooling transition. In practice, transitions can exist that can take the atom out of the two state optical loop and so effective cooling often requires additional measures to ensure these atoms are brought back into the cooling cycle.

Cooling can be performed on a $F_g = F \rightarrow F_e = F + 1$ transition provided that there is sufficient optical coupling between the two states (Section 1.3.2). However, in practice the line-width of the laser is often wide enough to also excite nearby states. If these states decay to the $F_g = F - 1$ hyperfine state, the atom will be inaccessible to the laser and leave the cooling cycle. In order to counteract decays into this dark ground state, an additional repumping laser can be introduced at the $F_g = F - 1 \rightarrow F_e = F$ transition frequency (Figure 2.3) to return the atoms to the excited state manifold.

2.5   Magneto-Optical Traps

A magneto-optical trap (MOT) applies laser cooling mechanisms in the presence of a magnetic field to permit spatial confinement of the cooled sample through a magneto-optic interaction based on the Zeeman splitting resulting from the electron spin interaction with the magnetic field. We first consider the situation of a two level atom with a $F_g = F \rightarrow F_e = F + 1$ transition moving in one dimension. The magnetic field is chosen with a linear field gradient

$$B(z) = Az \tag{2.29}$$

and two counter-propagating laser beams are placed along the axis of motion, red detuned from the atomic resonance ω_a by a frequency $\delta < 0$. The two beams are circularly polarized $\sigma_\pm$ and of opposite handedness. The polarization is chosen so that the right handed σ_+ beam is moving in the
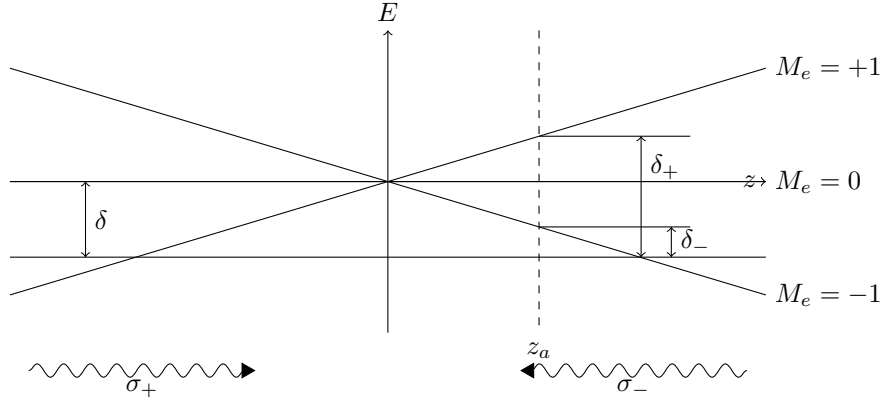
Figure 2.4: A one dimensional MOT configuration. Two counter-propagating red-detuned lasers with equal frequency and intensity are polarized such that the right handed σ_+ is moving to the right and the left handed σ_- to the left. The atoms move in a magnetic field $\mathbf{B} = A\mathbf{z}$. For atoms on the right, the $M_e = -1$ state is closer to resonance and more light is scattered from the σ_- beam driving the atoms to the center. On the left side, the $M_e = +1$ state is closer to resonance and scatters more light from the σ_+ beam. The symmetry of interaction traps the atoms at the center of the magnetic field.

positive z direction and the left handed σ_- beam travels in the *negative* z direction (Figure 2.4).

This configuration leads to a position dependent force which confines the sample. If the atom is at some position $z_a > 0$, the Zeeman splitting (1.21) increases the energy of the $M_e = +1$ state while decreasing the energy of the $M_e = -1$ state by an equal amount. This energy shift drives the $M_e = -1$ state closer to resonance with the lasers while also driving $M_e = +1$ farther away. As the σ_- beam drives the $g \to e$, $\Delta m = -1$ transition, the force of the beam is increased and the atom is driven towards $z = 0$, the center of the trap. On the other side where $z_a < 0$, the $M_e = +1$ state is now driven to closer to resonance, increasing the interaction with the σ_+ beam and again the atom is driven towards the center of the trap. Atoms are now both cooled and trapped by the addition of this position dependent effect to previously discussed cooling mechanisms.

In the presence of the magnetic field, the Doppler force (2.22) of the two beams is modified to

$$F_\pm = \frac{\hbar\gamma\mathbf{k}}{2}\frac{I/I_s}{1 + (I/I_s)(2\delta_\pm/\gamma)^2} \tag{2.30}$$

where the modified detuning

$$\delta_\pm = \delta \mp \mathbf{k} \cdot \mathbf{v} \pm \frac{\mu' B}{\hbar} \tag{2.31}$$

is determined by the relative magnetic dipole moment between the ground and excited states $\mu' = \mu_B(g_e\mu_e - g_g\mu_g)$. The net force of the two beams can be written as the sum of two terms

$$F \equiv -\beta\mathbf{v} - \kappa\mathbf{r} \tag{2.32}$$

This magneto-optical force has the form of damped harmonic motion. It contains the velocity

dependent Doppler term (2.22) $\beta\mathbf{v}$ and a restoring force $\kappa\mathbf{r}$ with spring constant

$$\kappa = \frac{\mu' A}{\hbar k}\beta \tag{2.33}$$

Considering the system as a damped oscillator, the oscillations can be characterized by damping and oscillation frequencies of

$$\Gamma_{MOT} = \frac{\beta}{M} \qquad \omega_{MOT} = \sqrt{\frac{\kappa}{M}} \tag{2.34}$$

This idea can easily be extended to three dimensions with the use of three sets of orthogonal beams intersecting at the center of a magnetic field with a linear gradient in all three directions. An atomic cloud of cold atoms can be trapped at the center where the position-dependent force is zero. The size of this cloud can be estimated from the temperature of the sample as

$$k_B T = m v_{rms}^2 = \kappa z_{rms}^2 \tag{2.35}$$

For temperatures around the Doppler cooling limit, the atomic cloud is typically on the order of tens of µm to a few mm.

Chapter 3

Electron-Atom Collisions

The study of electron-atom collisions is important in a number of applications. The development and testing of collision theories is important for understanding and modeling atomic systems[5, 23]. These types of collisions are also important in the understanding of plasma phenomena[24] and astrophysical processes[23]. They can also be relevant in seemingly unrelated fields such as biophysics[25] and the production of integrated circuits[24].

One important factor in electron collisions is that the projectile's mass is orders of magnitude less than that of the atomic target, $m_e \ll M$, and the transfer of kinetic energy to the atom during scattering can be considered negligible[17]. The electron may still transfer energy to the atom which can result in changes to the atomic configuration. If no energy is transfered, the collision is considered *elastic* and the electron scatters from the target by some angle, exiting with no change in speed. An *inelastic* collision transfers energy to the atom, resulting in a change of atomic state. *Superelastic* collisions may also occur with energetic targets[26] where energy is transfered to the electron, increasing its final kinetic energy.

There are certain energy regimes associated with electron collisions. At *low* energies, the collisions are mostly elastic with some resulting in transitions to energetic bound states in the target. The region around the atomic ionization potential are considered *intermediate* energies where inelastic scattering result in bound and ionization excitations. In this regime only a few collision channels are open as the impact energy is close to the binding energy of atomic electron. As such, in ionization collisions, previously bound electrons exit with little kinetic energy. At *high* energies many channels are open, ionized electrons can have considerable kinetic energy gains, and more complex dynamics such as multiple ionization can occur.

3.1 Quantifying Collision Processes

Scattering in collisions is often quantified and reported as a cross section value. In classical scattering between two hard spheres[26], the cross section corresponds to the geometric area that the target presents to the incoming projectile. In a quantum mechanical picture, the cross section can be interpreted as the probability that a certain collision event will occur under a given set of conditions[17]. Generally, the cross section value is dependent on the particles involved, the particular collision process, the velocities of the particles and their separation distance.

Often, the cross section for some process i is denoted by the symbol σ_i. Scattering in a given direction through the solid angle $d\Omega(\theta, \phi)$ is given by the *differential cross section* $d\sigma_i/d\Omega$. Integrating over all solid angles gives the total cross section for the process

$$\sigma_i = \int d\Omega \, \frac{d\sigma_i}{d\Omega}(\theta, \phi) \tag{3.1}$$

The *total scattering cross section* represents the scattering from all channels

$$\sigma_{tot} = \sum_{i \in S} \sigma_i \tag{3.2}$$

in the set S which can occur in a particular system. A "total" cross section value may also be associated with a specific set of processes. For example, the total elastic and total ionization cross sections correspond to the total probabilities of elastic scattering and atomic ionization respectively.

Reported cross sections may also differ in how they are normalized[17]. An *absolute* cross section is normalized to the densities and profiles of the electron and target beams and provides a measure of the scattering from a single collision. These values are often reported in units of cm^2 or in terms of the Bohr radius with units of πa_o^2. *Relative* cross sections are not fully normalized and remain dependent on certain parameters of the experiment in which they were measured, such as the collision geometry. In some cases it is possible to determine the absolute cross section from a relative measurement by normalizing to related intermediate cross section values.

3.2 Electron Ionization Collisions

During an inelastic collision, if the projectile transfers energy to an atomic electron in excess of its binding energy, ionization of the atom can occur[26]. Below this threshold, there is only sufficient energy to transfer the electron to a bound excited state of the atom which may later decay optically or it may be metastable[23]. Above the ionization potential however, the bound electron can transition to a free-electron continuum state, exiting the collision region and leaving an atomic ion. Ionization may occur through one of a number of reaction channels depending on the impact energy[17]. While electron ionization of lighter atoms is considered fully understood[5], more work remains to fully understand[3, 4, 23] collisions with larger, heavier atoms exhibiting more complex scattering dynamics.

The majority of ionization collision with an atom A occur[26] through direct channels

$$e^- + A \rightarrow 2e^- + A^+ \tag{3.3}$$

where the energy transfer from the projectile results in an atomic electron transitioning from a bound to free electron state. Multiple ionization may also occur through direct processes

$$e^- + A \rightarrow (n+1)e^- + A^{n+} \tag{3.4}$$

but usually only occur appreciably in collisions with heavier atoms and at higher energies[17]. It is also possible for collisions to leave the target in an excited state A^* which later transitions to an

ionization state

$$e^- + A \rightarrow e^- + A^* \rightarrow 2e^- + A^+ \tag{3.5}$$
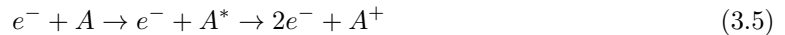
through an *autoionization* collision (also known as the *Auger effect*).

The study of atomic ionization collisions is important in understanding the quantum three-body problem[5, 17]. In these collisions the transition to the final state results in three particles, two electrons and an atomic ion. While elastic scattering is considered a well described process[17], only recently has the problem of electron impact ionization been fully solved for the H and He atoms[5] analytically. Several theoretical approaches have been proposed to solve the problem both analytically and with numerical approximations. Analytic models can be applied to few electron systems but as the number of particles involved in the calculation increases, the complexities of many-body systems make these methods difficult and numerical computations are preferred in these situations.

Several numerical methods have been proposed to accurately model electron collisions, two of the most successful being the atomic R-matrix with pseudostates (RMPS)[23] and convergent close coupling (CCC)[5]. The RMPS method has been shown to produce accurate cross section values for low and intermediate energies[23], demonstrating excellent agreement with experiment, especially for lighter atoms[27]. In this method, the collision space is divided into internal, external and asymptotic regions which are solved independently, matching the solutions at the region boundaries. In the CCC approach, target eigenstates and square integrable pseudostates are expanded in a complete basis and the scattering amplitudes are determined by solving a set of coupled integrodifferential equations in momentum space. Good agreement with experimental benchmarks has been found with this method[5].

3.3 Measurement of Electron Collision Cross Sections

While experiments studying electron-atom collisions date back to turn of the 20th century[26], quantitative measurements of scattering cross sections were first reported by Ramsauer in 1921[17]. The experiments involved the measurement of the transmission losses of an electron beam passing through a gas sample and measured the total collision cross section, determined by the beam attenuation of the target. Since then, advances in technology have made possible new techniques, such as crossed beam[17, 26] and trapped target[10] studies, which permit high resolution cross section measurements and new levels of precision which have become critical for benchmarking of today's very accurate theoretical models and for proper understanding of complex atomic and molecular targets.

Crossed beam methods have been in use since the 1950s[26] and these studies are responsible for much of the current cross section data for atomic and molecular targets[19]. In these experiments, a thermal velocity target beam is crossed with an electron beam to form the collision region. Products formed in the reaction volume at the intersection are then detected either in, or perpendicular to the plane formed by the two beams. The measured cross section is relative[17] and must be normalized to the electron and target densities relative to the geometry of the interaction volume to obtain absolute cross section data. Great care must be taken when determining these absolute values to ensure that the beam densities and geometries are well known which can often require considerable effort to realize experimentally.

Detection methods have also significantly improved since early transmission loss measurements and scattering products can now be measured directly with single charged particle detectors[17]. Scattered electrons can be measured with high resolution spectroscopy methods to determine energy loss spectra of the projectiles[26]. In this work, the scattered ion products are instead resolved with ion TOF spectroscopy to determine the relative ionization cross sections. While this does not permit direct determination of the absolute cross section without detailed information of the interaction geometry, it is possible to derive these values by scaling the relative measurements to previously measured absolute cross sections.

3.4 Electron Collisions in a Magneto-Optical Trap

There are several major advantages to performing atomic collisions in a MOT[10]. First, the atoms are confined to a very small region of space (a few millimeters) so that the target can be approximated as a point in space, greatly simplifying analysis. The point source treatment makes it unnecessary to determine the electron or atomic beam profiles as is done in typical cross-beam collision experiments. The trapped atoms have also been cooled[8] to temperatures on the order of μK with velocities of tens of cm/s and the target can be considered stationary during collision events. As target is stationary, even weak collision events can result in sufficient atomic recoil to differentiate them from atoms which have not experienced a collision. A stationary target also has an advantage for excited state collisions since the measured linewidth of an atomic transition will be determined by its natural linewidth rather than the Doppler profile of the atomic velocity distribution. This reduced broadening also means that the transition can be saturated with lower intensity lasers than in other experiments. The cooling process itself is also advantageous for precision collision studies. The atoms are also constantly scattering light from the laser beams and the amount of light scattered from the beams will be directly proportional to the number of atoms within the trap at a given time. Trap losses due to collision events can be determined directly from measurements of the trap fluorescence. Finally, the cooling process can be used for state selection of the collision target. As discussed in Section 2.1, the excited state population at steady state is determined by the parameters of the optical field. This makes it possible to perform collision studies on targets in the ground state or a mixture of ground and excited states by adjusting the trap lasers.

Absolute cross section measurements can be performed by measuring the fluorescence of the trap as a function of time using simple photon counting techniques. Due the high amount of scattering from the trapped atoms, the fluorescence can be used as a direct measure of the trap population at a given time. After a collision event, the number of atoms in the trap evolves as

$$N(t) = N_s(1 - e^{-(\Gamma_o + f\Gamma_e)t})$$ (3.6)

where N_s is the steady-state trap population, Γ_e is the loss rate due to electron collisions, Γ_o is the loss rate due to other collision events and f is the fraction of time the electron beam is on. The loss rate due to electron collisions is related to the cross section by

$$\Gamma_e = \frac{\sigma J}{e}$$ (3.7)

where J is the electron current density at the trap and e is the fundamental charge. Determination

of the cross section is directly related to the fluorescence and this result does not depend on the target density. This removes one of the difficulties associated with other techniques such as crossed beam experiments where measuring the target density is necessary for an absolute measurement.

With state selection, appreciable fractions of the trapped atoms are in both the ground and excited state at any given time, a feature which makes it extremely appealing for scattering experiments. Historically, the production of excited state beams has often been difficult[17], largely due to the often short lifetimes of these states. As such, there is little data available[28] on excited state electron scattering cross sections. In an optical trap, significant excited state populations are produced and cross sections can readily be measured for both ground and excited state atoms.

At steady state, a significant number of the trapped atoms are in the excited state due to the optical pumping process. From the steady state solution (2.15), the excited state fraction for a two-level atom is determined by the intensity and the detuning

$$f_e = \frac{I/I_s}{1 + I/I_s + (2\delta/\gamma)} \tag{3.8}$$

Trapped multi-level atoms reach a steady state fraction with the same functional dependence on the trapping laser detuning and intensities[10, 29, 30]. The trapped target cross section will be a weighted sum of the excited and ground state collisions cross sections determined by the steady state fraction

$$\sigma_{trap} = f_e\sigma_e + (1 - f_e)\sigma_g \tag{3.9}$$

If the repump laser is turned off shortly before the beam is introduced, the trapped target will quickly decay to the dark ground state and the collision cross section is determined strictly by σ_g. Knowing f_e and σ_g, it is possible to determine the excited state cross section σ_e from collisions with the trapped target with the repumper on.

Chapter 4

Experimental Apparatus

To perform electron collisions with a trapped target, it is necessary to have an electron beam, detectors and the apparatus needed for the operation of a MOT. The majority of the experimental setup is dedicated to this final aspect as realizing atomic trapping is non-trivial. The experiment is performed under ultra high vacuum (UHV) due to the conditions needed for trapping and operating the cathode used in the electron gun.

In addition to the vacuum requirements, optical and magnetic fields are needed to establish the MOT. Near infra-red (IR) diode lasers are used to form the trapping and repump beams. Due to the precise red detunings needed for cooling, the lasers are locked to a reference hyperfine spectrum by means of a frequency shifting and stabilization system. The two lasers are merged before passing through a series of optics which create the proper optical configuration for trapping. The magnetic field with linear gradient is created by a pair of anti-Helmholtz coils located inside the chamber.

The electron gun is a highly configurable multi-element unit which produces variably focused beams with energies in the range of $0\,\text{eV}$ to $250\,\text{eV}$. The beam current is measured by a set of Faraday cups in the forward scattering direction and translating wire current probes. Ionized collision products are measured via ion TOF spectroscopy. A multi-element TOF detector with adjustable focusing measures the product ions using multi-channel scaling and gated counting methods controlled by PC interface. All elements of the experiment are precisely timed using a configurable pulse generator for triggering.

4.1   Vacuum Chamber

The trap is loaded from a background atomic vapour within the chamber operated at UHV pressures. Atoms traveling above the capture velocity (2.24) cannot be cooled and trapped by the MOT ($4.42\,\text{cm/s}$ for Cesium[8]). In order to operate the MOT at room temperature, it is necessary to significantly reduce the pressure of the background vapour from which the trap is loaded to below 1×10^{-7} torr.

The vacuum chamber is constructed from 13.25" CF spool 304 stainless steel with a 10.0" inner diameter and electro-polished inner surface. Sixteen side-mount tubes with an outer diameter of 1.5" are mounted symmetrically about the chamber's horizontal plane (Figure 4.1) to allow for optical viewports and to mount various experimental components used in-vacuum. Two windows
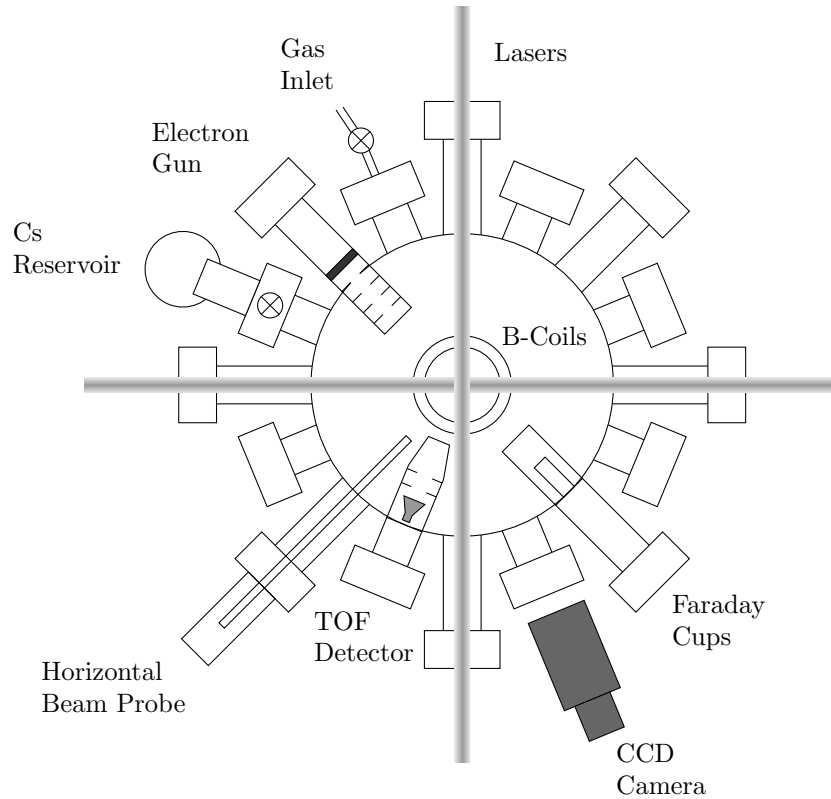
Figure 4.1: Diagram of the vacuum chamber in the horizontal plane. The trapped target is formed in the center of the anti-Helmholtz coils. The horizontal x and y optical beams are also identified. The Faraday cup pair is placed across from the electron gun to measure the current. Horizontal (in plane) and vertical (above plane) beam probes provide more detailed profiles. The trap can be imaged with the use of an external, high focus CCD camera as shown. The TOF detector, Cs reservoir and gas inlet are also labeled and their manual valves denoted with crossed circles.

are also located along the central axis of the chamber at the top and bottom for the vertical beam. The optical viewports are coated with a broadband (centered at $852\,$nm) anti-reflective coating by Applied Physics Specialties in Toronto. The inner surface of the chamber has also been coated with colloidal graphite to reduce the effects of light scattering within the chamber.

The chamber is pumped by a three stage vacuum system and can reach a base pressure below 2×10^{-8} torr. Operating pressures of around 5×10^{-8} torr are maintained by two ion pumps, a Varian starcell ($20\,$L/s) and a Varian triode pump ($100\,$L/s). A Varian VT-70 turbo-molecular pump ($20\,$L/s) backed by a Varian SH-1200 dry scroll pump ($120\,$L/s) are also used. A series of valves can seal both the roughing systems and the ions pumps from the main chamber. A combination of manual and pneumatic valves are used.

Cesium vapour is loaded into the chamber from a reservoir mounted to one of the side tubes. A precision mechanical valve on the reservoir can control the loading rate and the entire arm is separated from the main chamber by a second mechanical valve. The arm is loaded with a glass ampule of elemental Cs which is broken once the reservoir has been evacuated and sealed. Resistive heating tape is wrapped around both the Cs arm and the windows of the chamber, controlled with variable voltage supplies for adjustable temperature control. The tape on the Cs arm heats the
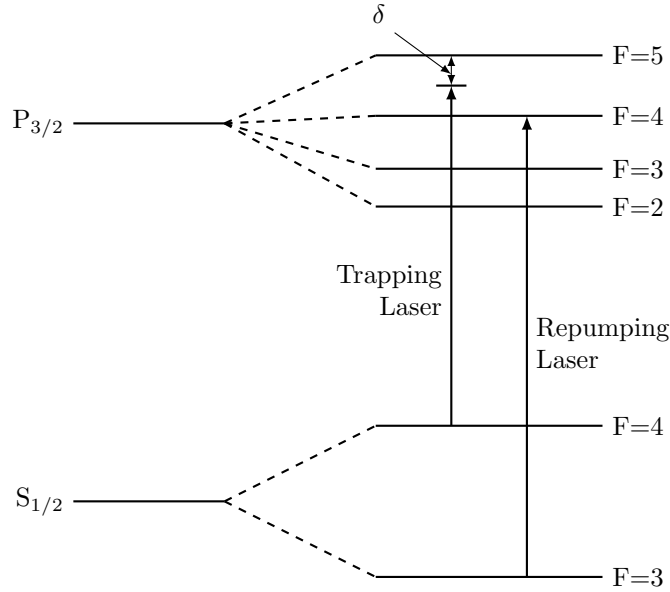
Figure 4.2: Optical pumping scheme used for the cooling and trapping of ^{133}Cs. The cooling and trapping laser is red detuned $F = 4 \rightarrow F' = 5$ transition by a frequency δ while the repump laser is set to the $F = 3 \rightarrow F' = 4$ transition. The detuning and Zeeman splitting widths are over-exaggerated in the diagram.

sample creating the atomic vapour while tape on the windows is used to prevent condensation of Cs on their interior surfaces.

4.2 Laser and Frequency Stabilization Systems

The lasers are operated at 852 nm corresponding to the $^{6}S_{1/2} \rightarrow^{6} P_{3/2}$ transition of neutral Cs. The trapping laser is red detuned from the $F_g = 4 \rightarrow F_e = 5$ hyperfine transition while the repump laser is set near the $F_g = 3 \rightarrow F_e = 4$ transition (Figure 4.2). Semi-conductor diode lasers are used due to their cost effectiveness and fast modulation ability. As the lasers operate in the near infra-red (IR) region, they cannot be easily seen by the naked eye. A small IR sensitive bench top CCD camera can be used to view the beams on a television screen. A second low luminosity, IR sensitive CCD camera with precision adjustable focal length lens has also been mounted outside one of the optical viewports to image the beams and trapped atom cloud inside the chamber.

Both beams are provided by distributed Bragg reflector, single mode, CW diode lasers (SDL 5712-H1 now JDL Uniphase 5400 series) capable of up to 100 mW output power at 852 nm with 180 mA of injection current. The raw laser output is a polarized, diverging elliptical beam with a line width on the order of a few MHz. Both outputs are converted to circular Gaussian beam profiles by means of a collimator and anamorphic lens pair. A Faraday rotator opto-isolator (Optics for Research IO-10-852-HP) placed after the lens pair prevents reflections returning into the laser cavity. Melles Griot O6DLD203A laser drivers provide power and regulate the temperature and drive current of each laser. The drivers have a modulation voltage input which allows for on-line adjustment of the laser drive current for precise frequency adjustment of both beams and locking of the trapping laser. A stabilization circuit referenced to a table-top Doppler free spectroscopy (DFS)
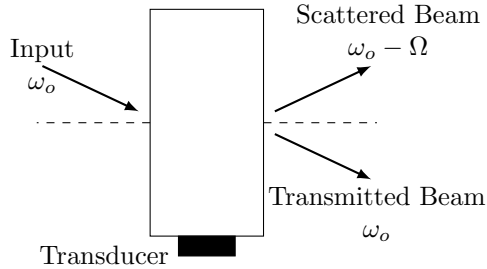
Figure 4.3: An acousto-optic modulator (AOM). The input beam at frequency ω_o enters at an angle and is scattered by the acoustic wave of frequency Ω within the crystal driven by the transducer. A scattered wave at frequency $\omega_o - \Omega$ is diffracted at an angle determined by the Bragg condition.

measurement provides the reference for the feedback modulation.

The cooling and trapping process is heavily dependent on the detuning frequency of the optical field (Section 2.5). An optimal trap is formed when the trapping laser is red detuned from the transition by half the natural linewidth of the transition (2.23). For the $F_g = 4 \rightarrow F_e = 5$ transition of Cesium[13], $\gamma = 32.7686\,\text{MHz}$ which corresponds to a detuning $\delta \approx 19\,\text{MHz}$. Proper operation requires that the lasers hold a precise frequency lock for long periods of data-taking time. Diode lasers have a tendency to experience frequency drift[10] mainly due to thermal fluctuations in the semi-conducting gain medium and the feedback circuit keeps the laser locked to the proper detuning frequency. The feedback voltage modulates the drive current of the laser in real time, keeping the frequency stable and preventing drift. The stabilization system has several components - a DFS setup which provides the hyperfine reference spectrum, a stabilization circuit which accounts for the drift by means of a lock-in technique, and an acousto-optic modulator (AOM) for shifting the laser frequency to the correct detuning.

4.2.1 Frequency Shifting

Acousto-optic modulation is a non-linear optical effect[31] which can be used for precise tuning of the parameters, such as the optical frequency, of an incident field. An AOM is constructed from an ultrasonic transducer coupled to a non-linear crystal within a cavity. The acoustic transducer oscillates at a parameterized frequency, often on the order of $100\,\text{MHz}$, creating a standing acoustic wave within the crystal. If an optical beam of frequency ω_o enters the cavity at an angle θ, the beam is Bragg diffracted by the acoustic wave producing orders of diffraction at multiples of the input angle (Figure 4.3). Due to Brillouin scattering in the crystal, these diffracted beams exit with a shifted frequency $\omega_o \pm m\Omega$ where m corresponds to the diffraction order and Ω is the angular frequency of the acoustic wave. Tuning the frequency of the oscillator can provide precise control of a laser's frequency.

The MOT configuration requires a beam that is red-detuned from the atomic resonance by the appropriate frequency. When performing locking and frequency shifting, one can lock the laser to the $F_g = 4 \rightarrow F_e = 5$ hyperfine peak, down-shift the beam by $19\,\text{MHz}$ to the proper detuning and use the red-detuned light for trapping (Figure 4.4). However, this results in significant intensity reductions in the beam as the shifting process is not 100% efficient and the geometry of the AOM does not permit large beams to pass through. The DFS signal of the $F_g = 4 \rightarrow F_e = 5$ peak is also
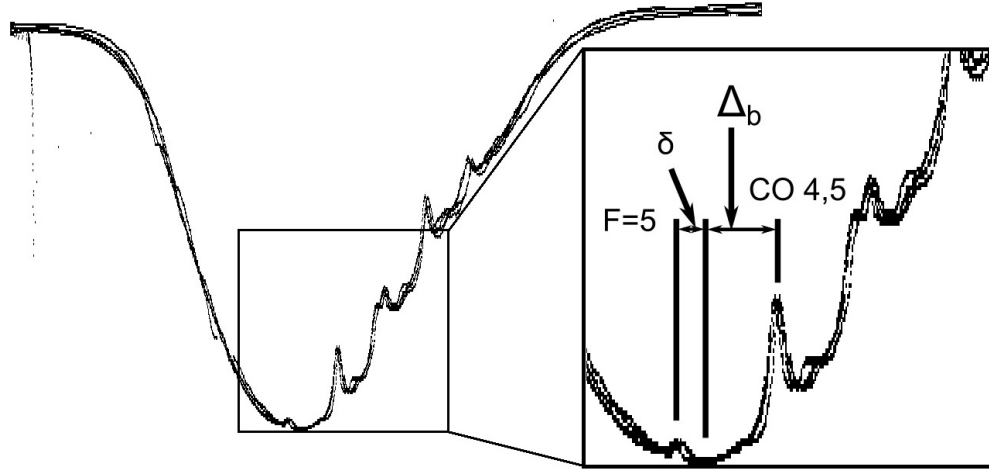
Figure 4.4: Reference hyperfine spectrum obtained from DFS of the Cs vapour cell by sweeping over the Doppler profile of the $F_g = 4$ transition manifold. Rather than lock to the $F_e = 5$ peak and sending a beam detuned by $\delta \approx 20\,\mathrm{MHz}$ to the trap, the beam is down-shifted before spectroscopy and locked to the $F_e = 4, 5$ crossover (CO 4,5) and the unshifted beam is sent to the trap. The crossover is $125\,\mathrm{MHz}$ below the transition corresponding to a blue detuning of $\Delta_b = 105\,\mathrm{MHz}$ from the crossover. Red detuning by δ from the $F_e = 5$ transition or blue detuning by Δ_b from the crossover achieve the same effect.

relatively weak compared to other nearby features making stabilization more difficult. In practice, better locking and increased laser intensity can be achieved by shifting the DFS input beam and sending the *unshifted* beam to the trap. If the beam is locked to the $F_g = 4 \rightarrow F_e = 4, 5$ crossover $125\,\mathrm{MHz}$ below the $F_g = 4 \rightarrow F_e = 5$ transition, with a beam shifted $-105\,\mathrm{MHz}$ from the AOM input, the unshifted beam sent to the trap will be detuned $-20\,\mathrm{MHz}$ from the trapping transition, corresponding to the optimal red detuning for cooling Cs.

4.2.2   Doppler-free Spectroscopy

Doppler-free spectroscopy is a relatively simple optical technique which allows for the determination of atomic hyperfine structure from a gas sample at room temperature with the use of a pump-probe technique. If an atomic gas sample is in thermal equilibrium at a temperature T, the velocities of its constituents are distributed according to Maxwell-Boltzmannn statistics (1.1). If the sample is placed in an optical field with frequency ω_ℓ, the moving atoms see a Doppler shifted (2.20) optical field determined by the atom's speed. The Doppler shifts of the entire sample[7] have a spread on the order of 10^9 Hz. This is two orders of magnitude above typical optical line widths. Even more problematic, hyperfine transitions are often on the order of 10^4Hz and the Doppler shift due to the thermal motion will obscure the hyperfine structure.

Hyperfine resolution can be obtained with a pump-probe setup, as in Figure 4.5. The strong pump beam saturates the atomic transition, decreasing the population difference between the ground and excited states. If the Doppler shifted pump beam is on resonance with the transition, the probe beam will experience less absorption on resonance due to the saturation. When sweeping the frequency of the probe beam, peaks occur at these hyperfine saturated transitions. Additional crossover peaks will also occur midway between each set of hyperfine peaks as additional resonances are introduced
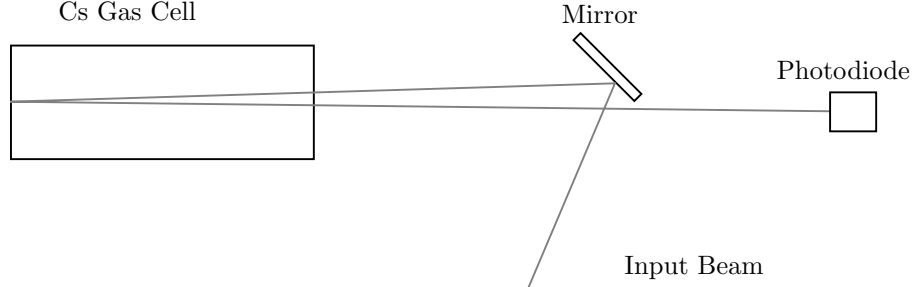
Figure 4.5: Doppler-free spectroscopy setup. The beam is directed into the gas cell and pumps the atoms into the excited state. The rear reflection acts as the weak probe beam which is less absorbed when the frequency is closer to resonance. The photodiode measures the probe beam intensity. Sweeping the laser frequency produces a Doppler-free absorption spectrum.

where the pump and probe beams are at different frequencies which are Doppler shifted to an equal frequency producing a saturation resonance.

The setup used for frequency locking is similar to the one shown in Figure 4.5 and can be seen in the experimental optical configuration in Figure 4.7. The beam is sent into a high purity Cs vapour cell at a small angle, reflecting off the back of the cell into a photo-diode. The incoming beam acts as the pump beam while the weakly reflected beam acts as the probe. Both the trapping and repumping lasers are measured in this manner. In the case of the repumper, a small mirror directs a portion of the beam to the cell as the beam is directed towards the trap (Figure 4.7). It is only necessary that some portion of the repump beam overlaps with the transition frequency and precise locking of this laser is not necessary. The trapping laser however requires stable, specific detuning from the resonance frequency. A beam splitting cube splits the trapping beam, sending one component to the trap and the second through the AOM. Spectroscopy is performed on the shifted beam and locked to the $F_g = 4 \rightarrow F_e = 4, 5$ crossover resonance. The photocurrent is routed through a feedback stabilization to modulate the frequency keeping a lock to the feature.

4.2.3   Stabilization Feedback

Laser drift is corrected by voltage feedback to the laser driver, modulating the drive current to achieve frequency locking. The stabilization system is shown in Figure 4.6. The laser is locked to a hyperfine peak in the DFS (Section 4.2.2) and as the laser drifts, a lock-in amplifier (LIA) provides corrections to keep the measured photocurrent at a maximum, locking the frequency to that of the feature. Voltage modulation and feedback parameters are fine tuned by means of a custom signal mixer which can be manually adjusted. An oscilloscope is used to visualize the hyperfine spectrum when adjusting the lock parameters.

The LIA (Stanford Research Systems SR844) samples the photodiode at a frequency determined by a reference sine wave provided by a sweep generator (Wavetek Model 184). The reference sine sweeps over a small frequency range, resulting in a modulation of the LIA sampling rate of the photocurrent and a scan of its frequency components. The LIA will amplify the component of the input which is in-phase with the reference sine and with the appropriate phase, can act in a maximum seeking mode. As the photocurrent is maximal at the frequency of the resonance peak, the laser remains locked to the transition frequency.
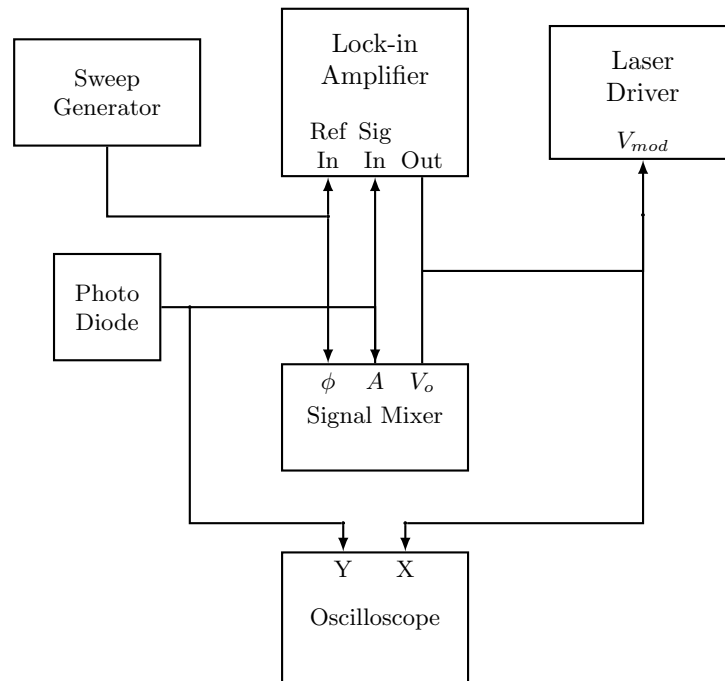
Figure 4.6: Frequency stabilization system. The sweep generator provides a reference sine to the lock-in amplifier (LIA) and mixer. The photocurrent from the trapper DFS measurement is used as the input. A feedback voltage modulated by the LIA and mixer corrects the laser drive current. The signal can be viewed on the oscilloscope plotting the frequency versus the photocurrent in XY mode.

The mixing circuit adjusts the phase and amplitude of the reference wave in addition to providing a final DC voltage offset before feedback is sent to the laser driver. Manual adjustment of the phase ensures that the lock operates in the proper maximum seeking mode while adjusting the amplitude of the reference changes the frequency range over which the beam is scanned. The mixer DC offset can provide small changes to the injection current for frequency control with precisions smaller than the linewidths of the hyperfine transitions.

To aid in the locking procedure, an oscilloscope can be used to provide visualization of the locked feature or the entirety of the hyperfine spectrum. Operating in XY mode, the offset voltage (X) and photodiode current (Y) can be viewed on the oscilloscope. As the LIA scans over the peak, the changes in photocurrent reveal the structure of the underlying hyperfine transitions in that frequency range so that a specific feature can easily be found and then locked to. An external ramp generator can also be used to sweep the laser over a wider frequency range covering the entire Doppler profile of the spectrum.

4.3   Beam Splitting and Polarization Optics

Optical trapping requires a set of three mutually orthogonal beams with polarizations that are properly aligned to the trap's magnetic field gradient. A Cartesian x, y, z system is used with two of the beam sets placed in the horizontal plane with the electron beam and detectors (x and y) and a final set along the chamber axis (z) through the middle of the coils. The beams must be power distributed to provide equal optical forces in all directions and polarized so that a right handed circular beam propagates from negative to positive along the magnetic field (Section 2.5) for a trapping force. As the z beam travels along the central axis of the coils, it experiences twice the field gradient (Appendix C.8) as the beams propagating in the experimental plane. The power ratio of the beams $x : y : z$ must be $2 : 2 : 1$ for equal magneto-optical forces (2.30).

In order to ensure uniformity of the beams, the trapping and repump laser are merged before passing through the splitting and polarization optics which form the trap's optical configuration. The beams are conditioned and portions sent to the DFS setups and the trap (Figure 4.7). A small mirror clips the bottom edge of the repump beam as it enters the optics while a beam splitting cube is used to split the trapping laser sending a portion through the AOM before spectroscopy (Section 4.2.1) and the remainder to the trap. After merging, the beams pass through an adjustable iris to attenuate the beam and then a beam expanding lens pair to maximize the size of the optical trapping area while maintaining low light intensities. The beams then pass through a series of beam splitting cubes, wave-plates and mirrors which create the proper geometrical configuration and correctly polarize the beams.

Polarizing beamsplitting cubes use a layer of dielectric or birefringent material placed along the hypotenuse of the cube to separate the incident light into linear orthogonal components, transmitting one component and reflecting the other[32]. Changing the linear polarization of the incident light will change the transmitted and reflected power. An adjustable half wave-plate placed before the cubes is used to rotate the polarization of the incident beam to achieve the proper optical power distribution.

Before entering the chamber viewports, the beams must be circularly polarized yet the beam cubes output a linearly polarized beam. If the axis of a quarter wave-plate is placed with its fast

axis a 45° angle to the polarization axis, the beam can be circularly polarized before entering the chamber. Rotating the wave-plate axis 90° will reverse the handedness of the light. A second quarter wave-plate on the opposite side of the chamber reverts the beam to a linear polarization before a retro-mirror reflects the beam back along its path to produce the necessary counter-propagating arrangement. As the beam passes through the quarter wave-plate again, it is circularly polarized with the *opposite* handedness due to the reflection at the mirror. The polarizations must be aligned with the magnetic field so that the right handed beam travels along the direction of increasing B. If the polarizations are reversed, the magneto-optical forces will push the atoms out of the trap rather than confine them.

Proper geometrical alignment of the beams is also essential as using non-orthogonal beams introduce asymmetries that will result in non-zero net forces which may push atoms out of the trap. The horizontal current probe can be placed in the center of the trapping region and used as a reference point in alignment of the horizontal beams. Proper retro-reflection of the laser beams is also important. Using the bench cameras and a small collimator placed in the beam line far from the trap, small deviations from true retro-reflectance can be observed on the surface of the collimator around its aperture. In practice however, a small angular deviation may need to be introduced as light reflected directly back towards the laser cavity can cause beam instability.

4.4   Magnetic Field

A set of anti-Helmholtz coils (Appendix C) located inside the chamber provide a magnetic field with the proper linear gradient needed for trapping. The coils were constructed by Stephen Brotton, consisting of 200 turns of 24AWG Kapton insulated wire (Figure 4.8) producing a magnetic field gradient of over $10\,\text{G/m}$, operated with $1\,\text{A}$ to $2\,\text{A}$ of current. A regulated current supply connected via vacuum feed-through provides the coil current.

If the electron beam is introduced while the magnetic field is on, it will exert a force on the beam deflecting it away from the trapped target. Therefore it is necessary to turn off the field and wait until it has fully decayed before introducing the electron beam. As the trapped target can warm up[8, 10] on the order of hundreds of ms, a fast-switching circuit[33], designed and built by Siniša Jezdić is used to quickly turn the field on and off.

The circuit (Figure 4.9) is controlled by a TTL/CMOS control voltage, allowing or preventing the flow of current to the coils. Due to inductance, the coil response is not immediate and the strength of the magnetic field decays to zero over a period of approximately $1\,\text{ms}$. This needs to be taken into account when timing the electron beam. The field also has a finite rise time but it is far smaller than the time scales needed to load the trap (tens of μs vs tens or hundreds of ms) and do not need to be considered.

4.5   Electron Gun

The electron gun currently installed in the trap was designed by Dr. P. Hammond in 1986 and constructed in the University of Windsor machine shop. The filament is contained within a detachable Wehnelt cylinder followed by primary deflection and focusing stages, a secondary deflection stage, and a pentode lens stack for final focusing. The schematic can be seen in Figure 4.10. The gun uses
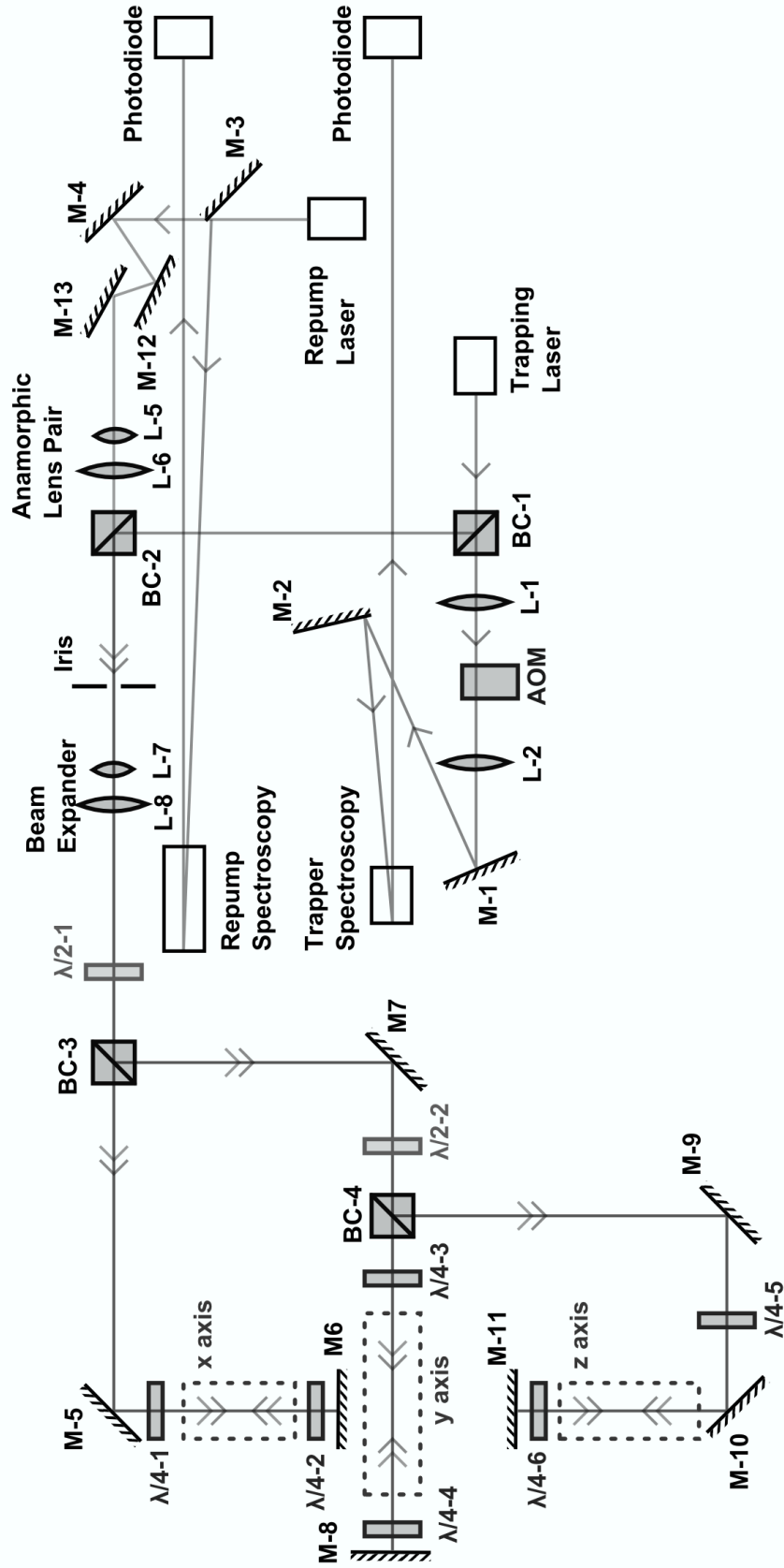
Figure 4.7: Beam splitting and polarization optics including frequency shifting and DFS optics. Lenses (L), beam splitting cubes (BC), mirrors (M) half ($\lambda/2$) and quarter ($\lambda/4$) wave-plates are shown. Original figure created by Jeff Hein.
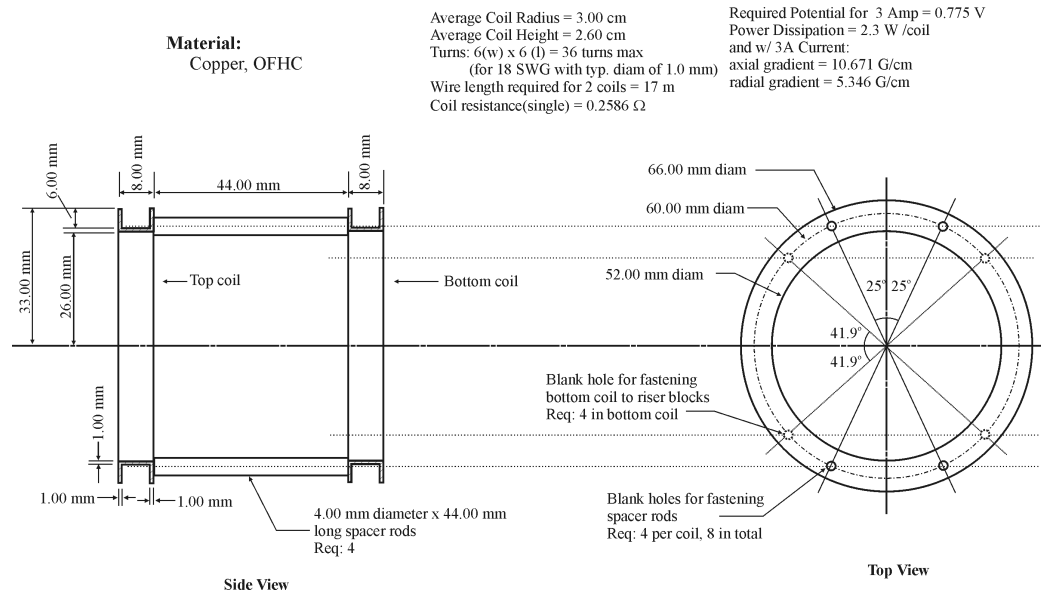
Figure 4.8: Schematic of the anti-Helmholtz coil assembly. Figure reproduced from MacAskill[14].

a Barium Oxide (BaO) cathode from Kimball Physics that operates at approximately 1000 K with a maximum emission current of 3 mA and current densities of approximately 0.25 A/cm. The cathode is designed for use under UHV and is extremely sensitive to atmospheric molecules (especially O_2) which can poison the surface of the cathode, permanently damaging it.

A pulsed electron beam can be generated by changing the voltage of the Wehnelt cylinder enclosing the cathode. Driving the cylinder approximately 20 V below the cathode potential will block the flow of current, acting as a sort of "grid". The grid voltage is controlled by a fast-switching transistor based circuit responding to an "on/off" TTL control voltage. When "off", the grid is brought below the cathode voltage and then taken back up when "on".

Deflector and lens bias supplies are connected in a floating arrangement (Figure 4.11) to easily reference the lens potentials to the extraction voltage. A custom control module regulates the voltages supplied to the various elements and is connected via a UHV feedthrough cable to the electron gun. The module also encloses other conditioning and computer interface electronics for the current probes (Section 4.6).

It is also possible to vary the energy of the electron beam with the use of an external ramp generator. A high voltage amplifier can replace or supplement the cathode supply (PSU1 in Figure 4.11) to allow the cathode energy to be varied through automated control. The amplifier is capable of providing linear 50x voltage amplification of a 0 V to 2.5 V input pulse to a range of 0 V to 125 V with a variance of less than 3 mV.

4.6   Current Measurement Systems

A set of Faraday cups opposite the electron gun are the primary means of measuring the emission current. There are also two thin-wire beam probes which can be used to perform more detailed measurements of the electron beam cross section. Both systems can be read out by external ammeters or a PC interface. Deep cups are used in order to avoid scatter from secondary electrons. The
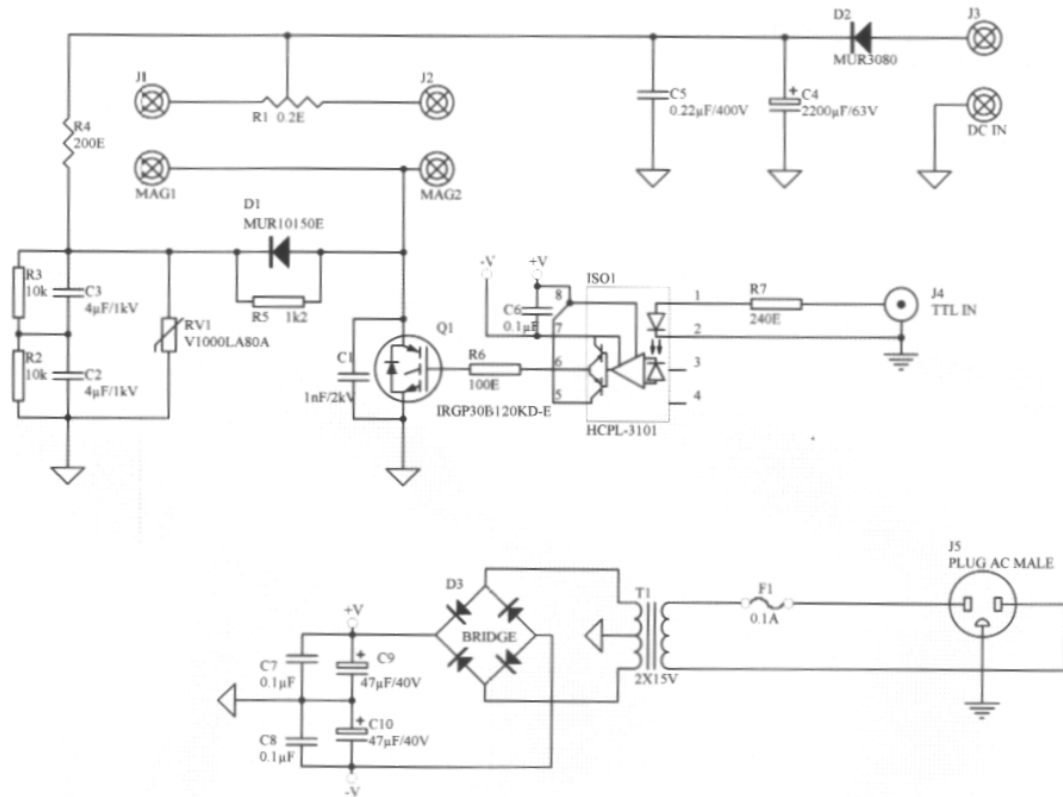
Figure 4.9: Circuit diagram of magnetic field switch. The current flows in the presence of a TTL/CMOS control voltage. The field will be turned off in the absence of voltage. The dissipation time of the field is less than 1 ms. Figure reproduced from MacAskill[14].

outer cup has a length of 2.00" with a length-to-diameter ratio $L/D \approx 3.33$ while the inner cup has $L/D \approx 5$. The cups can both be optionally biased with approximately 0-40V by independent bipolar DC voltage supplies. Currents from the inner and outer cups are measured by two high precision HP 3457A multimeters or can be directed through conditioning electronics to a PC interface.

More precise profiles of the emission current can be obtained with a pair of horizontal and vertical beam probes located inside the chamber. These 0.010" diameter stainless steel wire probes are mounted on linear translators which can be moved µm distances for detailed measurements of the electron beam profile at different locations. The horizontal probe is mounted on a linear track driven by a UHV feedthrough, manual micrometer drive. The vertical probe is located on the top of the chamber and fed through a flexible UHV flange mounted on a horizontal stage. A linear manual micrometer drive controls the motion of the probe vertically and the horizontal stage is capable of micrometer translation of the probe in the horizontal plane. A variable positive or negative bias of 0-18V can be applied to each probe. The current can be measured with an analogue ammeter or via a PC interface similar to the Faraday cups.
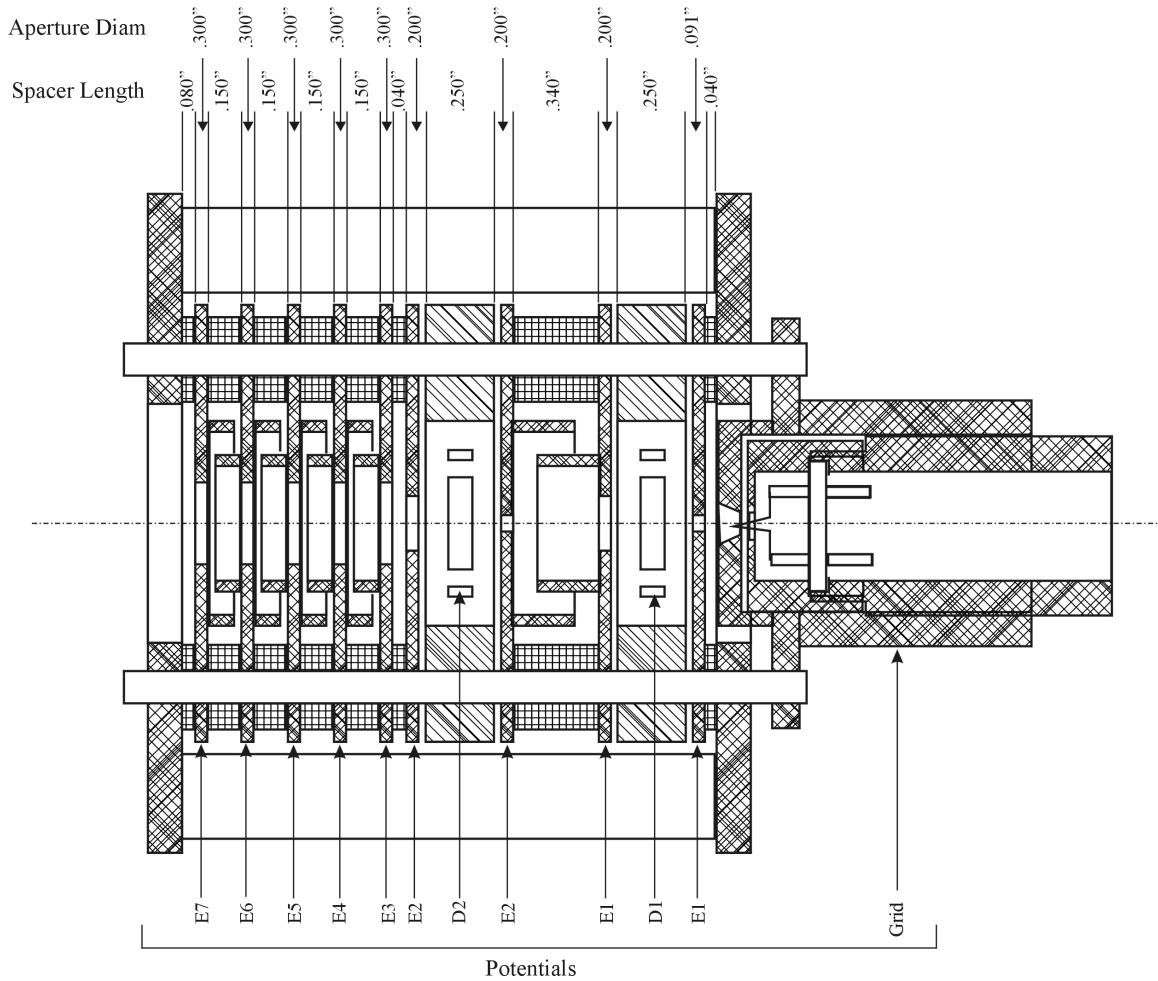
Figure 4.10: Schematic of electron gun system. Figure is reproduced from MacAskill[14].

4.7 Time-of-Flight Detection

4.7.1 Principles of Time-of-Flight Measurement

Ion time-of-flight (TOF) spectroscopy measures the mass distribution of ions collected by a TOF detector. An electric field applied to the ions accelerates them proportionally to their mass-to-charge ratio separating them in time as they arrive at the detector. Suppose that some ion near the detector has a charge q and mass m. The sign of the charge has not been specified. The principle of TOF spectroscopy is the same for both positive and negative ions and the only difference will be in the choice of potentials used for extraction. Below, it is assumed that the ions have positive charge.

Consider the one-dimensional motion of an ion in the presence of an extraction field. The electric field $\mathbf{E}$ exerts a force in the accelerating region on the ions

$$F = qE \tag{4.1}$$

In the absence of any external forces, Newton's second law states that the ion will experience an

PS 1 : Cathode Current Supply
 (Tenma 72-705)
PS 2 : Beam Energy Power Supply
 (Lambda LPD-425A-FM)
PS 3 : Positive Lens Power Supply
 (Kepco HB2AM)
PS 4 : Negative Lens Power Supply
 (Kepco HB2AM)
DPS 1 : First Deflector Stage Power Supply
 (Lambda LPD-425A-FM)
DPS 2 : Second Deflector Stage Power Supply
 (Lambda LPD-425A-FM)
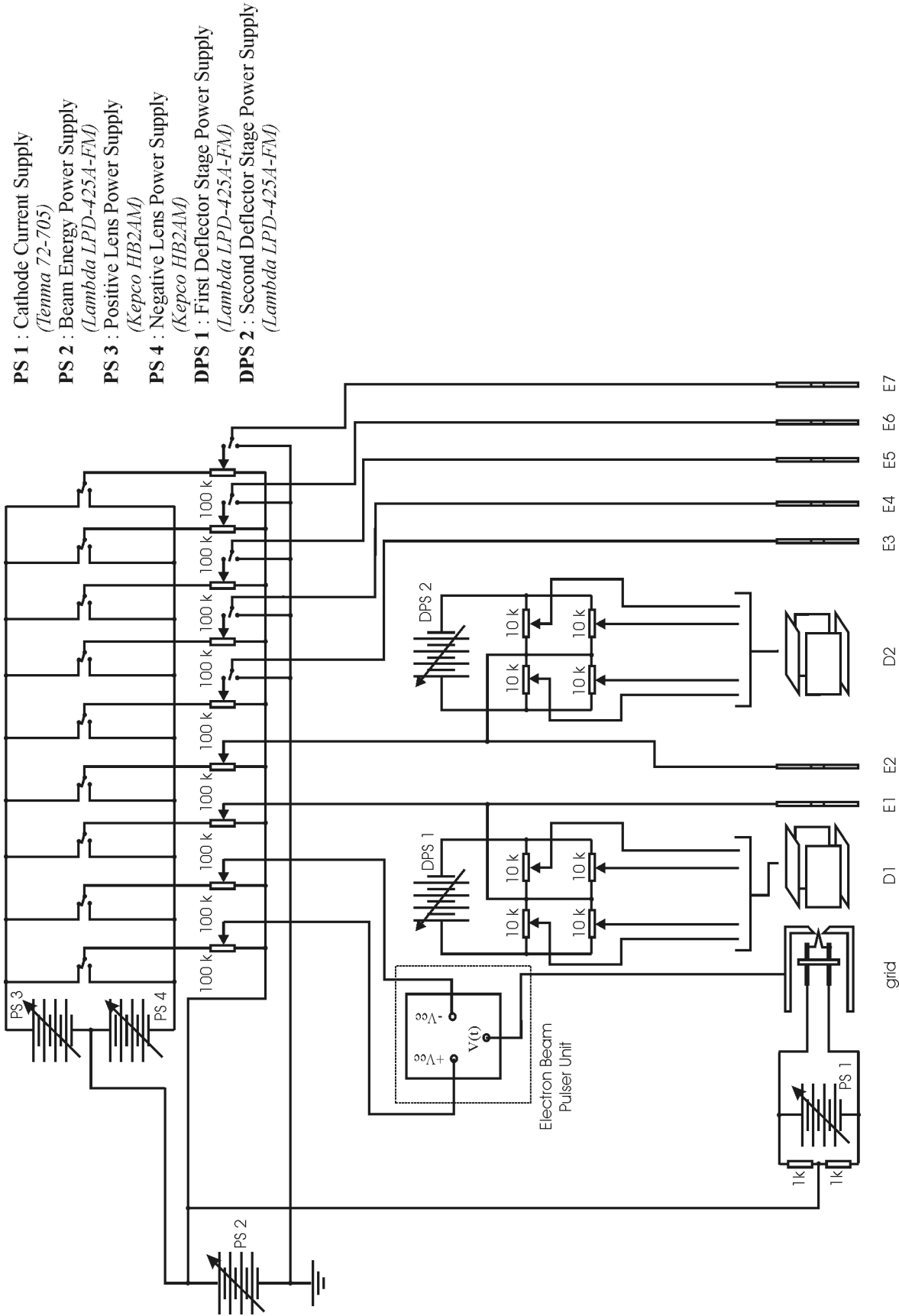
Figure 4.11: Diagram of electron gun control circuitry. Potential elements are held relative to the cathode (PSU1). Deflector elements (D1,D2) are powered by separate units from the focusing plates (E1-E7). Figure taken from MacAskill[14].

acceleration a given by

$$a = \frac{F}{m} = \frac{qE}{m} \tag{4.2}$$

As the ion accelerates, its velocity at a given time t is determined by the integral equation

$$v(t) = \int_{t_o}^{t} dt \, \frac{qE}{m} = v_o + \frac{qE}{m} t \tag{4.3}$$

where v_o is the ion's initial velocity at time t_o. The ion can be accelerated to a velocity v_a in a time

$$t_a = \frac{m}{q} \frac{v - v_o}{E} \tag{4.4}$$

It is also possible to determine the position of the ion after a time t from the integral

$$x(t) = \int_{t_o}^{t} dt \, v(t) = x_o + v_o t + \frac{qE}{2m} t^2 \tag{4.5}$$

For simplicity, assume that the ion begins at rest with $v_o = 0$. After passing through the accelerating region, the ion will have acquired energy due to the applied force

$$U = \int_{x_i}^{x_f} dx \, F(x) = qE x_a \tag{4.6}$$

where $x_a = x_f - x_i$ is the distance over which the ion has been accelerated. The ion therefore picks up additional kinetic energy

$$\frac{1}{2} m v_a^2 = qE x_a \tag{4.7}$$

and the ion's velocity upon entering the drift tube is then

$$v_d = \sqrt{\frac{2qE x_a}{m}} \tag{4.8}$$

The ion will pass through the drift tube of length D in a time

$$t_d = \frac{D}{v_d} = \sqrt{\frac{D^2 m}{2qE x_a}} \equiv \kappa \sqrt{\frac{m}{q}} \tag{4.9}$$

where κ only depends on the detector configuration *not* the properties of the ion. The ion's TOF can be seen to be proportion to the $\sqrt{m/q}$. With TOF spectroscopy, it is possible to differentiate species of charged particles through the use of time resolved detection methods.

4.7.2   TOF Detector System

The current TOF detector was constructed here in the machine shop and was designed and assembled by Stephen Brotton. It consists of a channel electron multiplier (channeltron) behind a bias grid, an approximately 100 mm field free drift tube, as well as focusing and deflection elements. A schematic of detector is shown in Figure 4.13. Cylindrical electrodes act as axial lensing elements to focus the ion beam onto the detector. Deflection plates also allow for corrections of ion trajectories due to misalignment of the target. Stray fields from the detector are suppressed with a grounded metal
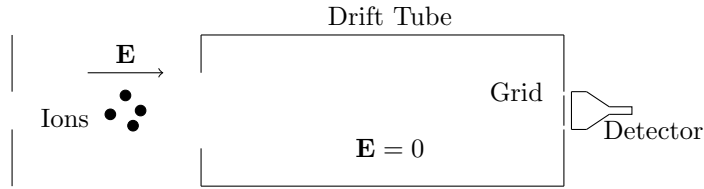
Figure 4.12: A basic time-of-flight detection system. Ions are generated by some process and are extracted with the accelerating potential. The ions are drawn into the drift tube. The entire tube is held at a constant potential to create a field free region. Ions are collected at the detector and measured by the data acquisition system.

shield fitted over the detector.

The TOF spectrometer is mounted in one of the side tubes in the experimental plane at a $67.5°$ angle to the forward scattering direction (Figure 4.1). The front of the detector is placed a few millimeters away from the center of the trap for maximum ion collection. The position of the front face is as close to the trapping region as possible without blocking the line of sight of the optical beams to the center.

The lens biases are provided through a UHV feedthrough from a custom control module (Figure 4.14) designed by Siniša Jezdić and constructed by Stephen Brotton. Three cylindrical lens elements are independently, negatively biased with $0\,V$ to $-24\,V$ for axial focusing. The horizontal and vertical deflectors also have variable biases which are made bi-direction with an inverting switch. The channeltron receives positive high voltage from an Ortec 659 HV Bias NIM module. A low pass filter (Figure 4.15) removes high frequency noise from the voltage signal received from the bias supply. Output pulses from the channeltron go directly to a pre-amplifier module and are amplified to a few hundred mV.

Optimization of the detector focusing plays an important role in ion resolution. However, resolution is also limited by the velocity and spatial distributions of the collected ions which adds further broadening of the ion distribution. For thermally distributed atoms the resolution, determined by the full width at half maximum (FWHM) of the ion distributions (Figure 4.16), which is approximately one m_u/e unit. For trapped targets, this distribution can be significantly narrowed[7, 8] resulting in improved TOF resolution.

4.7.3   Ion Counting

A fast timing filter amplifier (Ortec 474) further increases the voltage of the pre-amplifier pulses before being counted. Counting is performed using a multi-channel scaler (MCS) or gated pulse counters interfaced to PC systems. Time resolved ion TOF spectra are obtained using MCS counting and the use of gated counters allows for cross section measurements of specific ions while varying the projectile energy to obtain the excitation function.

The MCS is a FastCom P7882 PCI card which interfaces with proprietary software to acquire spectra has a minimum dwell time of 100 ns. An on-board analog-to-digital (ADC) converter allows for counting of the amplified pulses without introducing additional signal processing. The scaler is triggered to start by an external pulse generator (Section 4.8).

The gated counter (Standford Research Systems SR400 Dual Gated Photon Counter) is interfaced
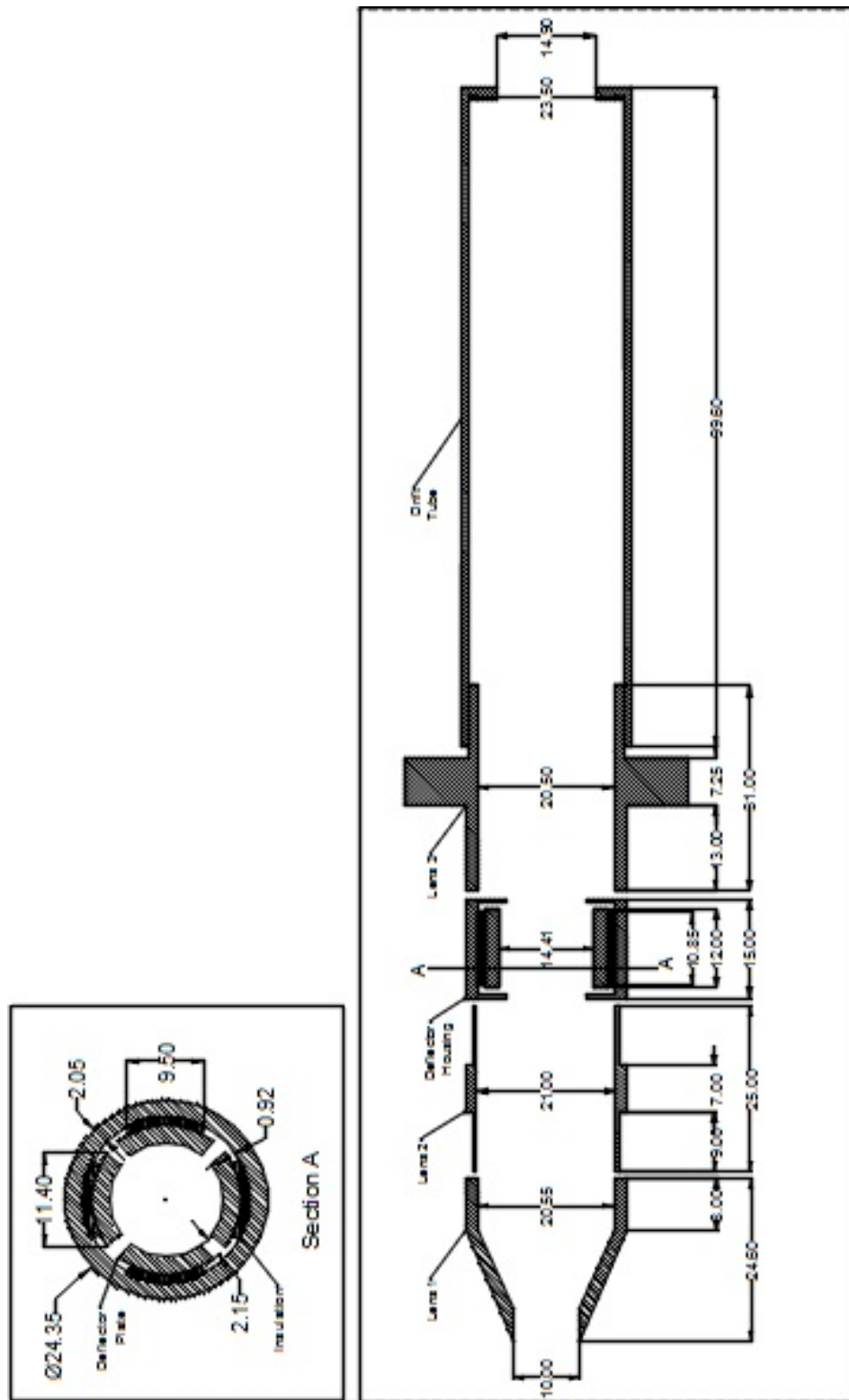
Figure 4.13: Schematic of time-of-flight detector system. The detector is equipped with three lens elements and sets of horizontal and vertical deflector plates (Section A). Not shown are the channeltron detector and final voltage grid placed after the drift tube.

Figure 4.14: Circuit diagram of time-of-flight detector control box. The unit can supply variable, independent 0 V to 24 V potentials to the lens elements V1, V2 and V3, grid potential V4 and the horizontal and vertical deflector plates X and Y. The deflectors can also be inverted. Both the design and diagram were created by Siniša Jezdić.
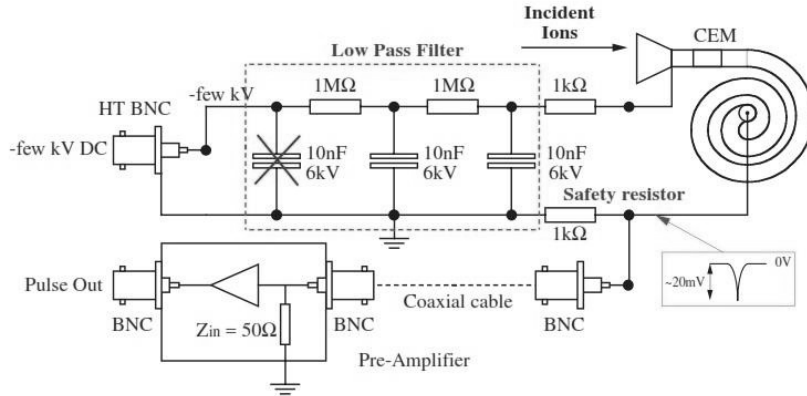
Figure 4.15: Ion TOF detector bias circuit powered by an external high voltage supply. A low pass filter removes noise from the bias voltage before being applied to the channeltron (CEM) detector. Output then goes to a pre-amplifying module (also shown) before processing. Graphic originally produced by Stephen Brotton.

by serial RS-232 communication to a PC which externally controls the unit through a custom software interface developed by Jeff Hein. When the external start trigger is received, two counting windows with variable delays and widths are then created to detect specific mass groups from the spectrum based on their TOF (Figure 4.17). The PC software is capable of configuring counting windows and providing more advanced control of the unit's functionality. The SR400 also has an auxiliary voltage output which can be used to vary the extraction voltage of electron gun. In this manner, specific ion cross sections can be measured as a function of impact energy.

4.8 Experimental Control

Precise timing is necessary in order to perform collisions with a trapped target as the collision must be performed after the field has decayed but before significant expansion of the atomic cloud occurs. Ion detection must also be timed to start a few µs after the end of the electron pulse. A Berkley BNC 555 Pulse Delay Generator was used to provide master triggering for all timed aspects of the experiment. The module can produce fully customized pulse sequences to up to 8 outputs with individual delays, pulse shapes and widths and voltages.

A typical experiment with a trapped target has a duration of about 500 ms (Figure 4.18). The field is left on for a period of about 400 ms to form the trapped target. The field is then turned off for a period of 20 ms. The electron beam is introduced after a 1 ms delay to allow the field to decay. After the electron pulse, the detector is triggered and a TOF spectrum is acquired. As the magnetic field can also affect scattered ion trajectories, it is turned back on after the end of the scan which are less than a few ms in duration.
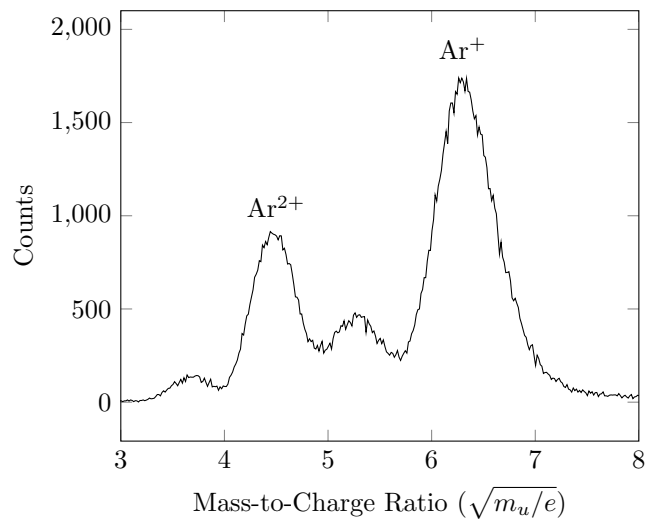
Figure 4.16: Example ion TOF spectrum for electron collisions with a thermal Ar beam at $200\,\text{eV}$. The Ar^+ and Ar^{2+} ion peaks are marked. For thermal atoms, resolution is approximately one m_u/e unit but this is dependent on the initial distributions of the ions.
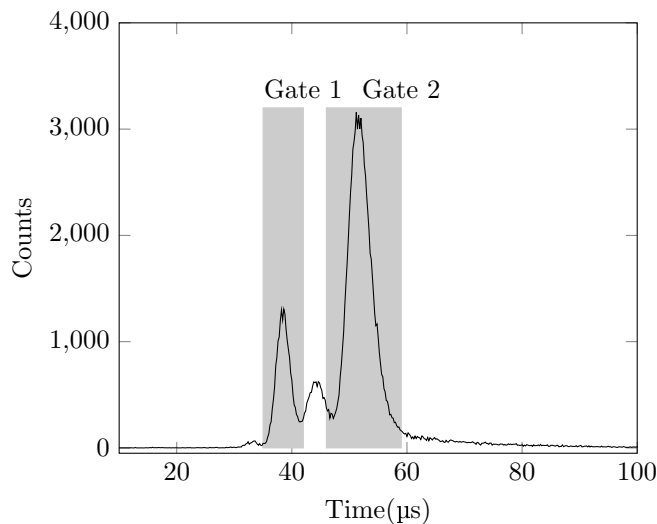
Figure 4.17: Example of gated ion counting for some TOF distribution. Two gates are delayed from the start trigger at $0\,\text{µs}$ and each have a set time width. The gates can be set to coincide with specific ion groups as shown with the two gray boxes.
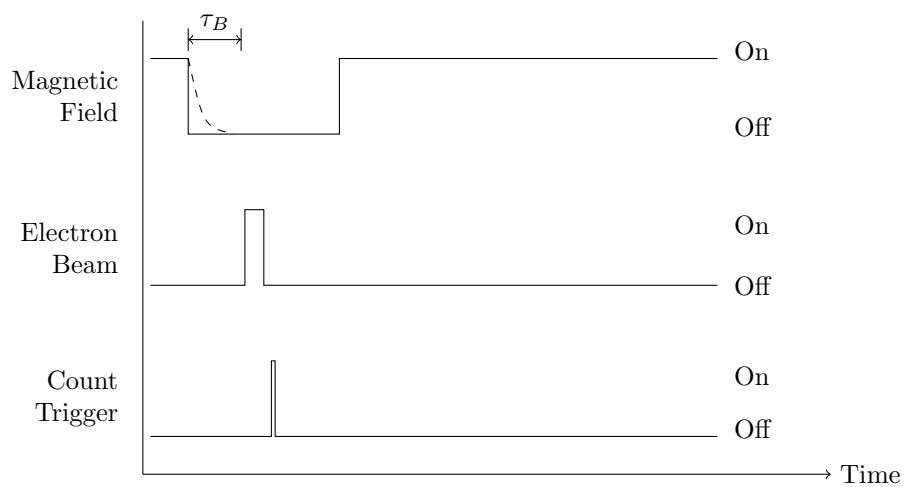
Figure 4.18: Typical timing sequence for a collision experiment with a trapped target lasting about 500 ms. The magnetic field is turned off for a period of about 10 ms to 20 ms. After the field is allowed to decay for a period $\tau_B = 1$ ms, an electron pulse is introduced with a width of a few µs. Shortly after the end of the electron pulse, the ion counter is triggered. Typical TOF scans are less than 1 ms in duration. The field is turned on after the end of the scan and the trap is reloaded for another measurement.

Chapter 5

Electron Impact Ionization of Argon

Studies of electron collisions with Argon (Ar) were performed to assess the performance of the TOF detector and evaluate the viability of different ion counting methods for use in future experiments. Using an injected gas rather than Cs vapour as the target, higher operating pressures and total count rates could be readily obtained while also removing the complexities associated with using a trapped target. This allows for the detector performance to be evaluated with improved reliability and reduced data acquisition time. Detector resolution was from spectroscopy of single and double Ar ions which are readily produced at the gun's operating energies. Methods such as gated ion counting can be evaluated by comparing resulting to literature which can demonstrate a proof of concept for measurements of other, less well known systems.

Argon is an inert, noble gas with closed outer electron shell whose most abundant isotope ^{40}Ar makes up a little more than 0.9% of the Earth's atmosphere (Table 5.2). It is used in many scientific and industrial applications including attosecond pulse generation[7], searches for dark matter[34], welding[35] and fire suppression systems[36]. While the BaO cathode used in the electron gun (Section 4.5) is highly reactive with atmospheric molecules, Ar makes an appropriate target for use with the installed electron gun due to its non-reactivity and cost effectiveness. Its atomic mass also makes it more analogous to Cs in mass spectroscopy measurements than He, another commonly used noble gas target. The electron collision properties of Ar have also been well studied[17, 26] with accurate multiple ionization cross section data available over a wide energy range[37, 38]. The ionization potentials of Ar can be found in Table 5.1 and cross section data in Appendix A.

5.1 Experimental Method

Electron impact of Ar was performed with a crossed beam setup and collisions ions measured with ion TOF spectroscopy. The objective of the measurement was twofold. The first goal was to assess the detector resolution and optimal operating parameters. Second was to measure the relative cross sections of doubly ionized Ar (σ^{2+}/σ^{+}) and possibly other multiple ionization ratios σ^{n+}. As these values are well known[17, 37, 38], comparison can be made to known literature values for assessment of the detector.

Ion Species	Mass-to-Charge Ratio ($\sqrt{m_u/e}$)	Absolute Ionization Potential (eV)
Ar^+	6.32	15.759 611 2(5)
Ar^{2+}	4.47	43.389 28(12)
Ar^{3+}	3.65	84.124(12)

Table 5.1: Single and multiple ionization potentials of neutral ^{40}Ar. Data is taken from the NIST atomic database[19].

Molecule	Mass ($\sqrt{m_u/e}$)	Ionization Potential (eV)	Dry Air Abundance (%)
Oxygen (O_2)	5.66	12.07	20.946
Water (H_2O)	4.24	12.62	-
Carbon Dioxide (CO_2)	6.63	13.78	0.0370
Nitrogen (N_2)	5.29	15.29	78.084
Argon (Ar)	6.32	15.76	0.934

Table 5.2: Atomic mass, single ionization potentials and dry air (no H_2O) abundances of possible atmospheric constituents. Masses and ionization potentials are taken from [19] and abundances from [39]. Water may also be present in some amount according to local humidity.

A constant atomic gas beam was injected via the inlet valve (Figure 4.1) of the vacuum chamber. Injection was controlled by a manual variable leak valve (Granville-Phillips 203) from a compressed gas cylinder of UHP 5.0 ^{40}Ar purchased from Praxair Canada. The chamber was operated at an ambient pressure of approximately 7×10^{-6} torr maintained by the turbo and roughing pumps (Section 4.1) as this was above the standard operating pressures for the ion pumps which were sealed off for the experiment. The gas tubing leading up to the leak valve uses Swagelok fittings and valves, which are not designed for use in UHV environments and atmospheric molecules can leak into the system through the tubing, contaminating the atomic beam. These molecules can also ionize during collisions, producing additional ion peaks in the TOF spectrum. While nonreactive with noble gases such as Ar, the BaO cathode is highly reactive with some atmospheric molecules and so experimental runs were limited to reduce the possibility of damage.

Collisions were performed with $3\,\mu s$ to $5\,\mu s$ wide electron pulses pulsed at $1\,kHz$. The energy of the gun was calibrated to the single ionization potential of Ar with an energy resolution of $\pm 0.5\,eV$. Emission currents varied with energy but averaged approximately $50\,nA$ to $150\,nA$. The observed emission was orders of magnitude less than the $3\,mA$ maximum reported current of the cathode and is an indication of possible poisoning or other damage. Replacement requires that the vacuum chamber be opened to remove the gun and considerable time may involved in this process due to the need to open up the chamber to atmosphere. Rather than opt for replacement during this study, the installed cathode was used and studies were performed with reduced emission current and lower count rates. However, if the electron distribution is assumed to be approximately uniform then representative relative measurements can still be obtained with ion spectroscopy. The reduced current prevented detailed profile measurements as the wire probes could not collect sufficient current to produce an appreciable reading. The electron beam profile was instead estimated from measurements of the transmission current incident on the outer and inner Faraday cups.

For acquisition of TOF spectra, short electron pulses are ideal as collisions occur with the target

over the entire pulse length so that longer pulses result in broader TOF peaks. However, pulses shorter than about $3.5\,\mu s$ could not be produced due to hardware limitations. The electron gun is switched by a Wehnelt cylinder which defocuses the beam "off" by applying a strong negative potential relative to the cathode. Capacitive and space charge effects within the system may create fields which prevent formation of shorter pulses. Switching the circuit at $3.5\,\mu s$ also corresponds to a frequency of about $286\,MHz$ which could represent a limit of the response time of the transistor and may be another possible cause of this limitation.

The resolution of the detector is heavily influenced by the potential configuration of the electrodes which form the extraction field. Varying the voltage on the front cylinder can be used as a means of adjusting the overall strength of the extraction field. Focusing and ion steering can then be achieved with adjustment of the remaining potential elements relative to the front lens. Resolution will be determined both by the overall field strength and the axial focusing, which can be optimized for a given field strength. The detector's resolution was determined from Ar ionization spectra taken with extraction fields of $0.5\,V$ to $10\,V$. After the detector was optimally focused for a given field strength, ion peak widths and time separations could be used to assess the resolution of the detector.

Relative cross section measurements of Ar ion production in electron impact collisions were also obtained and compared with the generally accepted measurements of Straub et al[37]. Cross sections were determined directly from the TOF spectra and from excitation functions obtained with gated ion counting (Section 4.7.3). With the direct method, collisions were obtained for energies of $50\,eV$ to $200\,eV$ corresponding to a range where both single and double ionization cross sections are high. For excitation function measurements, the cathode supply was replaced with a high voltage amplifier ramped by a control voltage. With this method cross sections were measured from threshold to $120\,eV$, the maximum voltage output of the amplifier, to produce excitation functions.

While the absolute cross section is dependent on the electron and atomic beam parameters, relative cross sections can still be determined directly from ion TOF spectra. In the case of excitation functions, any energy dependent changes in the electron beam density must be removed to obtain accurate cross section data. The beam was focused to be ideally uniform across the energy range as determined from the Faraday cups. The total emission current was also measured across the energy range in order to correct for changes in electron density.

5.2   Results

A comparison of spectra taken with different extraction fields can be seen in Figure 5.1 where the spectra have been mass calibrated. Significantly improved mass resolution can be seen with larger extraction voltages. In all of the spectra, two prominent peaks can be seen corresponding to Ar^+ and Ar^{2+}. However, a third peak can be seen at higher potentials (5.1d and 5.1e) corresponding to N_2^+ which is obscured at lower voltages (5.1a - 5.1c). Part of the obfuscation is due to asymmetric peak tails which become even more pronounced with small extraction fields. These tails can be attributed to certain experimental factors which are discussed further in Section 5.3. On the basis of these results, the TOF detector was operated in a well focused configuration with $9\,V$ on the front lens of the detector for further measurements. These initial spectra also (Figures 5.1d and 5.1e) indicate the presence of atmospheric gases in the atomic beam. As previously noted, this is expected when using fittings not specifically designed for use in UHV systems. Due to their abundances (Table 5.2),
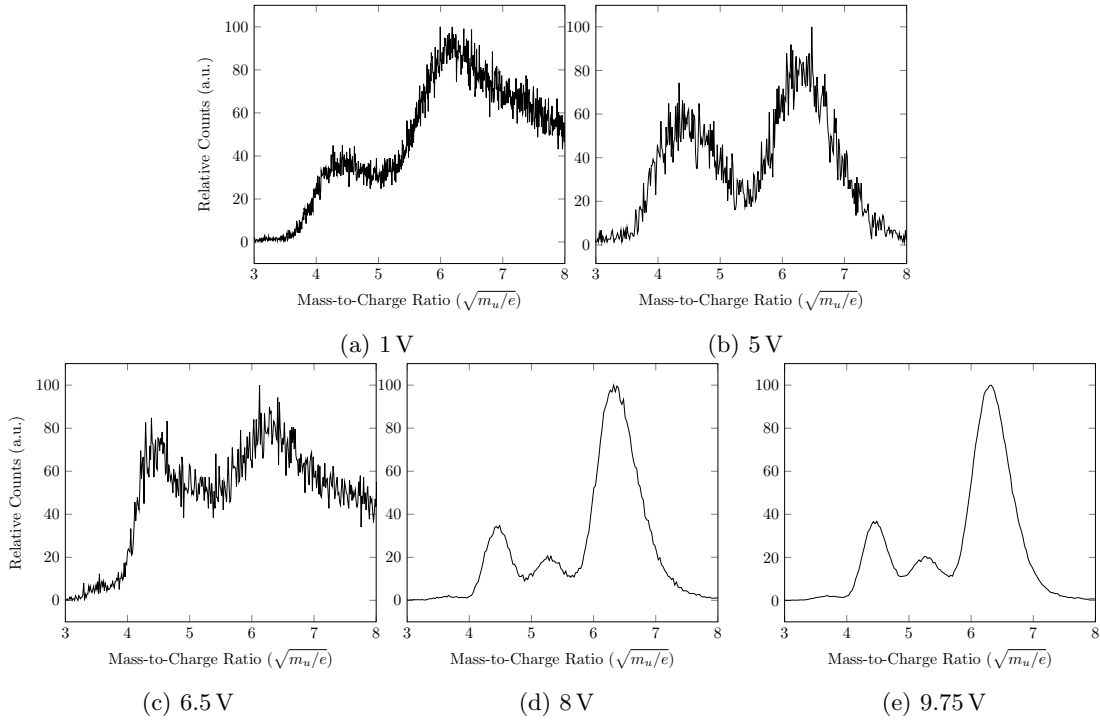
Figure 5.1: Detector resolution with extraction potentials of 1 V to 10 V. The TOF spectra have been normalized and then mass calibrated to the single and double Ar ionization peaks. Impact energies vary from 50 eV to 200 eV which accounts for differences in relative peak heights. Non-Gaussian tails can be seen on the slow end of the TOF peaks resulting from the collision distribution. Larger extraction fields suppress this tail and also increase the collection efficiency dramatically improving results.

the most significant[39] constituents are N_2, H_2O and O_2.

5.2.1   Ion TOF Spectra

An optimal ion spectrum is shown in Figure 5.2 for collisions at 200 eV. The spectrum was mass calibrated assuming that the three most prominent peaks correspond to Ar^+, Ar^{2+} and N_2^+ as marked in the diagram. This assumption was later verified using other results of this study. Examination of Figure 5.2 also reveals the presence of several atmospheric constituents. A clear N_2^+ peak can be seen between the single and double Ar ionization peaks. H_2O^+ is also expected to be present. Due to their similar mass ratios however, this ion peak is heavily overlapped with Ar^{2+}. O_2 is also likely present but also significantly overlaps with the neighbouring N_2^+ and Ar^+ peaks and its presence cannot be confirmed. At the light end of the spectrum, one can also observe Ar^{3+} and N^+ which overlap due to their similar mass ratios.

The four general features observed in Figure 5.2 (Ar^+, N_2^+, H_2O^+/Ar^{2+} and Ar^{3+}/N^+) were each fitted with Gaussian peaks using least squares fitting. The centers and FWHMs are shown in Table 5.3. With FWHMs of almost 1, the combined Ar^{2+}/H_2O^+ and Ar^{3+}/N^+ peaks widths are far greater than the difference in mass ratio of the two species constituting each peak (0.23 and 0.09 respectively). Certainly with these severe degree of overlap, attempts to meaningfully separate the two constituent ions in each peak will be fruitless.
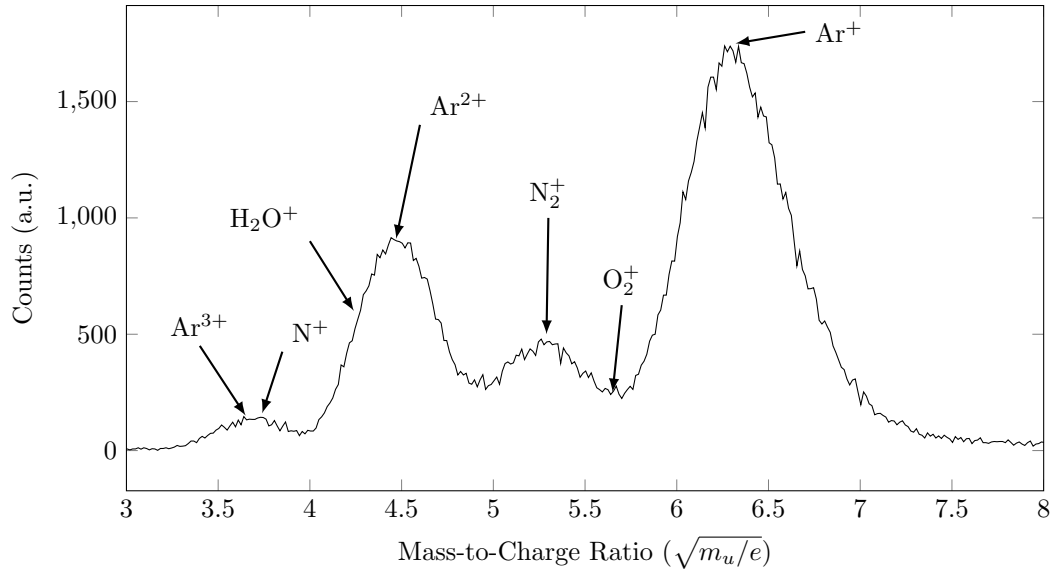
Figure 5.2: Electron impact at $200\,\text{eV}$ mass calibrated to Ar^+, Ar^{2+} and N_2^+. The locations of Ar and atmospheric peaks are marked with arrows. Significant amounts of N_2 and H_2O can be observed in the target beam.

Species	Fit Parameters ($\sqrt{m_u/e}$)	
	x_c	FWHM
Ar^+	6.32(1)	1.32(1)
N_2^+	5.27(1)	0.78(3)
Ar^{2+}/H_2O^+	4.49(1)	0.98(1)
Ar^{3+}/N^+	3.70(1)	0.96(3)

Table 5.3: Gaussian fit parameters for the four prominent peaks of Figure 5.2. Peak centers (x_c) and FWHM are shown in units $\sqrt{m_u/q}$. The fit corresponding to Ar^+/H_2O^+ is of the total peak which is generated by both ion species which cannot be separated in these measurements.

5.2.2   Gated Counting Measurements

While poor TOF separation prevents the discrimination of H_2O^+ and Ar^{2+} in ion spectra, the two ions have markedly different ionization thresholds ($12.6\,\text{eV}$ and $43.4\,\text{eV}$ respectively) and can be differentiated when comparing the cross sections as a function of energy (Appendix A) with gated ion counting. Initially, excitation functions of singly and doubly ionized Ar were acquired using narrow windows positioned to reduce signals not originating from Ar collisions (Figure 5.3). While useful in determining ionization thresholds, narrow windows result in low count rates and these measurements cannot be assumed to be representative of the actual cross section values.

The results of this threshold study are shown in Figure 5.4 where the literature ionization potentials[19] of Ar^+ and Ar^{2+} are marked with arrows. While some background is still observed in the functions, the onset of significant ionization can be seen to occur at the marked energies. This provides confirmation that the ions have been correctly identified in the spectum Figure 5.2, validating the calibration.

Excitation functions were also obtained with wider gates to improve count rates and acquire
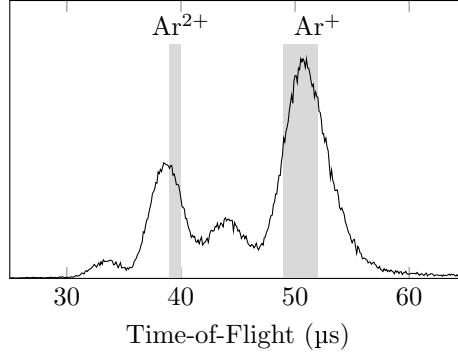
Figure 5.3: Narrow counting windows used in the threshold study. This removes a significant portion of the signal generated by background ionization peaks.
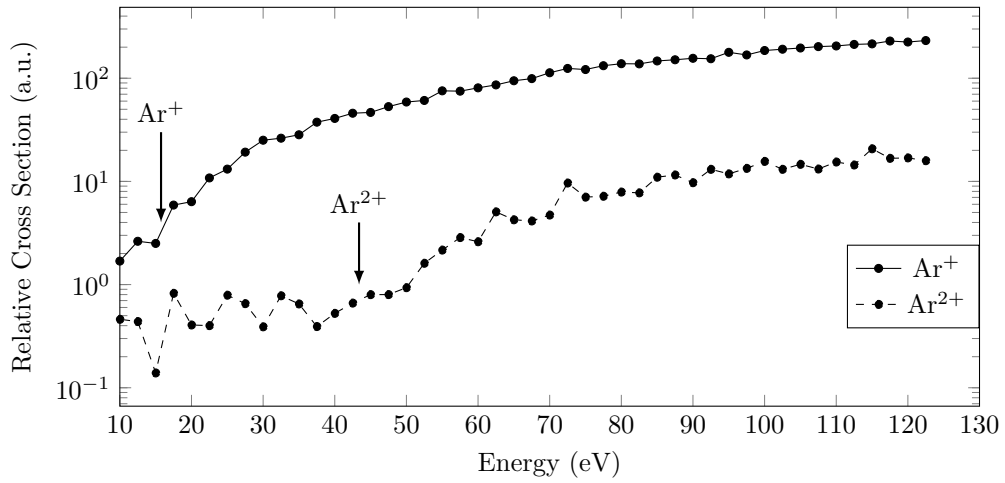
Figure 5.4: Semi-logarithmic plot of the excitation functions of Ar^+(solid) and Ar^{2+}(dashed) from threshold to 125 eV taken with narrow counting windows designed to reduce the influence of other ion species. The known thresholds[19] of both ions are marked with arrows. The onset of significant ion production is observed at these points indicating the ions have been correctly identified.

more representative data from threshold to 120 eV. As previously noted, the beam profile had to be estimated from the Faraday cup measurements due to the low emission current. A profile of the electron current as a function of energy was obtained (Figure 5.5) at 5 eV intervals over the energy range. The relative cross section at energy E was determined from the total ion counts C and the beam current J interpolated from the measured profile as

$$\sigma_{rel} = \kappa \frac{C(E)}{J(E)} \tag{5.1}$$

where κ is an arbitrary scaling factor. A relative uncertainty of $\pm 10\%$ has been assigned to the measurements of σ_{rel}. This is intended to account for the uncertainty in the electron beam profile, the presence of background ionization and statistical count variances.

The current normalized excitation functions of Ar^+ and Ar^{2+} are shown in Figure 5.6 and compared with the literature data. Reference cross sections were scaled to the measured values at 100 eV which is near the maximum value of both single and double ionization cross sections. There
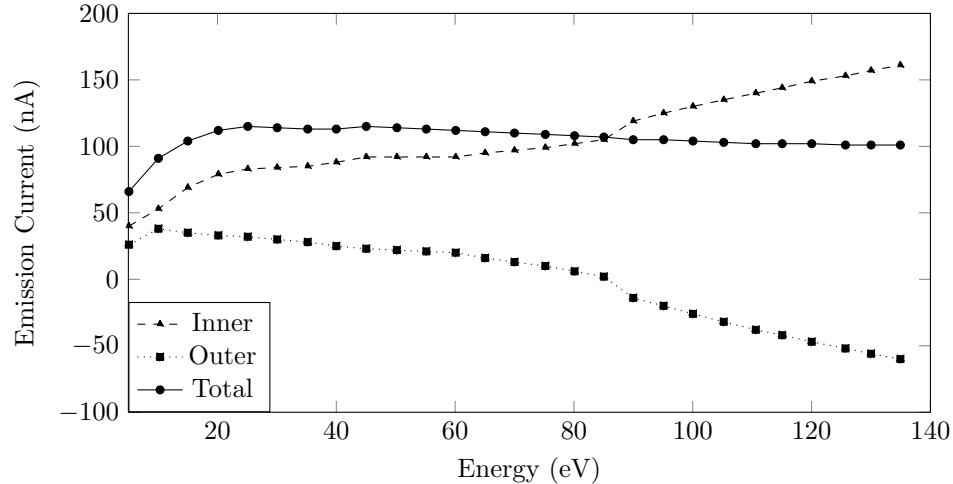
Figure 5.5: Electron beam current profile for energies of 5 eV to 140 eV, encompassing the study's region of interest.

does appear to be some disagreement with the accepted values, especially at lower energies. Near the threshold where the cross section is small, the presence of background ions with higher cross sections can become more pronounced presenting as an overestimation near the threshold. This may be the case with Ar^{2+} where agreement within error can be seen above 50 eV. However, there also appears to be a systematic deviation which seems to be present in both signals but is less noticeable in Ar^{2+} where lower count rates where observed.

If this deviation is due to energy dependent, systematic changes in the measurement which apply equally to all collisions, then the σ^{2+}/σ^+ ratio can still be derived from this data. A comparison of the measured ratio to the accepted values is shown in Figure 5.7 where the reference value has been scaled by a factor of 2.2 for comparison. The scaling is necessary to account for the fact that the counting gates did not encompass an equal fraction of each ion peak. The Ar^+ TOF peak is significantly broader than that of Ar^{2+} and less of its width could be covered without significant background contributions affecting the measured ratio. This difference in observed ion signal fractions is then corrected by the introduction of the scaling factor.

The ratio can be seen in Figure 5.7 along with the scaled, accepted ratio. Based on the reported errors of the Straub[37] cross sections, the reference value has a relative error of $\pm 5.7\%$. For energies of 60 eV and above, measurements agree within error except for one data point at 115 eV. Some of the disagreement at lower energies can likely be attributed to the small cross section of Ar^{2+} near threshold where the background results in an overestimation of the ionization ratio.

5.3 Discussion

5.3.1 Detector Resolution

It was determined that placing 9 V on the front TOF lens provided sufficient initial acceleration for good mass separation and reduction of asymmetric tails in ion distributions. Collisions occur over the entire interval of the electron pulse and over the whole volume of the interaction region

(a) Ar^+

(b) Ar^{2+}
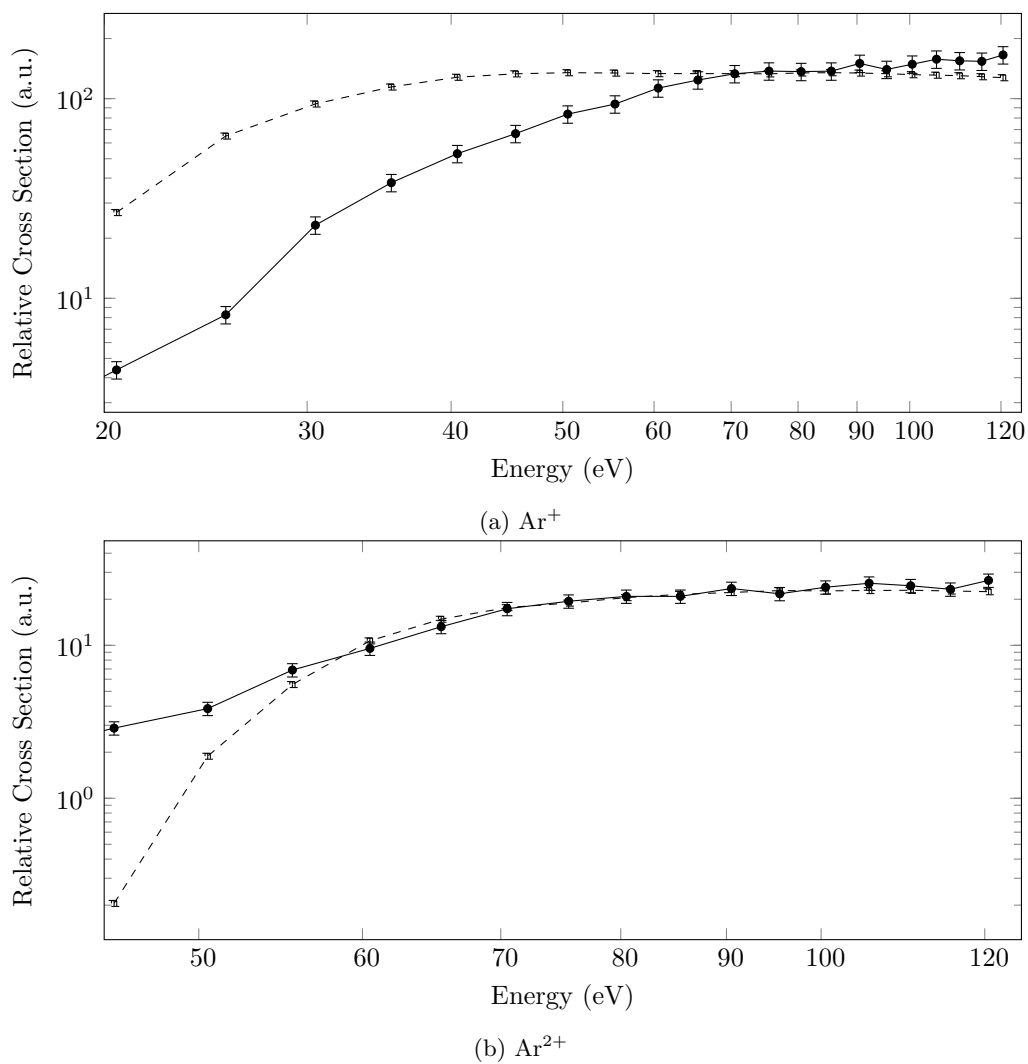
Figure 5.6: Comparison of measured ionization cross sections for Ar^+ and Ar^{2+} (solid lines) compared to scaled literature[37] data (dotted lines). Reference data was scaled to the measured values at $100\,eV$. While disagreement can be observed, this can largely be attributed to changes in electron focusing and beam bending by the TOF field at low energies.
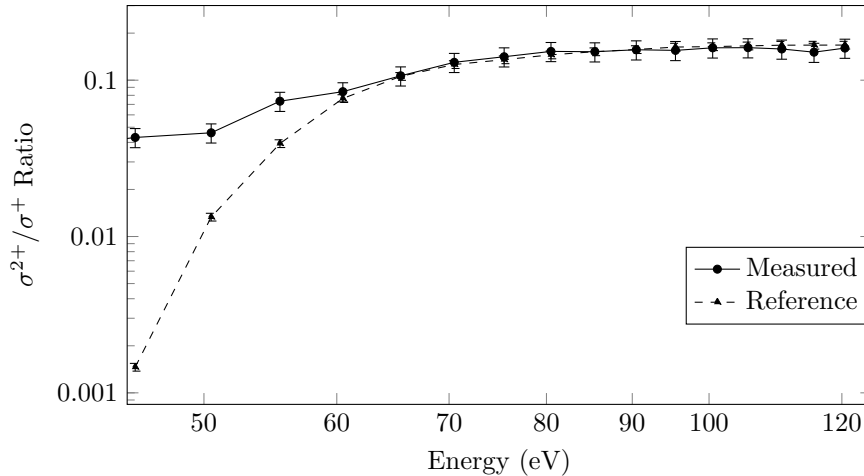
Figure 5.7: Measured double to single ionization ratio (solid line) with comparison to literature[37] (dashed line) for energies of 45 eV to 120 eV. The measured ratio has a relative uncertainty of $\sim 14\%$ and literature values $\sim 7.5\%$. Good agreement can be seen above 60 eV. Disagreement close to the ionization threshold can be attributed to background ion signals.

determined by the atomic and electron beam geometries. With larger extraction fields, the increased force on the ions dominates the differences due to their initial distribution reducing the observed ion peak width.

While these fields are ideal for obtaining good resolution in TOF spectra, difficulties can arise in studies with low energy electrons in the presence of large extraction fields. For energies of a few eV, a 9 V potential can produce forces large enough to bend the beam, diverting it from the target. This presents a problem when attempting to study collisions near the ionization threshold for weakly bound atomic systems such as Cs which has an ionization potential of less than 4 eV. One solution is to use a pulsed, rather than DC, extraction field which is turned on shortly after the end of the electron pulse. This would require modification of the detector circuitry but allows for improved resolution over a DC field in threshold studies.

The mass resolution of the detector is heavily dependent on the extraction fields used and the focusing of the ions onto the detector. Even with optimal settings, there are still limits on the achievable resolving power. Consider the spectrum of Figure 5.2 and the results presented in Table 5.3. The FWHMs indicate that ions can be well resolved for separations larger than one $\sqrt{m_u/e}$. For studies of Cs where the single and double ions are separated by ~ 3.4 units, this presents an acceptable resolution if peaks have similar TOF distributions. Trapped targets are considered to be stationary point sources and so their initial distributions will be far narrower than in collisions with thermal atoms and resolution should improve. Unfortunately, the resolution is still insufficient to determine the ionization ratios directly from the spectrum. When two peaks are heavily overlapped, with centers separated by less than the FWHMs of the peaks, it becomes difficult to separate them with Gaussian peak fitting routines and any fits which are found often have extremely large errors, making them statistically insignificant.

5.3.2   Cross Section Measurements

While the direct cross section measurements appear to suffer from systematic errors, the measured σ^{2+}/σ^+ ratio demonstrates agreement with accepted results at energies well above the Ar^{2+} threshold. This suggests that gated ion counting is quite viable provided that energy dependent changes in measurement condition are well understood, achieving the ultimate goal of the study. These systematic errors can be attributed to certain experimental factors which can be mitigated or eliminated completely in future measurements.

Obtaining an understanding of changes in electron beam focusing was difficult without more detailed beam profile measurements. As the wire probes could not be used, it is likely that changes in the beam profile resulted in and energy dependence which remained unaccounted for in analysis. This would not affect the ionization ratio as this is determined by the relative counts at a single energy. Likely, if the optimal focusing was found using more precise profile measurements, this dependence could be mitigated and better accounted for in future analysis. Increased beam currents would also improve the measurements resulting from higher count rates.

The presence of background ions was a significant problem in these measurements. Ionization signals from atmospheric constituents in the atomic beam resulted in obfuscation of the Ar peaks which prevented proper resolution of the multiple ionization peaks directly from the TOF spectra. While gated counting allowed for resolution of the Ar^{2+} peak and determination of σ^{2+}/σ^+, background still posed a difficulty in these measurements. In experiments under UHV where an externally injected atomic beam is no longer used, these signals will be significantly reduced or possibly completely eliminated. The atomic beam also had an associated thermal velocity distribution which contributed to broadening of the TOF peaks. One of the advantages of using a trapped target is that it can be considered a point source with negligible initial velocity. Detector resolution will improve in this case as ion peaks will be narrower than those obtained with thermal velocity targets.

While the issues encountered in the measurement prevent more accurate determination of Ar ionization cross sections, they still demonstrate that gated counting and excitation function measurements may have some utility in other experiments. The biggest problem with this method appeared to be energy dependent variations in electron current which can be mitigated by scanning over smaller energy ranges and with a better understanding of the beam profile. These types of measurements may prove useful in situations where resonances[17] appear in the collision cross section which are only observed over narrow energy ranges. However, this experiment shows that accurate data cannot be obtained over large energy ranges without better understanding of the beam profile. Furthermore, the method is sensitive to the presence of background ion counts, albeit less than in direct analysis of TOF spectra. In situations where there is poor peak separation, this method may give misleading results and care must be taken when attempting to derive cross section values from this data without good knowledge of the experimental parameters.

If gated counting was performed with wider windows, a larger fraction of the ion peak could be included and it may be possible to increase the accuracy of the measurements, but this would also introduce further background. In principle, background can be subtracted from measurements using known reference data but the large energy dependent effects prevented this from being performed with the present data. Curve fitting algorithms could be used to estimate the contribution due to background using reference data for Ar and atmospheric molecules in order to estimate the relative contributions. However, implementing arbitrary curve fitting with multiple datasets and functions

involves considerable time due to the lack of easily obtainable, "out of the box" solutions. As much is already known about electron impact of Ar, this improved accuracy would also present little value in this case.

5.4   Conclusion

Measurements of electron collisions with Ar have been investigated in order to assess the performance of the detector and evaluate the effectiveness of various ion counting methods for use with the TOF detector. The presence of atmospheric constituents in the atomic beam and low electron beam currents prevented more accurate measurements of ionization cross sections. Given that these issues can be addressed in future measurements, these results serve as a proof of concept, demonstrating the detector resolution and viability of direct TOF spectra analysis and gated ion counting for use with this apparatus.

Chapter 6

Electron Impact Ionization of Cesium

The study of electron collisions with alkali atoms are of considerable importance[17, 26] to the understanding of atomic structure and scattering phenomena. They are amenable to calculation[5, 17] as the single valence electron can be modeled without including the multi-particle correlations associated with multiple valence electrons[4]. The large nuclear mass of Cs also results in relativistic motion of the inner electrons[4]. While the electron impact ionization of H and He is considered to be fully understood[5], more work is needed to develop models which completely describe scattering from more complex atomic systems with large numbers of electrons. As such, electron collisions with Cs represent an important benchmark for relativistic electron-atom scattering theories[3, 4]. Until recently[12, 13, 15], relatively little data has been available on the electron total scattering and total ionization cross sections of Cs. Many of the previous measurements were performed in crossed beam studies[40, 41] and date back several decades. Only a single measurement of the multiple ionization cross sections has been reported by Tate and Smith[16], dating back to 1934.

In the present study, multiple ionization ratios of atomic Cs were measured with ion TOF spectroscopy in a crossed beam setup. Experimental conditions were less favourable than those of previous studies of Ar collisions. Particularly, resolution suffered due to both lower atomic beam densities and increased ion spread associated with the heavier atomic mass of Cs which made resolution of multiple ionization peaks difficult in some TOF spectra. Measurements of the double and triple ionization ratios were most readily obtained for collisions at energies of 50 eV to 120 eV. Results are presented and compared to the measurements of Tate and Smith[16] and agreement is found between the two datasets across the measured energy range.

6.1   Motivation

Recently, a series of measurements of electron scattering from trapped Cesium targets has been performed[12, 13, 15] to provide updated, accurate cross section values for benchmarking. The total scattering[12, 15] and total ionization cross sections were measured for collisions with ground state Cs and, for the first time[13], measurements of the $P_{3/2}$ excited state cross section were also reported. In these studies the absolute cross section was determined through the trap loss method (Section

Ion Species	Ionization Energy (eV)
Cs^+	$3.893905548(19)^*$
Cs^{2+}	$27.051356(6)^*$
Cs^{3+}	$60.246(4)^\triangle$

Table 6.1: Ionization potentials of the first three ions of neutral ^{133}Cs. Data is taken from NIST database[19]. Experimentally measured values are noted $*$ and results extrapolated from experimental data with $\triangle$.

3.4). Collision trap losses were found by measuring changes in the trap fluorescence caused by the electron scattering event. Excellent agreement was found with previous measurements of the total scattering cross section[15]. Theoretical calculations also exhibit good agreement at energies above 75 eV but some differences with experiment do still exist at lower energies. Measurements of the total ionization cross section also exhibit excellent agreement[13] with previous measurements[16, 40, 41]. This level of agreement is consistent with that found in measurements of collisions with trapped Rubidium[10, 42].

Previous studies[12, 13, 15] detected collision losses through fluorescence measurements of the trapped Cs operating on the principle that ions produced in collisions will be off resonance with the lasers, exiting the trap. Since all ions escape, it is impossible to differentiate ion species strictly from trap fluorescence data. With ion TOF spectrometry however, the electrostatic forces are inherently charge selective of atomic ions permitting measurement of scattering cross sections of single and multiple ions.

6.2 Experimental Method

Electron impact of atomic Cs was performed in a crossed beam setup similar to that used for measurements of Ar (Chapter 5), the biggest difference being the employed atomic beam source. In this study, the Cs arm attached to the chamber (Figure 4.1) was heated to produce the atomic beam. A 4 µs electron beam pulse was introduced at a repetition rate of 2 kHz and collision products were collected by the TOF detector and read out via an MCS operating with 1 µs dwell time triggered to begin acquisition 5 µs after the end of the electron pulse. Low emission currents again prohibited the use of the wire beam probes for profile measurements so focusing characteristics were again estimated from the transmission current measured at the Faraday cups. Single and multiple ionization ratios of Cs were measured from threshold (Table 6.1) to 250 eV based on the relative areas of the corresponding ion peaks. Gated counting methods were not used in these measurements so as not to introduce systematic errors associated with possible changes in the interaction geometry over the course of the measurements. The TOF detector was focused with the same extraction fields as studies with Ar in order to keep the previous mass calibration, minimizing uncertainty in determining ion peak positions.

The objective was to measure the multiple ionization *ratios* rather than the absolute cross sections themselves, which can be found by scaling to previous measurements of the total ionization cross section[13]. This greatly simplifies the analysis process and allows for less stringent demands on the experimental protocol as it is not necessary to have detailed knowledge of the beam profiles and

densities. It is assumed that variations in the beam densities affect the bulk properties of the collision volume and so any changes in the ionization ratio, which can be attributed to atomic interactions, should be mostly independent of these parameters. The ionization ratio is simply

$$R_{\sigma^{n+}/\sigma^+} = \frac{N\left(A^{n+}\right)}{N\left(A^+\right)} \tag{6.1}$$

where the number of ions $N\left(A^{n+}\right)$ is found from the area of the corresponding peak in the TOF spectrum.

Rather than determine the cross sections through direct integration of the ion peaks, multi-peak Gaussian curve fitting routines (Origin® 6.0) were applied to all spectra in order to mitigate issues associate with peak overlap. The reported ionization ratios were determined from the statistically derived peak areas. If the peak positions and widths do not vary considerably between spectra, then this should provide a good representation of the actual peak area. Values are reported with their statistical error and an additional relative error of 15% to account for experimental variations in the measured ionization spectra. Lower count rates encountered in this study as well as increased broadening tended to contribute to larger variation between spectra than previously observed with Ar. While all attempts were made to optimize the experimental parameters for a particular spectrum, it was often difficult to obtain clear resolution of the multiple ions peaks, especially at higher energies. While Cs ion signals are sufficiently resolved in the spectra used to obtain the reported ionization ratios, wider TOF peaks and low signal to noise ratio due to the observed count rates lead to considerable variance in spectra, justifying the experimental uncertainty. This level of uncertainty which is still reasonable for a crossed beam study[17, 26].

6.3 Results

A comparison of ion spectra obtained with Ar and Cs targets is shown in Figure 6.1 where the previous mass calibration has been applied to both spectra. When fit independently, the calibration scales of both spectra also agree within 1% of each other, further validating the current calibration. However, due to low electron currents, collisions with Cs exhibited much lower count rates and wider TOF distributions compared to previous investigations with Ar. The injected Ar target had significantly higher pressure than the Cs beam used in this measurements and possibly a narrower beam profile, producing a more concentrated, higher density interaction region with narrower spatial and velocity distributions which would also imply smaller FWHMs of observed ion peaks. The far heavier mass of will Cs also contribute to widening of TOF peaks. As a result, considerable increases in data acquisition time were needed to obtain results of statistical significance. The Cs spectrum of Figure 6.1 also exhibits atmospheric background ions at the lighter end of the spectrum, even at UHV pressures. While not well resolved due to low statistics, the background appears to be comprised of usual atmospheric constituents such as H_2O, N_2 and O_2. Due to the differences in mass-to-charge ratios, peaks up to Cs^{3+} ($\sqrt{m/q} \approx 6.7$) are still well separated from this mass region.

In an attempt to increase the target density, the pressure of the collision chamber was increased by restricting the manual valve separating the main chamber from the vacuum pumps. As the ion gauge which measures vacuum pressure is located on the same side of the valve as the pumps, Cs pressure could not be determined directly. It is estimated that pressures of 10^{-6}-10^{-5} torr were achieved
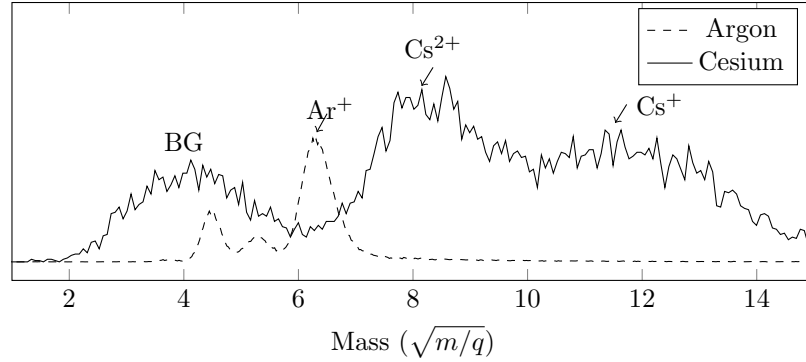
Figure 6.1: Comparison of ion TOF spectra obtained in collisions with Ar and Cs targets with 200 eV impact energy. The Cs single and double ionization peaks are marked along with Ar^+. Atmospheric background (BG) present in Cs spectra (mostly N_2 and H_2O) are also noted.
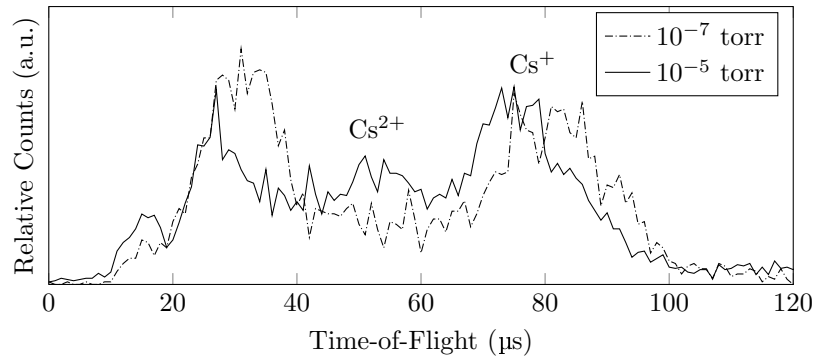
Figure 6.2: Ion TOF spectra acquired at 10^{-5} torr (solid) and 10^{-7} torr (dashed) for collisions at 100 eV. While the low count rate in these scans does contribute to channel-to-channel noise, significant systematic changes in the ion distribution are observed occur at higher pressures including differences in the relative peak heights of the $Cs^{+,2+}$ ion signals.

with this method. While increased pressure did raise measured count rates, significant changes were observed in the TOF spectra at these higher pressures (Figure 6.2). Repeatedly, significant changes in the TOF spectra were observed at all energies including ion peak broadening and systematic changes in the *relative* peak heights of Cs ion signals. Likely, detector efficiency decreases if the ion distribution broadens beyond a critical width, but only for a specific ion, changing the measured ratio. Collision measurements were performed at pressures of approximately 10^{-7} torr to reduce peak broadening in spectra ensuring equal detection efficiencies for all ions.

Even with the increased time separation of the peaks seen in Cs spectra, overlap was still observed due to significant increases in ion peak widths. Due to low total counts and the lower signal-to-noise ratio (SNR), statistical fitting errors in determined peak areas could sometimes exceed 20%. With a relative difference of only $\sqrt{m/q} \approx 1.5$, it was also difficult in some cases to fully resolve the Cs^{2+} and Cs^{3+} peaks. Far greater sensitivity to electron beam focusing conditions was also observed compared to studies of Ar. Poor beam focusing would often result in broadening of the measured ion peaks and per-ion changes in collection efficiency, particularly in the case of Cs^+, systematically increasing the measured ionization ratios.

Peak broadening was especially problematic at higher energies (above 120 eV). In most cases,
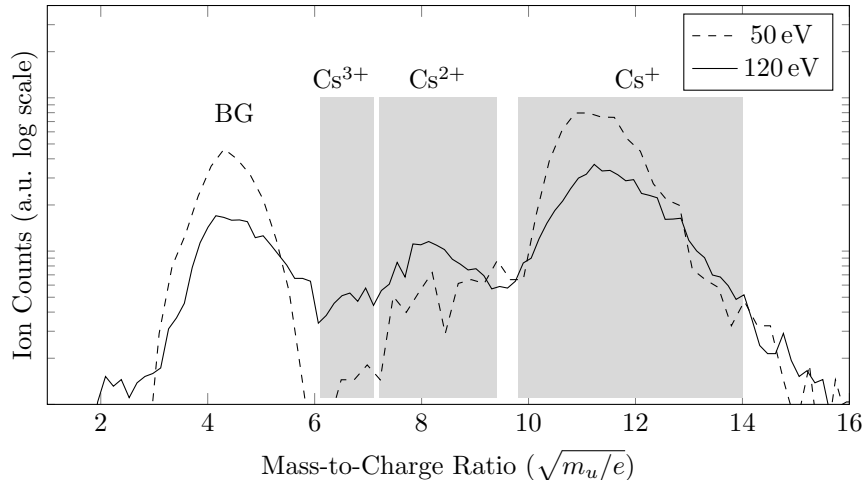
Figure 6.3: Measured ion spectrum for collisions at $120\,\mathrm{eV}$ and $50\,\mathrm{eV}$, the spectrum has been mass calibrated. Peaks corresponding to Cs^{n+} for $n \leq 3$ are marked. Ionization signals from collisions with atmospheric background (BG) is also shown. Spectra compare the TOF signal above and below the Cs^{3+} ionization potential (Table 6.1).

the Cs^+ peak was of sufficient width that it began to obscure the Cs^{2+} ion signal (Figure 6.4) preventing separation with curve fitting routines. At lower energies, peak widths and positions were quite constant across multiple spectra but systematic increases in peak widths could be seen at higher collision energies. It was not possible to determine the double ionization cross section above $120\,\mathrm{eV}$ as the Cs^+ peak began to appreciably overlap even the Cs^{3+} peak. The Cs^{3+} peak could often be resolved at these energies, but as it was not possible to separate contributions from Cs^+ and Cs^{2+} the ratio still could not be determined in these cases.

The measured multiple ionization ratios are shown in Figure 6.5 compared to the values reported by Tate and Smith[16]. There does appear to be some variance in the present data which could partly be attributed to the low total counts and sensitivity to experimental parameters such as beam and detector focusing but the results do agree with Tate and Smith within error. The σ^{3+}/σ^{2+} is also compared in Figure 6.6 and comparable agreement can be seen between the two datasets.

6.4 Discussion

While agreement has been found between the present measurements and the ionization ratios reported by Tate and Smith[16], the level of uncertainty associated with the present study prevents improvement upon the previous values. The experimental and statistical errors encountered in the current study were largely due to the low SNR and the broad, poorly resolved peaks observed in TOF spectra. This shows a clear need to reduce experimental uncertainties if high precision measurements of the multiple ionization ratios of Cs are desired. With larger ion count rates and improved charged particle focusing, the present method could be dramatically improved, greatly increasing the precision of measured cross section data.

The low electron and atomic beam densities greatly reduced observed count rates which made obtaining quality TOF spectra difficult. Replacement of the cathode was deferred due to the considerable time involved but once performed should drastically improve spectra quality. Even emission
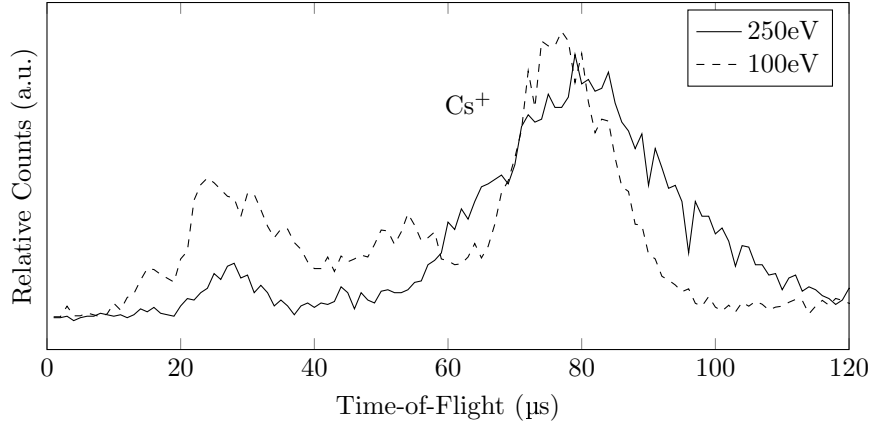
Figure 6.4: Ion TOF spectrum at $225\,\mathrm{eV}$ collision energy (solid) and $100\,\mathrm{eV}$ (dashed). At higher energies, the ionization peaks exhibit systematic broadening preventing resolution of Cs^{2+}. Peaks can be resolved at $100\,\mathrm{eV}$ where the Cs^+ peak has a FWHM of about $15\,\mathrm{\mu s}$ but for energies of $250\,\mathrm{eV}$ the FWHM is about $32\,\mathrm{\mu s}$, an increase of over 100%.

currents on the order of µA would increase observed ion counts by a few orders of magnitude leading to a significantly higher SNR. This alone would lead to increased precision in future studies.

Observed ion peaks were also quite broad and prevented discrimination of Cs^+ and Cs^{2+} at higher energies above $120\,\mathrm{eV}$. There were a number of factors which lead to this poor resolution. Noise and statistical variance due to a low SNR lead to poor spectra quality and made peak discrimination difficult. The width of TOF distributions and therefore ion spectra resolution are also dependent on the collision geometry, scattering product mass, and charged particle focusing. The interaction region, defined by the overlap of the electron and atomic beams, has a finite volume over which ions can be created in collisions. Ideally, most of the ions produced throughout this volume are collected by the detector and contribute to the TOF spectrum. A larger collision volume will lead to wider ions peaks, reducing resolution. The electron beam focusing also affects the size of the interaction volume. As the beam focusing was determined from measurements of the Faraday cup currents rather than beam cross sections, due to the low emission current, it is likely that with a new cathode an improved focusing could be found using the beam probes which could create a smaller interaction region. While the TOF detector was previously focused during measurements of Ar, the larger mass of Cs will likely lead to different focusing characteristics. The low count rates prevented further detector optimization with Cs and so it is also possible that TOF spectrum resolution could be improved in the future if a better lens potential configuration is found when higher count rates are possible.

6.5   Conclusion

Multiple ionization ratios of Cs have been reported for energies of $50\,\mathrm{eV}$ to $120\,\mathrm{eV}$. Poor resolution due to low SNR and broad ion TOF peaks prevented measurement of these values at higher energies. The current data agrees with the previously reported values of Tate and Smith[16] to within experimental error. The present study demonstrates that further work is needed to achieve better ion count rates and improved resolution if high precision measurements of the ionization cross sections
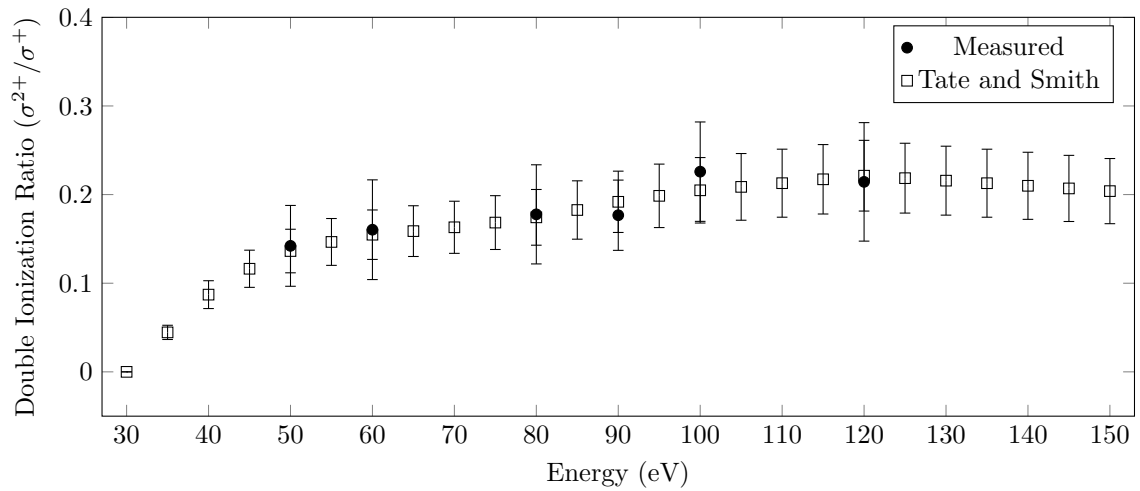
(a) Double ionization ratio
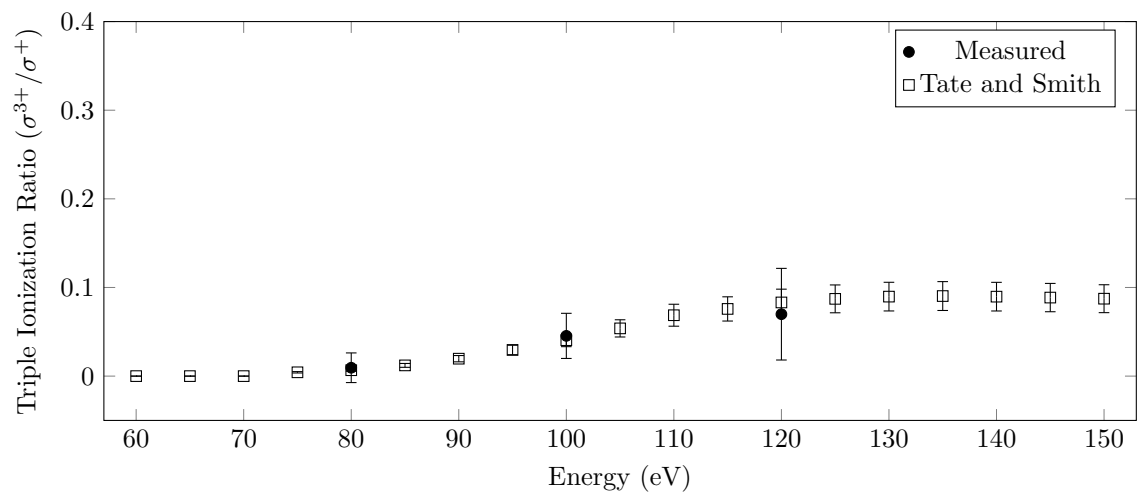
(b) Triple ionization ratio

Figure 6.5: Measured multiple ionization ratios (circles) of Cs from threshold to 250 eV. The values are compared with those of Tate and Smith[16] (squares).
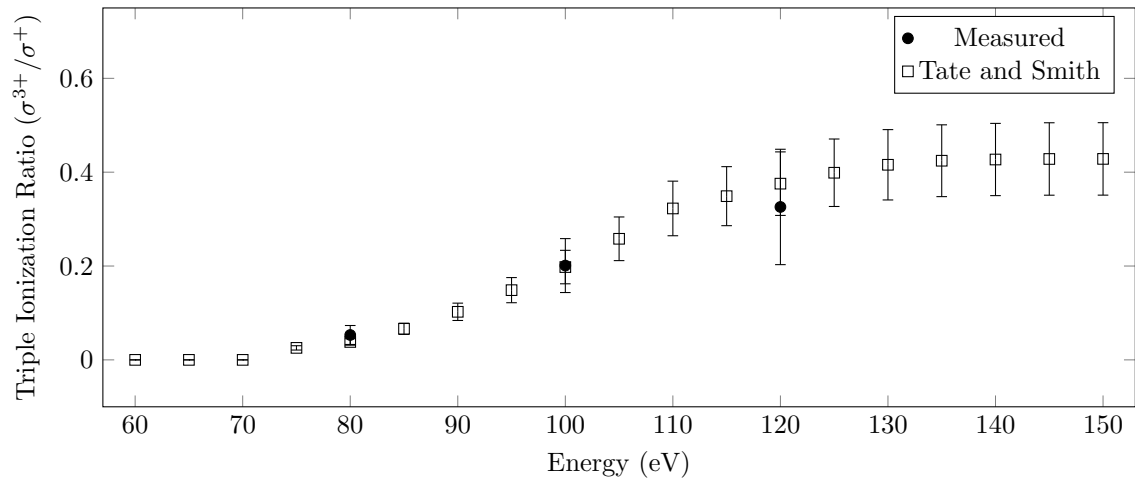
Figure 6.6: Observed σ^{3+}/σ^{2+} ratio compared to Tate and Smith[16].

are to be obtained. However, this should certainly be achievable with the proposed modifications of the current setup.

Chapter 7

Conclusion

Measurements of the multiple ionization ratios of Cs have been presented and compared with the values reported by Tate and Smith[16] and have been found to agree within experimental error. Low SNR and poor ion peak resolution lead to large uncertainties in the present work which cannot improve on the results of Tate and Smith due to difficulties with the present setup. This speaks not only to the difficulty of obtaining quality results in collision studies of heavy targets such as Cs but also the quality of Tate and Smith's measurements, which have been shown to be quite accurate even though dating back almost a century. However, the current study does demonstrate that with the appropriate modifications, it should be able to obtain high precision measurements of the multiple ionization ratios in future experiments. With increased electron beam currents, improved charged particle focusing, and the use of a trapped target, future investigations should be able to obtain well resolved TOF spectra with improved precision.

In the present study, low electron beam current lead to reduced ion count rates and poor SNR in TOF spectra. Emission currents of about $150\,\mathrm{nA}$ were observed in this work which is orders of magnitude below the manufacturer reported $3\,\mathrm{mA}$ maximum output of the cathode. This indicates that the present cathode is likely damaged and needs to the replaced. The time required to complete this task is considerable due to the need to open the vacuum chamber, exposing it to atmospheric pressure and the time required to restore UHV pressures after opening the chamber, which is on the order of weeks. This is the reason the cathode was not replaced during this work. After replacement, higher ion counts should be immediately observed which should dramatically increase the SNR, leading to better resolution of the ion peaks.

While the focusing of the electron beam and ion detector, based on studies of Ar, were assumed to be near optimal, detailed studies of the focusing could not be performed with Cs in the present work because of the low observed ion counts. Due to the low electron currents, the translating wire probes could not be used for determining cross sections of the beam as the observed currents were below the detection limits of the system. With higher count rates, it may be possible to better tune the extraction field focusing for Cs, improving resolution as well as the electron beam focusing.

During collision studies of Ar, it was observed that large extraction fields lead to electron beam bending at lower collision energies. While the field strengths used in this study were necessary for achieving a sufficient resolution, they were observed to introduce systematic decreases to the measured cross sections below $60\,\mathrm{eV}$. Rather than using a DC field, the detector potentials could

instead be pulsed to only turn on after the end of the electron pulse and remain grounded when off. This would allow for low energy studies without sacrificing TOF detector resolution.

The use of a cold, trapped target will also provide many extremely desirable advantages (Section 3.4) in future studies including access to an excited state target, the ability to remove atmospheric background from TOF spectra, and improved resolution in ion spectra. As the lasers excite a significant fraction of the trap population to the $P_{3/2}$ state, cross sections can be obtained for this excited state which was not possible in the present study. Due to the current lack of data on scattering from excited state Cs[13, 28], this ability is of considerable interest. Atmospheric background in the present study contributed to difficulty in measuring highly charged ions (Cs^{4+} and higher). In this future this could be removed in cold collision studies during analysis[10], improving the ability to resolve these higher charge Cs ion peaks. The cold target can also be considered a stationary point source not only simplifying analysis which determining collision cross sections, but also reducing the widths of observed TOF distributions in ion spectra. This should permit increased precision over present studies where an atomic beam with a finite distribution was used.

With the incorporation of these improvements in future collisions studies, higher precision cross section data should be readily obtained. The current results indicate that measurements will be similar in magnitude to those of Tate and Smith[16] although further study is still quite fruitful as increased precision over previously reported measurements should be achievable. When used with a trapped target, the current TOF detector should also be able to obtain multiple ionization cross section data for the $P_{3/2}$ state for which no experimental data currently exists[13] and demonstrates a clear motivation for future investigation.

Bibliography

[1] P. J. Mohr, B. N. Taylor, and D. B. Newell, "Codata recommended values of the fundamental physical constants: 2010*", Rev. Mod. Phys. **84**, 1527–1605 (2012).

[2] M. Niering, R. Holzwarth, J. Reichert, P. Pokasov, T. Udem, M. Weitz, T. W. Hänsch, P. Lemonde, G. Santarelli, M. Abgrall, P. Laurent, C. Salomon, and A. Clairon, "Measurement of the hydrogen 1s-2s transition frequency by phase coherent comparison with a microwave cesium fountain clock", Phys. Rev. Lett. **84**, 5496–5499 (2000).

[3] O. Zatsarinny, K. Bartschat, N. Y. Babaeva, and M. J. Kushner, "Electron collisions with cesium atoms—benchmark calculations and application to modeling an excimer-pumped alkali laser", Plasma Sources Science and Technology **23**, 035011 (2014).

[4] K. Bartschat and Y. Fang, "Relativistic r matrix with pseudostates calculations for electron scattering from cesium atoms", Physical Review A **62**, 052719 (2000).

[5] I. Bray, D. Fursa, A. Kadyrov, A. Stelbovics, A. Kheifets, and A. Mukhamedzhanov, "Electron-and photon-impact atomic ionisation", Physics Reports **520**, 135–174 (2012).

[6] C. J. Bostock, D. V. Fursa, and I. Bray, "Relativistic convergent close-coupling calculation of inelastic scattering of electrons from cesium", Phys. Rev. A **89**, 032712 (2014).

[7] C. Cohen-Tannoudji and D. Guery-Odelin, *Advances in atomic physics: an overview* (World Scientific Publishing, 2011).

[8] H. J. Metcalf and P. van der Straten, *Laser cooling and trapping* (1990).

[9] M. Saffman and T. Walker, "Analysis of a quantum logic device based on dipole-dipole interactions of optically trapped rydberg atoms", Physical Review A **72**, 022347 (2005).

[10] R. Schappe, M. Keeler, T. A. Zimmerman, M. Larsen, P. Feng, R. C. Nesnidal, J. B. Boffard, T. G. Walker, L. Anderson, and C. C. Lin, "Methods of measuring electron–atom collision cross sections with an atom trap", in, Vol. 48, edited by B. Bederson and H. Walther, Advances In Atomic, Molecular, and Optical Physics (Academic Press, 2002), pp. 357–390.

[11] L. J. Uhlmann, R. G. Dall, A. G. Truscott, M. D. Hoogerland, K. G. H. Baldwin, and S. J. Buckman, "Electron collisions with laser cooled and trapped metastable helium atoms: total scattering cross sections", Phys. Rev. Lett. **94**, 173201 (2005).

[12] J. MacAskill, W. Kedzierski, J. McConkey, J. Domyslawska, and I. Bray, "Measuring cesium electron impact cross-sections using a magneto-optical trap", Journal of electron spectroscopy and related phenomena **123**, 173–184 (2002).

[13]M. Łukomski, S. Sutton, W. Kedzierski, T. Reddish, K. Bartschat, P. Bartlett, I. Bray, A. Stelbovics, and J. McConkey, "Electron-impact ionization cross sections out of the ground and $^6P_2$ excited states of cesium", Physical Review A **74**, 032708 (2006).

[14]J. A. MacAskill, *Electron collision studies of cesium using a magneto-optical trap* (2003).

[15]M. Łukomski, J. MacAskill, D. Seccombe, C. McGrath, S. Sutton, J. Teeuwen, W. Kedzierski, T. Reddish, J. McConkey, and W. van Wijngaarden, "New measurements of absolute total cross sections for electron impact on caesium using a magneto-optical trap", Journal of Physics B: Atomic, Molecular and Optical Physics **38**, 3535 (2005).

[16]J. T. Tate and P. T. Smith, "Ionization potentials and probabilities for the formation of multiply charged ions in the alkali vapors and in krypton and xenon", Phys. Rev. **46**, 773–776 (1934).

[17]E. McDaniel, *Atomic collisions: electron and photon projectiles*, Atomic Collisions (Wiley, 1989).

[18]I. Estermann, S. Foner, and O. Stern, "The mean free paths of cesium atoms in helium, nitrogen, and cesium vapor", Physical Review **71**, 250 (1947).

[19]A. Kramida, Yu. Ralchenko, J. Reader, and and NIST ASD Team, NIST Atomic Spectra Database (ver. 5.2), [Online]. Available: `http://physics.nist.gov/asd` [2014, December 16]. National Institute of Standards and Technology, Gaithersburg, MD. 2014.

[20]D. A. Steck, "Cesium d line data", Los Alamos National Laboratory (unpublished) **124** (2003).

[21]J. J. Sakurai and J. Napolitano, *Modern quantum mechanics* (2011).

[22]E. Arimondo, M. Inguscio, and P. Violino, "Experimental determinations of the hyperfine structure in the alkali atoms", Rev. Mod. Phys. **49**, 31–75 (1977).

[23]P. Burke, *R-matrix theory of atomic collisions: application to atomic, molecular and optical processes*, Springer Series on Atomic, Optical, and Plasma Physics (Springer Berlin Heidelberg, 2011).

[24]L. G. Christophorou, *Electron—molecule interactions and their applications*, Vol. 2 (Academic Press, 2013).

[25]J. D. Hein, H. Al-Khazraji, C. J. Tiessen, D. Lukic, J. A. Trocchi, and J. W. McConkey, "Excited atomic fragments following electron dissociation of pyrimidine", Journal of Physics B: Atomic, Molecular and Optical Physics **46**, 045202 (2013).

[26]H. S. W. Massey, E. H. Burhop, and H. Gilbody, *Electronic and ionic impact phenomena. vol. 1. collision of electrons with atoms* (Oxford, 1969).

[27]X. Ren, S. Amami, O. Zatsarinny, T. Pflüger, M. Weyland, W. Y. Baek, H. Rabus, K. Bartschat, D. Madison, and A. Dorn, "Kinematically complete study of low-energy electron-impact ionization of neon: internormalized cross sections in three-dimensional kinematics", Phys. Rev. A **91**, 032707 (2015).

[28]L. G. Christophorou and J. K. Olthoff, "Electron interactions with excited atoms and molecules", Advances in Atomic, Molecular, and Optical Physics **44**, 155–293 (2001).

[29]M. Shah, H. Camp, M. Trachy, G. Veshapidze, M. Gearba, and B. DePaola, "Model-independent measurement of the excited fraction in a magneto-optical trap", Physical Review A **75**, 053418 (2007).

[30] G. Veshapidze, J.-Y. Bang, C. Fehrenbach, H. Nguyen, and B. DePaola, "Model-free measurement of the excited-state fraction in a Rb^{85} magneto-optical trap", Physical Review A **91**, 053423 (2015).

[31] R. W. Boyd, *Nonlinear optics, third edition*, 3rd (Academic Press, 2008).

[32] D. J. Griffiths, *Introduction to electrodynamics; 4th ed.* (Pearson, Boston, MA, 2013).

[33] C. Dedman, K. Baldwin, and M. Colla, "Fast switching of magnetic fields in a magneto-optic trap", Review of Scientific Instruments **72**, 4055–4058 (2001).

[34] M. Boulay and A. Hime, "Technique for direct detection of weakly interacting massive particles using scintillation time discrimination in liquid argon", Astroparticle Physics **25**, 179–182 (2006).

[35] J. F. Lancaster, "The physics of welding", Physics in technology **15**, 73 (1984).

[36] N. Saito, Y. Ogawa, Y. Saso, C. Liao, and R. Sakei, "Flame-extinguishing concentrations and peak concentrations of N_2, ar, CO_2 and their mixtures for hydrocarbon fuels", Fire Safety Journal **27**, 185–200 (1996).

[37] H. C. Straub, P. Renault, B. G. Lindsay, K. A. Smith, and R. F. Stebbings, "Absolute partial and total cross sections for electron-impact ionization of argon from threshold to 1000 ev", Phys. Rev. A **52**, 1115–1124 (1995).

[38] A. Kobayashi, G. Fujiki, A. Okaji, and T. Masuoka, "Ionization cross section ratios of rare-gas atoms (ne, ar, kr and xe) by electron impact from threshold to 1 kev", Journal of Physics B: Atomic, Molecular and Optical Physics **35**, 2087 (2002).

[39] *The atmospheric chemist's companion* (Springer My Copy UK, 2012).

[40] K. J. Nygaard, "Electron-impact ionization cross section in cesium", The Journal of Chemical Physics **49**, 1995–2002 (1968).

[41] H. Heil and B. Scott, "Cesium ionization cross section from threshold to 50 ev", Physical Review **145**, 279 (1966).

[42] R. S. Schappe, P. Feng, L. W. Anderson, C. C. Lin, and T. Walker, "Electron collision cross-sections measured with the use of a magneto-optical trap", EPL (Europhysics Letters) **29**, 439 (1995).

[43] J. Böhlke, J. De Laeter, P. De Bievre, H. Hidaka, H. Peiser, K. Rosman, and P. Taylor, "Isotopic compositions of the elements, 2001", Journal of Physical and Chemical Reference Data **34**, 57–67 (2005).

[44] H. Straub, P. Renault, B. Lindsay, K. Smith, and R. Stebbings, "Absolute partial cross sections for electron-impact ionization of H_2, N_2, and O_2 from threshold to 1000 ev", Physical Review A **54**, 2146 (1996).

[45] H. Straub, B. Lindsay, K. Smith, and R. Stebbings, "Absolute partial cross sections for electron-impact ionization of CO_2 from threshold to 1000 ev", The Journal of chemical physics **105**, 4015–4022 (1996).

[46] H. Straub, B. Lindsay, K. Smith, and R. Stebbings, "Absolute partial cross sections for electron-impact ionization of H_2O and D_2O from threshold to 1000 ev", Journal of Chemical Physics **108**, 109–116 (1998).

[47]T. Meyrath, "Electromagnet design basics for cold atom experiments", University of Texas, Austin (2004).

Appendices

Appendix A

Scientific Constants and Data

A.1 Scientific Constants

A.2 Reference Cross Section Data
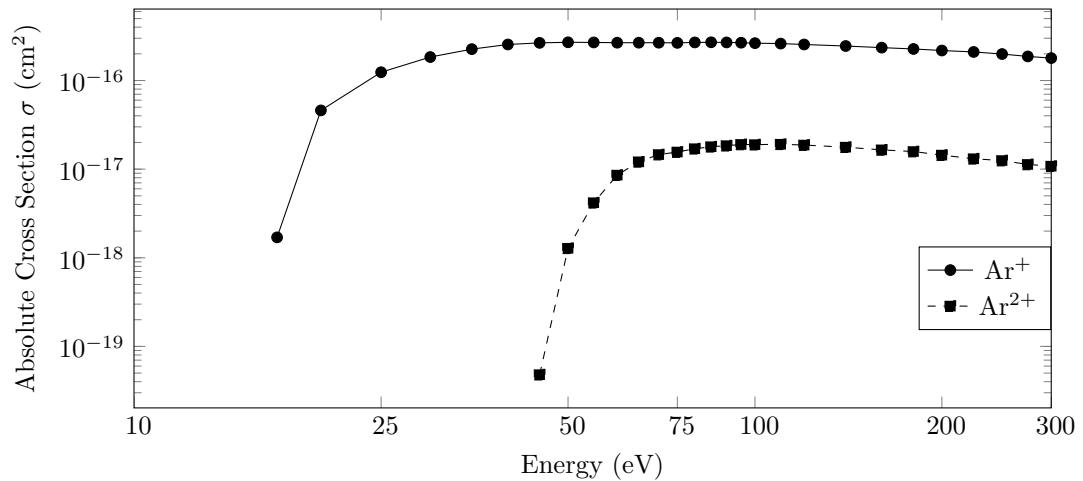
Figure A.1: Excitation function of Ar. Cross sections are shown for single and double ionization. Cross section data can be found in Table A.2 and [37].

Table A.1: Table of relevant scientific constants. Data taken from CODATA recommended values[1] with the exception of nuclear spin and isotopic abundance data. Nuclear spin values taken from [8] and isotopic abundances from [43].

Quantity	Symbol	Value	Units
Speed of light in a vacuum	c	$299\,792\,458$	m/s
Permeability of vacuum	μ_o	$4\pi \times 10^{-7}$	N/A^2
Permitivity of vacuum $(1/\mu_o c^2)$	ϵ_o	$8.854\,187\,817 \times 10^{-12}$	F/m
Electron volt	eV	$1.602\,176\,565(35) \times 10^{-28}$	J
Planck's constant	h	$6.626\,069\,57(29) \times 10^{-34}$ $4.135\,667\,516(91) \times 10^{-15}$	J s eV s
Reduced Planck's constant $(h/2\pi)$	$\hbar$	$1.054\,571\,726(47) \times 10^{-34}$ $6.582\,119\,28(15) \times 10^{-16}$	J s eV s
Boltzmann's constant	k_B	$1.380\,648\,8(13) \times 10^{-23}$ $8.617\,332\,4(78) \times 10^{-5}$	J/K eV/K
Elementary charge	e	$1.602\,176\,565(35) \times 10^{-19}$	C
Angstrom	Å	1×10^{-10}	m
Bohr magneton $(e\hbar/2m_e)$	μ_B	$9.274\,009\,68(20) \times 10^{-24}$ $5.788\,381\,806\,6(38) \times 10^{-5}$	J/T eV/T
Bohr radius	a_o	$0.529\,177\,210\,92(17) \times 10^{-10}$ $5.291\,772\,109\,2(17)$	m Å
Mass of the electron	m_e	$9.109\,382\,91(40) \times 10^{-31}$	kg
Universal gas constant	R	$8.314\,462\,1(75)$	J/(mol K)
Atomic mass constant $(\frac{1}{12}m(^{12}C))$	m_u	$1.660\,538\,921(73) \times 10^{-27}$	kg
Torrent	torr	$101\ 325/760$	Pa
Nuclear spin ^{133}Cs ^{40}Ar	I	7/2 0	
Natural isotopic abundance ^{133}Cs ^{40}Ar		100% 99.6%	

Table A.2: Reference data for single and multiple ionization cross sections of Ar up to Ar^{3+}. Measurements are taken from Straub[37].

Energy (eV)	σ^+ (10^{-16} cm^2)	σ^{2+} (10^{-17} cm^2)	σ^{3+} (10^{-19} cm^2)	σ^{tot} (10^{-16} cm^2)
17	0.017	–	–	0.017
20	0.46	–	–	0.46
25	1.24	–	–	1.24
30	1.84	–	–	1.84
35	2.26	–	–	2.26
40	2.55	–	–	2.55
45	2.66	0.005	–	2.66
50	2.7	0.128	–	2.73
55	2.69	0.418	–	2.77
60	2.67	0.856	–	2.84
65	2.67	1.21	–	2.91
70	2.67	1.46	–	2.96
75	2.66	1.56	–	2.97
80	2.69	1.7	–	3.03
85	2.7	1.79	–	3.06
90	2.69	1.84	–	3.06
95	2.67	1.9	0.51	3.05
100	2.64	1.89	1.03	3.02
110	2.61	1.91	2.21	3
120	2.55	1.87	3.23	2.93
140	2.45	1.77	4.94	2.81
160	2.35	1.65	5.57	2.7
180	2.27	1.58	5.68	2.6
200	2.18	1.44	5.53	2.49
225	2.1	1.31	5.3	2.37
250	1.99	1.25	5.23	2.25
275	1.87	1.13	5.09	2.11
300	1.79	1.08	5.03	2.02

Table A.3: Uncertainties associated with the Ar ionization cross sections of Straub[37] (Table A.2).

Cross Section	Relative Uncertainty (%)
σ^+	±3.5
σ^{2+}	±4.5
σ^{6+}	±6
σ^{tot}	±3.5

Table A.4: Ionization cross sections of atmospheric molecules. The results are obtained from measurements of electron impact of N_2[44], CO_2[45] and H_2O[46] obtained in a series of experiments performed by Straub *et al.* The measurements of water occurred at different intervals than those of the other molecules listed and these absent points are marked with dashes.

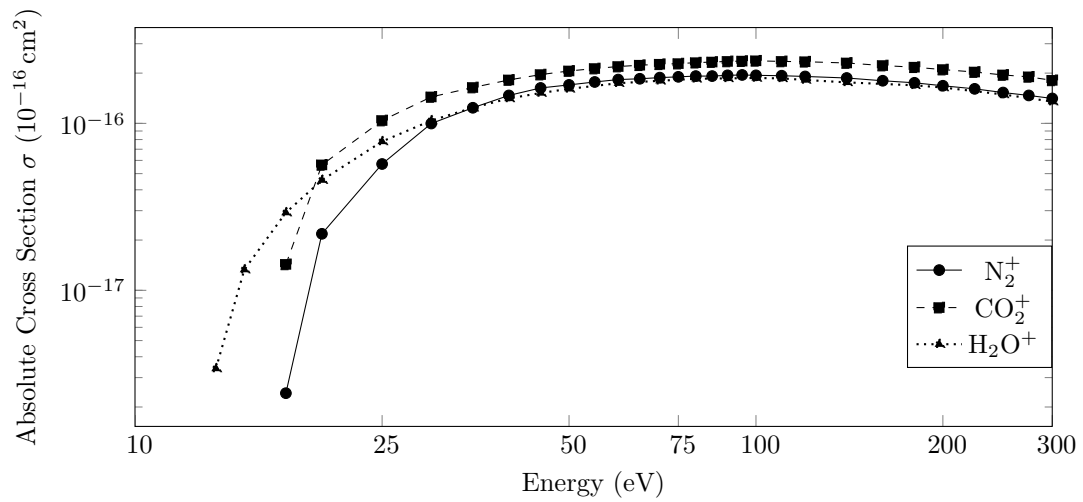| Energy (eV) | N$_2$ | | H$_2$O | CO$_2$ | |
	$\sigma(N_2^+)$ $(10^{-16}\,\mathrm{cm}^2)$	$\sigma(N^+{+}N_2^{2+})$ $(10^{-17}\,\mathrm{cm}^2)$	$\sigma(H_2O^+{+}OH^+{+}O^+)$ $(10^{-16}\,\mathrm{cm}^2)$	$\sigma(CO_2^+)$ $(10^{-16}\,\mathrm{cm}^2)$	$\sigma(CO^+)$ $(10^{-17}\,\mathrm{cm}^2)$
13.5	–	–	0.034	–	–
15	–	–	0.133	–	–
17.5	0.024	–	0.292	0.143	–
20	0.218	–	0.457	0.564	–
25	0.571	–	0.779	1.04	0.3
30	0.998	0.349	1.04	1.44	1.49
35	1.24	0.969	1.24	1.64	2.65
40	1.47	1.78	1.41	1.82	3.01
45	1.63	2.62	1.52	1.96	3.2
50	1.7	3.4	1.61	2.06	3.4
55	1.77	4.15	–	2.13	3.61
60	1.83	4.66	1.74	2.19	3.85
65	1.85	5.11	–	2.23	3.91
70	1.88	5.54	1.8	2.26	4.02
75	1.9	5.94	–	2.28	4.02
80	1.92	6.21	1.85	2.31	4.08
85	1.92	6.39	–	2.33	4.11
90	1.94	6.67	1.86	2.35	4.12
95	1.95	6.81	–	2.36	4.11
100	1.94	6.92	1.87	2.37	4.1
110	1.93	6.95	1.86	2.35	4.06
120	1.91	6.95	1.82	2.34	3.98
140	1.87	6.84	1.76	2.3	3.83
160	1.8	6.62	–	2.22	3.56
180	1.75	6.22	1.69	2.17	3.48
200	1.68	5.9	1.64	2.1	3.27
225	1.61	5.37	–	2.03	3.12
250	1.53	5.12	1.49	1.95	2.88
275	1.47	4.75	–	1.9	2.79
300	1.41	4.53	1.35	1.81	2.59

Figure A.2: Electron impact cross sections of primary ions produced in collisions with N_2, CO_2 and H_2O. Data can be found in Table A.4 and [44–46].
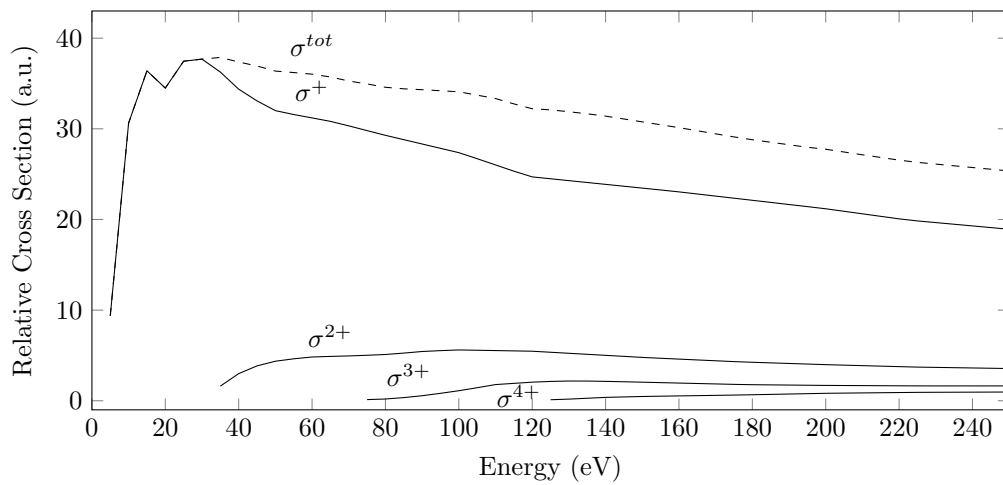

Figure A.3: Relative multiple ionization cross sections of Cs performed by Tate and Smith[16] (Table A.5) from threshold to $250\,\mathrm{eV}$.

Table A.5: Relative cross section measurements of Tate and Smith[16]. The data has been taken from a graph of the reported values present in the original publication.

Energy	σ^+	σ^{2+}	σ^{3+}	σ^{4+}
(eV)		(a.u.)		
5	9.37	–	–	–
10	30.64	–	–	–
15	36.4	–	–	–
20	34.5	–	–	–
25	37.46	–	–	–
30	37.69	–	–	–
35	36.26	1.62	–	–
40	34.38	2.99	–	–
45	33.08	3.85	–	–
50	32.01	4.36	–	–
55	31.58	4.63	–	–
60	31.2	4.83	–	–
65	30.83	4.89	–	–
70	30.33	4.95	–	–
75	29.8	5.02	0.13	–
80	29.28	5.1	0.19	–
85	28.8	5.26	0.35	–
90	28.33	5.43	0.56	–
95	27.85	5.53	0.82	–
100	27.37	5.61	1.11	–
105	26.71	5.57	1.44	–
110	26.02	5.54	1.79	–
115	25.33	5.5	1.92	–
120	24.7	5.47	2.05	–
125	24.49	5.35	2.13	0.11
130	24.29	5.24	2.18	0.18
135	24.08	5.12	2.18	0.28
140	23.87	5.01	2.14	0.37
145	23.67	4.9	2.1	0.42
150	23.46	4.78	2.05	0.47
155	23.25	4.69	2	0.51
160	23.04	4.6	1.95	0.54
165	22.81	4.5	1.91	0.57
170	22.58	4.41	1.86	0.6
175	22.35	4.32	1.81	0.63
180	22.12	4.25	1.77	0.66
185	21.88	4.18	1.75	0.7
190	21.65	4.12	1.73	0.74
195	21.42	4.05	1.71	0.78
200	21.18	3.99	1.69	0.82
205	20.9	3.93	1.68	0.85
210	20.62	3.88	1.67	0.87
215	20.35	3.82	1.66	0.89
220	20.07	3.77	1.65	0.91
225	19.84	3.71	1.64	0.93
230	19.66	3.68	1.64	0.94
235	19.47	3.65	1.64	0.94
240	19.29	3.62	1.64	0.95
245	19.11	3.59	1.64	0.96
250	18.92	3.56	1.64	0.96
255	18.73	3.52	1.64	0.97
260	18.54	3.49	1.65	0.98

Appendix B

Wigner-Eckart Theorem

The Wigner-Eckart is a powerful tool for determining the effect of vector operators on angular momentum eigenstates. For a rank k tensor $T_q^{(k)}$ operator acting on angular momentum states $|\alpha;\ j, m\rangle$, the matrix elements of the tensor operator are given by

$$\langle\alpha';\ j', m'|T_q^{(k)}|\alpha;\ j, m\rangle = \langle jk;\ mq|jk;\ j'm'\rangle\frac{\langle\alpha';\ j'\|T^{(k)}\|\alpha;\ j\rangle}{\sqrt{2j+1}} \tag{B.1}$$

There are two very important implications of this results. First, the matrix elements can be written in terms of a reduced matrix element $\langle\alpha';\ j'\|T^{(k)}\|\alpha;\ j\rangle$ which is *independent* of m and m'. Second, the dependence on m is completely described by the associated Clebsh-Gordan coefficient

$$C_{kqj'm'}^{jm} = \langle jk;\ mq|jk;\ j'm'\rangle \tag{B.2}$$

for adding momentum j and k to get j'.

Often when working with angular momentum states, it is useful to use the Wigner j symbols. The Wigner $3-j$ symbol can be connected to the Clebsch-Gordan coefficients through the relationship

$$\begin{pmatrix} j_1 & j_2 & j_3 \\ m_1 & m_2 & m_3 \end{pmatrix} \equiv \frac{(-1)^{j_1-j_2-m_3}}{\sqrt{2j_3+1}}C_{j_2,m_2,j_3,m_3}^{j_1,m_1} \tag{B.3}$$

The Wigner $3-j$ symbols obey a set of selection rules. The symbol will be zero unless

$$m_1 + m_2 + m_3 = 0 \tag{B.4a}$$

$$j_1 + j_2 + j_3 = n \tag{B.4b}$$

$$|m_i| \leq j_i \tag{B.4c}$$

$$|j_1 - j_2| \leq j_3 \leq j_1 + j_2 \tag{B.4d}$$

where n is an integer. Furthermore, if $m_1 = m_2 = m_3 = 0$, n must be an even integer.

The Wigner $6-j$ symbol can also be used when working with multiple momentum basis. The

symbols is defined as a summation over the $3j$-symbols

$$\begin{Bmatrix} j_1 & j_2 & j_3 \\ j_4 & j_5 & j_6 \end{Bmatrix} = \sum_{m_i} (-1)^S \begin{pmatrix} j_1 & j_2 & j_3 \\ m_1 & m_2 & -m_3 \end{pmatrix} \begin{pmatrix} j_1 & j_5 & j_6 \\ -m_1 & m_5 & m_6 \end{pmatrix}$$

$$\times \begin{pmatrix} j_4 & j_5 & j_3 \\ m_4 & -m_5 & m_3 \end{pmatrix} \begin{pmatrix} j_4 & j_2 & j_6 \\ -m_4 & -m_2 & -m_6 \end{pmatrix} \quad \text{(B.5)}$$

where the phase factor is summed over the 6 m values

$$S = \sum_{k=1}^{6} (j_k - m_k) \quad \text{(B.6)}$$

The value of the $6 - j$ symbol is zero unless $|j_2 - j_3| \leq j_1 \leq j_2 + j_3$.

Appendix C

Magnetic Field of Anti-Helmholtz Coils

A set of anti-Helmholtz coils consists of two coils of wire placed with their centers at locations $(0, 0, \pm D)$ above and below the xy-plane. Current is passed through both coils of wire but the flow of current is opposite. This configuration can be shown to result in a linear field gradient at the center fo the geometry. The derivations below follow those of Meyrath[47].

The magnetic field of a circular loop of wire with current I and radius R placed with its center at a position $(0, 0, D)$ above the xy-plane can be written in cylindrical co-ordinates

$$B_z = \frac{\mu I}{4\pi} \frac{1}{\sqrt{(R+\rho)^2 + (z-D)^2}} \left[K(k^2) + \frac{R^2 - \rho^2 - (z-D)^2}{(R-\rho)^2 + (z-D)^2} E(k^2) \right] \tag{C.1}$$

$$B_\rho = \frac{\mu I}{4\pi} \frac{z-D}{\sqrt{(R+\rho)^2 + (z-D)^2}} \left[-K(k^2) + \frac{R^2 + \rho^2 - (z-D)^2}{(R-\rho)^2 + (z-D)^2} E(k^2) \right] \tag{C.2}$$

defined in terms of the constant

$$k^2 \equiv \frac{4R\rho}{(R+\rho)^2 + (z-D)^2} \tag{C.3}$$

The equations are in terms of the complete elliptic integrals of the first and second kind $K(k)$ and $E(k)$ respectively which are defined as

$$K(k) = \int_0^{\pi/2} d\theta \, \frac{1}{\sqrt{1 - k^2 \sin^2 \theta}} \tag{C.4}$$

$$E(k) = \int_0^{\pi/2} d\theta \, \sqrt{1 - k^2 \sin^2 \theta} \tag{C.5}$$

Now consider the anti-Helmholtz geometry (Figure C.1). Two sets of coils are placed above and below the xy-plane with opposite currents. The coils are a distance $2D$ apart and the magnetic field near the origin $(0, 0, 0)$ can be determined from its Taylor series expansion. To third order, the
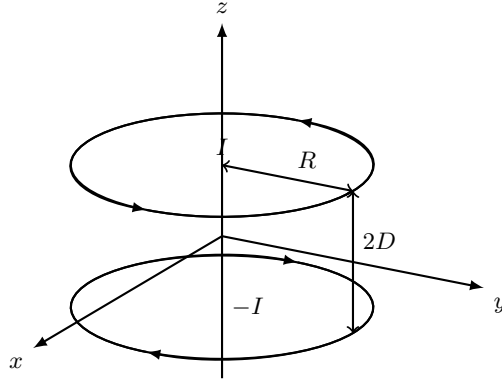
Figure C.1: Anti-Helmholtz coil geometry. Two coils are of radius R have opposite currents $\pm I$ flowing through them. The coils are placed symmetrically above and below the xy-plane a distance R apart. The problem can be solved in cylindrical co-ordinated (z, ρ, ϕ) and the solution is symmetric in the polar angle ϕ.

expansion is

$$B_z = \mu I 3 \, \frac{DR^2}{(D^2 + R^2)^{5/2}} z + \mu I \frac{15}{24} \frac{R^2(4D^2 - 3R^2)}{(D^2 + R^2)^{9/2}} (4z^3 - 6\rho^2 z) + \ldots \tag{C.6}$$

$$B_\rho = -\mu I \frac{3}{2} \frac{DR^2}{(D^2 + R^2)^{5/2}} \rho + \mu I \frac{15}{16} \frac{R^2(4D^2 - 3R^2)}{(D^2 + R^2)^{9/2}} (\rho^3 - 4\rho z^2) + \ldots \tag{C.7}$$

If the coils are placed a distance $2D = R$ apart then the magnetic field gradient is

$$\frac{dB}{dz} = \mu I \frac{48}{25\sqrt{5}R^2} = 2 \frac{dB}{d\rho} \tag{C.8}$$

The magnetic field gradient is linear both along the z axis and radially and the gradients in both directions differ only by a factor of two in the magnitude of the gradient.

Appendix D

Curve Fitting and Error Analysis

D.1 Gaussian Distributions

A Gaussian distribution

$$f(x; A, w, x_c) = \frac{A}{\sqrt{\pi w^2/2}} e^{-\frac{2(x - x_c^2)}{w^2}} \tag{D.1}$$

can be defined over the interval $x \in [-\infty, \infty]$ in terms of its area A, width w and the center of the distribution x_c. The distribution satisfies the normalization

$$\int_{-\infty}^{\infty} dx \; f(x; A, w, x_c) = A \tag{D.2}$$

corresponding to the total area A. The full width at half maximum (FWHM) is determined by

$$\text{FWMH} = 2\sqrt{2\ln(2)}w \tag{D.3}$$

according to the width parameter of the distribution.

D.2 Propagation of Errors

The inherent uncertainty of the measurement apparatus must be factored into the error of any results derived from them. For a function $f(x_i)$ dependent on an a set of variables x_i for $i \in S$ with uncertainties δx_i, the values calculated with the function have an uncertainty determined by

$$\delta f^2 = \sum_{i \in S} \left(\frac{\partial f}{\partial f_i}\right) \delta x_i^2 \tag{D.4}$$

and the propagated error is related to the uncertainties of the variables by the partial derivative of f with respect to each variable x_i.

A few regularly used error formula can be shown. For a sum of values

$$\delta(x_1 \pm x_2 \pm \ldots) = \sqrt{\delta x_1^2 + \delta x_2^2 + \ldots} \tag{D.5}$$

Multiplication and division propagate with relative error according to

$$\frac{\delta y}{|y|} = \sqrt{\frac{\delta x_1^2}{|x_1|^2} + \frac{\delta x_2^2}{|x_2|^2} + \dots} \tag{D.6}$$

The error in a power relation is derived from (D.4) as

$$\delta x^n = n|x|^{n-1} \, \delta x \tag{D.7}$$

More complex results can similarly be derived in terms of the partial derivatives.

VITA AUCTORIS

NAME:	Jeffery Michael Dech
PLACE OF BIRTH:	Windsor, ON
YEAR OF BIRTH:	1989
EDUCATION:	Riverside Secondary School, Windsor, ON, 2007
	University of Windsor, B.Sc. Hon., Windsor, ON, 2012
	University of Windsor, M.Sc., Windsor, ON, 2015